

学位論文（要約）

Spectral measurements of the diffuse near-infrared  
radiation with the CIBER rocket experiments

(CIBER ロケット実験による近赤外線拡散放射のスペクトル観測)

平成 25 年 12 月 博士（理学）申請

東京大学大学院理学系研究科  
物理学専攻

新井 俊明

## Abstract

Observations of the near-infrared diffuse radiation are crucial for the study of interplanetary and interstellar dust. The near-infrared diffuse radiation consists of Zodiacal Light (ZL), which is scattered sunlight by interplanetary dust, and Diffuse Galactic Light (DGL), which is scattered stellar radiation by interstellar dust. The scattering spectra and polarization by these dust particles can give valuable information of the size distribution, shape, refractive index, and input radiation. However, the ZL spectrum and polarization is not well known in the near-infrared. Moreover, because of its intrinsic faintness and contamination of other diffuse light, the DGL spectrum has never been observed in the near-infrared.

The near-infrared diffuse radiation includes not only ZL and DGL, but also Extra-galactic Background Light (EBL). One of the goals of observations of diffuse radiation in the near-infrared is to determine the spectrum of EBL. EBL is an integrated radiation produced by stellar nucleosynthesis and gravitational accretion on to massive black holes over the history of the universe. EBL is expected to contain also information on the epoch of reionization. Since UV radiation from the epoch of reionization emitted by the first ionizing stars and stellar remnants is redshifted into the near-infrared, the peak of spectral is expected in  $1\text{-}2\mu\text{m}$  due to the redshifted Lyman- $\alpha$  and Lyman-break features. Therefore, to reveal cosmic history of the epoch of reionization, near-infrared EBL measurements are expected to provide us with crucial information.

However, it is very difficult to make reliable measurement of the EBL spectrum in the near-infrared wavelength. Measurements of EBL are confronted with systematic uncertainties of subtraction of foreground of ZL and DGL. In order to measure accurate EBL brightness, it is therefore important to understand these foregrounds with sufficient accuracy.

We carried out the Cosmic Infrared Background Experiment (CIBER) with a sounding-rocket payload consisting of four instruments to study the near-infrared diffuse light from space. CIBER instruments are designed to measure spectrum, polarization, and spatial fluctuation of diffuse radiation in the near-infrared.

In this thesis, we describe the results of Low Resolution Spectrometer (LRS)

which is one of CIBER instruments. LRS measures spectrum and polarization of diffuse radiation in the near-infrared. LRS covers the wavelength range of 0.75-2.0 $\mu$ m with spectral resolution of  $R = 15 - 30$ . In addition, comprehensive data analysis for all the instruments would be powerful to the study of ZL, DGL, and EBL. In this thesis, we describe the result of LRS as a part of our work.

CIBER has flown four times, from White Sands Missile Range or Wallops Flight Facility. We observed five or six fields of  $5^\circ \times 5^\circ$  area of the sky in each flight with LRS. We selected observation fields based on the ecliptic latitude, which controls the brightness of zodiacal light, and column density of interstellar dust, which decides the brightness of diffuse galactic light, to separate ZL and DGL from the observed diffuse light reliably.

The observed diffuse radiation is analyzed with flux calibration data obtained in the laboratory and in-flight stability checks. The calibration error and the stability of the detector response are estimated to be  $\sim 3\%$ .

We estimate contamination by the airglow emission which is composed of stable atmospheric emission showing altitude dependence and time-decaying emission probably due to out-gassing from the payload at the altitude lower than 250km, and we successfully subtracted them from the observed data with enough accuracy (10% at low altitude, and better than 1% at high altitude). Next, we estimate the faint star contribution by Monte-Carlo simulation of the star distribution using 2MASS catalog and contemporary model of galaxy evolution with 10% accuracy. The resultant spectrum consists of ZL, DGL, and EBL. We call this resultant brightness as the sky brightness.

We decompose the sky brightness into three component; ZL, DGL, and EBL. We first extract the ZL spectrum by the difference between two fields which have the similar DGL brightness at different ecliptic latitude. In the same way, we also obtain the DGL spectrum by the difference between two fields which have the similar ZL brightness. We then iteratively find self consistent results of the ZL and the DGL spectrum with high S/N. Since we separate ZL and DGL based on global structure of dust distribution, we call this separation method as 'global-structure method'. Then we subtract the ZL brightness from the sky brightness and go back to the first step. The uncertainty of the resultant spectrum of ZL and DGL are better than 1% and 15%, respectively.

We can also separate the DGL spectrum using local structure of spatial distribution of the  $100\mu\text{m}$  brightness, hereafter 'local-structure method'. Thus we correlate the sky brightness with the  $100\mu\text{m}$  brightness in an local field. We obtain consistent result of the DGL spectrum from the local-structure method with that from the global-structure method.

The derived ZL spectrum shows the redder color than solar spectrum color. This spectrum color of zodiacal light is consistent with that of comets and that of asteroids in the near-infrared. These results indicate that the size of interstellar dust is predominated by large dust ( $\sim 2\mu\text{m}$ ). The wavelength dependence of polarization provides us to extra-information about physical property of interplanetary dust. We also derived the ZL polarization from the third flight data. The ZL polarization also shows the similar wavelength dependence of polarization of comets. In addition, the ZL polarization also supports the large interplanetary dust. Therefore, from both spectrum and polarization of ZL suggest that interplanetary dust is predominated by large dust ( $\sim 2\mu\text{m}$ ) and originates in debris of comets or/and asteroids.

We also derive the DGL spectrum in the near-infrared. Due to this intrinsic faintness of the DGL brightness, the DGL spectrum has never been measured in the near-infrared. Our result of the DGL spectrum in the near-infrared is the first measurements. The spectrum color of DGL shows bluer color than that of the stellar spectrum. Our result is well explained by a scattering model of interstellar dust. These results indicate that the interstellar dust is predominated by smaller particles ( $\sim 0.06\mu\text{m}$ ), and by typical composition; bare silicate, bare graphite and PAH particles.

One can see that the size distribution between interplanetary dust and interstellar dust is completely different from each other. The dust size difference is expected from a difference of morphosis between interplanetary dust and interstellar dust. The origin of interplanetary dust can be explained by debris of both comets and asteroids which are made from a collision and collapse of these bodies. The resultant particles should be large. On the other hand, interstellar dust originates in out-gassing of mass ejection from stars. The resultant particles cannot be grown up large particles in interstellar enviroment. Thus, the resultant particles should be small. Our result represents this morphosis difference between

interplanetary dust and interstellar dust.

From these foreground analysis, we constrain the detection limit on the EBL measurements. We estimated  $1\sigma$  uncertainty from the statistical uncertainties and the systematic uncertainties of the measurements. Since the measured brightness of EBL is  $\sim 50\text{nWm}^{-2}\text{sr}^{-1}$  at  $1.25\mu\text{m}$ , we could detect the measured EBL with  $5\sigma$ . On the other hand, the EBL is expected from known galaxy count as  $\sim 10\text{nWm}^{-2}\text{sr}^{-1}$ . When the EBL brightness is  $\sim 10\text{nWm}^{-2}\text{sr}^{-1}$ , we can measure it with  $1\sigma$ .



# Contents

<b>1</b>	<b>Introduction</b>	<b>1</b>
1.1	Near-Infrared Diffuse Sky Brightness . . . . .	1
1.2	Zodiacal Light . . . . .	3
1.3	Diffuse Galactic Light . . . . .	15
1.4	Extra Galactic Background Light . . . . .	16
<b>2</b>	<b>CIBER Rocket Experiment</b>	<b>21</b>
<b>3</b>	<b>Observation</b>	<b>23</b>
3.1	Field Selection . . . . .	23
3.2	Flight Performance . . . . .	26
3.2.1	Stability of Temperature . . . . .	26
3.2.2	Accuracy of Pointing . . . . .	26
3.2.3	Stability of Responsivity . . . . .	26
<b>4</b>	<b>Data Reduction and Analysis</b>	<b>33</b>
4.1	Obtaining the Image from the Raw Data . . . . .	33
4.2	Subtraction of Dark Current . . . . .	35
4.3	Removal of Bright Star . . . . .	37
4.3.1	Observed Sky Brightness . . . . .	37
4.3.2	Subtraction of Airglow . . . . .	40
4.3.3	Astronomical Sky Brightness . . . . .	43
4.4	Separation of Zodiacal Light and Diffuse Galactic Light by Differential of Two Field . . . . .	43

4.5	Separation of Zodiacal Light and Diffuse Galactic Light by Global-Structure Method . . . . .	47
4.6	Separation of Diffuse Galactic Light by Local-Structure Method . . . . .	50
4.7	ZL polarization . . . . .	51
4.8	Summary of the Data Reduction and Analysis . . . . .	61
<b>5</b>	<b>Result and Discussion</b>	<b>63</b>
5.1	Zodiacal Light . . . . .	63
5.1.1	Spectrum of Zodiacal Light . . . . .	63
5.1.2	Discussion on Spectrum of Zodiacal Light . . . . .	65
5.1.3	Polarization of Zodiacal Light . . . . .	74
5.1.4	Discussion on Polarization of Zodiacal Light . . . . .	80
5.1.5	Summary of Zodiacal Light . . . . .	83
5.2	Diffuse Galactic Light . . . . .	84
5.2.1	Spectrum of Diffuse Galactic Light . . . . .	84
5.2.2	Discussion on Spectrum of Diffuse Galactic Light . . . . .	86
5.3	Summary of Discussion of Zodiacal Light and Diffuse Galactic Light	90
5.4	Limit on Extra-Galactic Background Light (EBL) . . . . .	91
<b>6</b>	<b>Conclusion</b>	<b>97</b>

# Chapter 1

## Introduction

### 1.1 Near-Infrared Diffuse Sky Brightness

It has been known that the brightness of the night sky is an important astronomical information since early history of astronomy, e.g., Olbers pointed out that uniform distribution of stars in infinite volume of the universe should produce infinite brightness of the night sky, which is different from the observation, called "Olbers' paradox" (Olbers 1826). Olbers' paradox suggests a possibility to investigate the universe by measuring the total sky brightness, and this is a pioneering work on the diffuse radiation measurement. In such early days, the authors dealt primarily with integrated starlight, and they didn't know the existence of truly diffuse emissions caused by cosmic dust in local universe, such as Zodiacal Light (ZL) and Diffuse Galactic Light (DGL).

Figure 1.1 shows overview on the brightness of the sky outside the lower terrestrial atmosphere and at high ecliptic and galactic latitudes. In the near-infrared wavelength, the diffuse night sky brightness consists of atmospheric airglow emission (simply, hereafter airglow emission), ZL, integrated light of faint star and DGL. The airglow emission is a dominant component in the total diffuse radiation, and 200-1500 times brighter than the astronomical emission. Airglow emission has time variable structure (Ramsay et al. 1992) with spatial variations that increase on large angular scales, especially from  $1^\circ$  to  $10^\circ$ . The airglow emission confronts the observation of astronomical emission from the ground. Thus, we

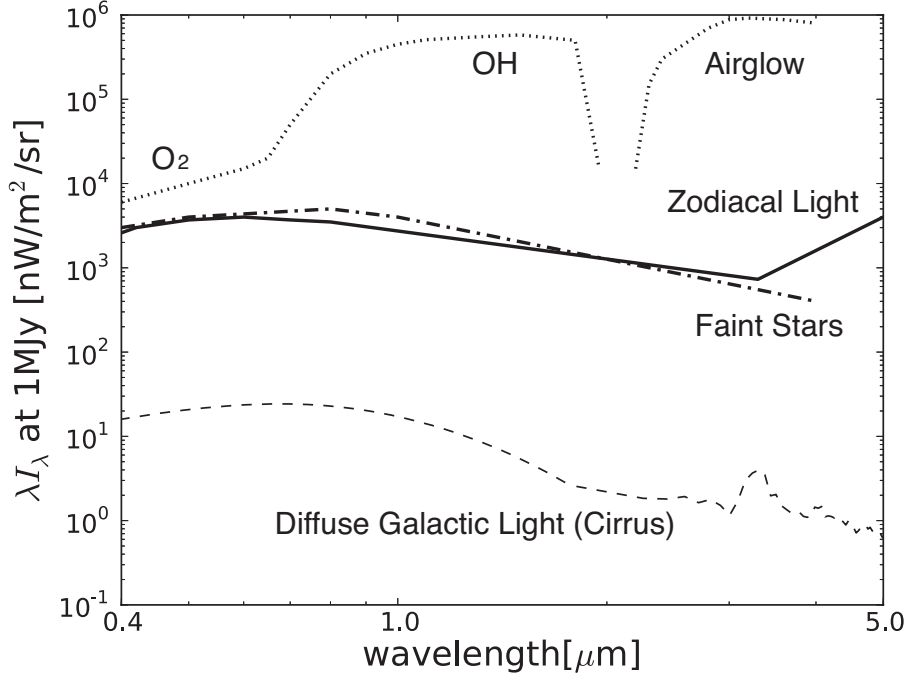


Figure 1.1: Components of diffuse radiation outside the lower terrestrial atmosphere and at high ecliptic and galactic latitude (Leinert et al. 1998). Zodiacal light as well as the integrated stars light is given for the South Ecliptic Pole ( $l = 276^\circ$ ,  $b = -30^\circ$ ). The cut-off magnitude for bright stars is  $V = 6.0$  mag for  $0.3\text{-}1\mu\text{m}$ . Stars brighter than 15 Jy between  $1.25$  and  $4.85\mu\text{m}$  are excluded for  $1\text{-}3\mu\text{m}$ . The data are from the following references: zodiacal light: Leinert & Grun (1990); integrated starlight:  $\lambda \geq 0.3\mu\text{m}$ , Mattila (1980); diffuse galactic light:  $\lambda < 1.8\mu\text{m}$ , Brandt & Draine (2012),  $\lambda = 1.8 - 5.0\mu\text{m}$ , Tsumura et al. (2013c).

conducted observations by a sounding rocket flight, at altitudes above the layers in the atmosphere responsible for airglow emission at characteristic altitude of  $\sim 100\text{km}$ .

In case of the space-based observation, the brightness of astronomical emission,  $I_{sky}$ , is predominated by the ZL brightness,  $I_{ZL}$ , in the near-infrared. ZL is scattered sunlight by interplanetary dust particles. In Figure 1.1, integrated light of faint stars  $I_{ISL}$ , also dominates the brightness of astronomical emission. However,  $I_{ISL}$  depends on how deep we remove the stars that contribute to the diffuse brightness. The brightness of DGL,  $I_{DGL}$ , is scattered stellar radiation by interstellar dust (sometimes, it is called as 'IR cirrus'). Extra-galactic Background Light (EBL) integrated all photons from outside of our Galaxy is not shown in Figure 1.1. Therefore, the astronomical diffuse emission can be expressed as follows.

$$I_{sky} = I_{ZL} + I_{DGL} + I_{ISL} + I_{EBL} \quad (1.1)$$

The astronomical diffuse emission provides wealth information about interplanetary dust and interstellar dust. The scattering spectra and polarization by interplanetary dust and interstellar dust can give valuable information of the size distribution, shape, refractive index, and input radiation. However, the ZL spectrum and polarization are not well known in the near-infrared. Because of its intrinsic faintness and contamination of other diffuse radiation, the DGL spectrum has never been observed in the near-infrared. In the following section, we describe current knowledge about ZL and DGL, and unsolved problem in this study.

## 1.2 Zodiacal Light

The brightest component of the astronomical diffuse brightness is zodiacal light (ZL). Therefore, measuring and understanding ZL are important to measure the other diffuse emission including DGL and EBL.

ZL is the scattered sunlight by interplanetary dust particles observed in a wide range from ultraviolet to near-infrared. Measuring ZL is important to understand the structure of interplanetary dust distribution and physical properties of

interplanetary dust; size distribution, composition and refractive index. In addition, the information obtained from the ZL measurement is important for future studies of dust disks of extra-solar planetary systems.

Structure of the interplanetary dust distribution is typically called as 'zodiacal cloud' or 'interplanetary dust cloud', and its observational study has been done by many authors. There is a smoothly distributed dust component with only large-scale structure from mixing of dusts associated with asteroidal and cometary debris, typically termed 'smooth cloud'. In addition to the smooth cloud, there are contributions from smaller scale structures. An asteroidal dust bands were found by IR Astronomical Satellite (Neugebauer et al. 1984, IRAS), and confirmed by Diffuse Infrared Background Experiment board on Cosmic Background Explorer (DIBER/COBE) (Low et al. 1984; Spiesman et al. 1995). A circumsolar ring which arises from dust spiraling in from the outer solar system and being resonantly trapped by the earth in orbits near 1 AU was confirmed from the DIRBE data (Reach et al. 1995). The number density decreases with increasing heliocentric distance,  $n(r) \sim r^{-\nu}$ , Levasseur-Regourd (1996) derived  $\nu = 0.93 \pm 0.07$ . This result is consistent with  $\nu = 1$  which is expected from the equilibrium distribution of the dust under the Poynting-Robertson drag.

The ZL brightness is dependent on viewing direction, heliocentric distance and position of the observer in the zodiacal cloud because of its non-uniform structure Figure 1.2. Dependence of the ZL brightness on viewing direction was measured with IRAS(12-100 $\mu\text{m}$ ) and DIRBE/COBE(1-240 $\mu\text{m}$ ) in whole sky for both the scattered light and the thermal emission (Boggess et al. 1992; Silverberg et al. 1993). The heliocentric dependence of the ZL brightness relative to the value at 1AU was measured with Helios experiments, to be  $I(r)/I(1AU) = r^{-2.3 \pm 0.1}$  and with Pioneer 10 to be  $I(r)/I(1AU) = r^{-2.5 \pm 0.2}$  for the solar elongations between  $16^\circ$  to  $160^\circ$  (Leinert et al. 1980; Hanner et al. 1976). Since the symmetry plane of the zodiacal cloud is tilted from the Earth's orbital plane by  $\sim 3^\circ$ , the brightness of ZL varies with season (Kelsall et al. 1998). The annual variation was observed with IRAS and COBE/DIRBE(Boggess et al. 1992; Silverberg et al. 1993) in a wide range from near-infrared to far-infrared, and more recently with the Spitzer Space telescope (Krick et al. 2012) in the mid-infrared. The Spitzer result showed a few percent deviation from the ZL model (Kelsall et al. 1998), which is based



Figure 1.2: ZL from Mauna Kea.

on the DIRBE/COBE data. From this result, Krick et al. (2012) found an under-prediction of the amplitude of the annual variation by the model, and suggested the presence of an over density behind the earth and evidence for a warping in the interplanetary dust cloud. The ZL brightness does not vary with the solar cycle to less than one percent (Dumont & Levasseur-Regourd 1978; Leinert & Pitz 1989).

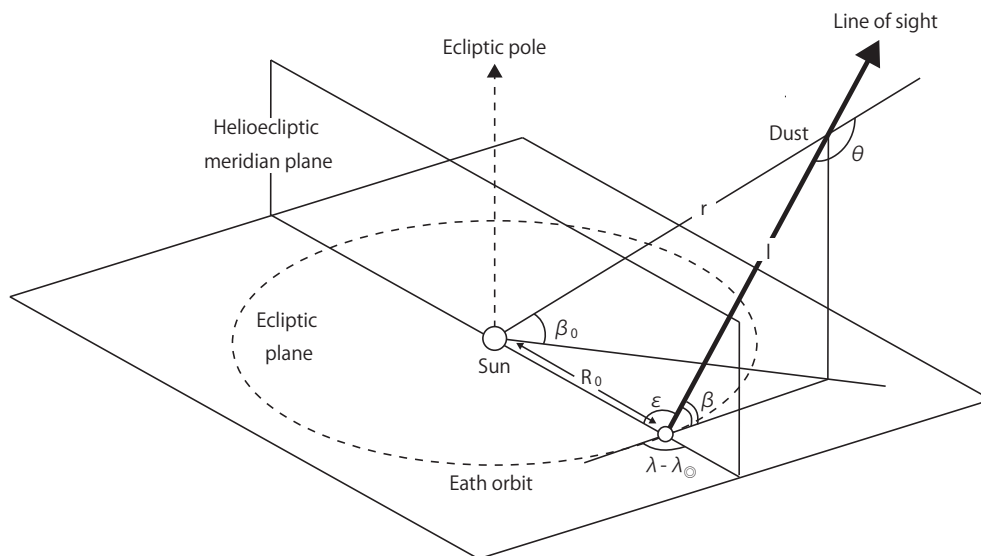


Figure 1.3: Basic geometry of observation of ZL (Matsuura et al. 1995).  $r$  is heliocentric distance of the dust particle.  $R_0$  is heliocentric distance of the observer ( $=1\text{AU}$ ).  $l$  is distance between the scatter and the observer.  $\beta_0$  is heliocentric ecliptic latitude.  $\beta$  is ecliptic latitude.  $\lambda - \lambda_\odot$  is ecliptic longitude.  $\epsilon$  is solar elongation.  $\Theta$  is scattering angle.

Figure 1.3 shows the geometry of the observation of ZL. The observed brightness of ZL can be presented by physical properties of interplanetary dust through an integral of the scattered light along the line of sight. The ZL brightness is expressed as follows.

$$I_{ZL} = F_0 R_0 \int_0^\infty \frac{\bar{\sigma}(\mathbf{r}, \theta) N(\mathbf{r})}{r^2 l^2} dl \quad (1.2)$$

where  $R_0, r, l$  and  $\theta$  are geometric parameters shown in Figure 1.3.  $F_0$  is solar

flux at observer (1AU).  $\bar{\sigma}(\mathbf{r}, \theta)$  is the average scattering function of dust particles (Leinert 1975).  $N(\mathbf{r})$  is number density of the dust. The average scattering function is obtained as the weighted mean respecting to the physical properties of the dust particles such as size, refractive index and shape. As an example, the weighted mean for the size distribution is expressed as follows.

$$\bar{\sigma}(\theta) = \frac{\int \sigma(s, \theta) \cdot n(s) ds}{\int n(s) ds} \quad (1.3)$$

where  $s$  is the size of dust particles,  $n(s)$  is the size distribution function,  $\sigma(s, \theta)$  is a scattering function for the particles of size  $s$ . Thus, it is important to understand the size distribution and the scattering function of interplanetary dust.

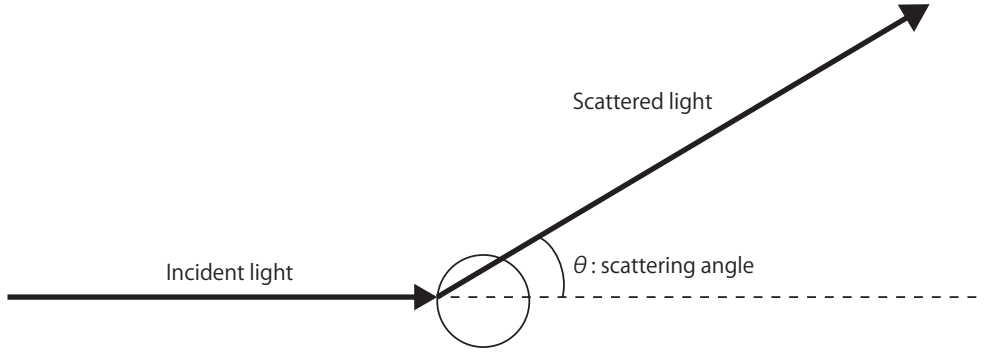


Figure 1.4: Scattering by a particle.  $\theta$  indicate the scattering angle.

The scattering function depends on the refractive index, size, and shape of the dust particles. The general relation between the scattering function and the size of the dust particles is well known. When the size of the dust particles is smaller than the wavelength;  $2\pi a/\lambda \ll 1$  ( $a$  is the size of particle), the scattering behavior can be approximated by Rayleigh scattering theory. The scattering function of the Rayleigh scattering is expressed as,  $\sigma(\theta) = 1 + \cos(\theta)$ . If the geometrical optics is valid for  $2\pi a/\lambda \gg 1$ , the scattering behavior can be approximated by Fresnel scattering theory. If the size is comparable to the wavelength,  $2\pi a/\lambda \approx 1$ , the scattering behavior is represented by the Mie theory. Figure 1.5 shows the scattering function for the Rayleigh scattering and the Fresnel scattering. The definition of the scattering angle is shown in Figure 1.4. To see general dependence

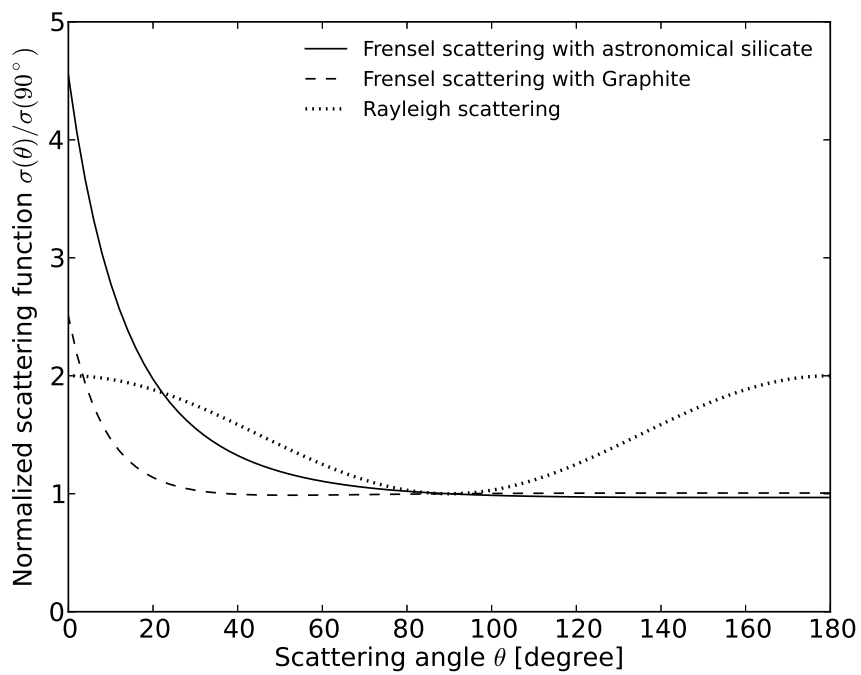


Figure 1.5: The scattering function as a function of the scattering angle (Bohren & Huffman 1983).

of the scattering function on the refractive index, we present example of the calculation of the Fresnel scattering for two different typical materials of the dust.

Size distribution is an important factor to characterize the interplanetary dust property. As shown in Matsumoto et al. (1996) and Tsumura et al. (2013b), the ZL spectrum is similar to the solar spectrum in the near-infrared from  $1.4\mu\text{m}$  to  $5\mu\text{m}$ . An early result of CIBER indicates the reddening of the ZL in a range from  $0.8\mu\text{m}$  to  $1.4\mu\text{m}$  (Tsumura et al. 2010). Neutral or red color of ZL means that dust particles larger than the wavelength, i.e.  $>5\mu\text{m}$ , are mainly responsible for ZL, because the scattering of small particles results in the prevalence of blue color. In addition, Reach et al. (2003) shows that large particles ( $10\text{-}100\mu\text{m}$  in radius) dominate the continuum of zodiacal emission in  $5\text{-}16\mu\text{m}$ .

In addition to the spectral measurements of ZL, direct measurement of the interplanetary dust flux provides us to an reliable information on the size distribution. The dust flux measurement have been carried out the 1970's by space-borne experiments. Dust detectors on board space probes measure the impact signal using various techniques such as capacitor or pressurized cell penetration sensors and impact ionization detectors. Although the mass distribution of dust particles are yielded by the analysis of the impact signal, we can convert from the mass distribution to the size distribution using an assumed material density as follows.

$$s = \left( \frac{3m}{4\pi\rho} \right)^{\frac{1}{3}} \quad (1.4)$$

where  $m$  and  $\rho$  are the mass and the density of interplanetary dust particles. We use the density of  $\rho = 2.5\text{gcm}^{-3}$  which is a typical value for stony materials in the earth. Grun et al. (1985) derived the mass distribution of the interplanetary dust near the earth from the impact measurements with detectors on board various spacecrafts such as Pegasus, Explorer 16/23, HEOS 2 and Pioneer 8/9 and from the lunar microcrater record. Top panel of Figure 1.6 shows the mass distribution measured by Grun et al. (1985) as a function of particle. The cross-sectional area of interplanetary dust is an important quantity, because amplitude of the scattered light is proportional to the cross-sectional area,  $G(m) = \pi s^2$ . Bottom panel of Figure 1.6 shows the cross sectional distribution as a function of the

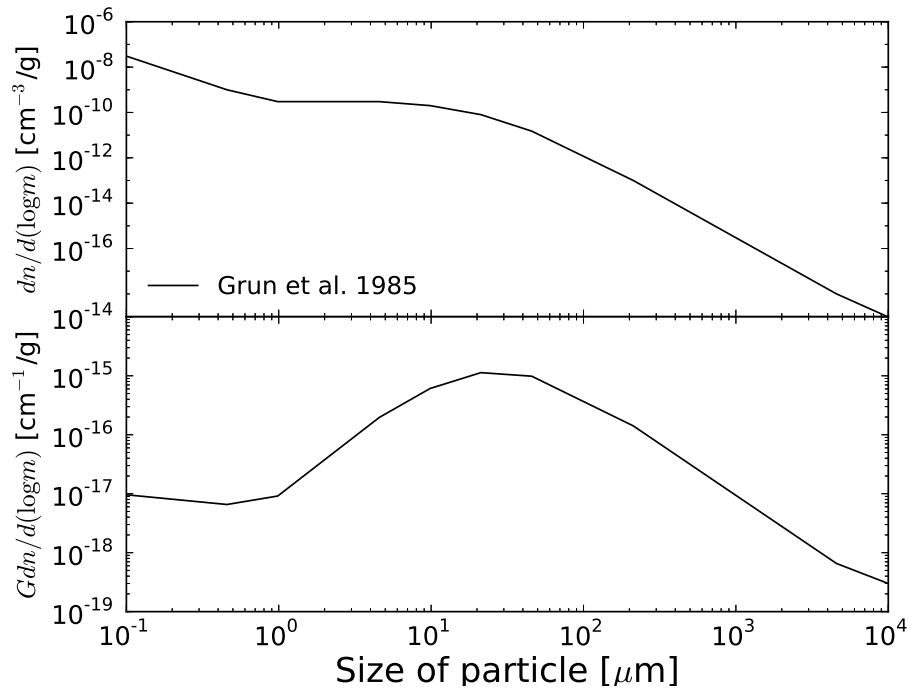


Figure 1.6: The size distribution and the cross sectional distribution of interplanetary dust for  $\rho = 2.5\text{gcm}^{-3}$  at the earth's orbit, corresponding to the mass distributions derived by Grun et al. (1985).

particle size. This result indicates that ZL is predominated by  $s = 10 - 100\mu\text{m}$  particles.

Albedo is another important factor to characterize the property of interplanetary dust. Albedo is defined as the ratio of the scattered light to the total extinction including the absorption as follows.

$$A = \frac{Q_{sca}}{Q_{sca} + Q_{abs}} \quad (1.5)$$

where  $Q_{ext}$  and  $Q_{abs}$  is the scattering efficiency and absorption efficiency. There is another definition of albedo, 'geometric albedo'. The geometric albedo defined as the ratio of the energy scattered by a particle to the energy scattered by a white Lambert disk having the same geometrical cross-section.

$$A_g = \frac{\pi\sigma(\theta)}{G} \quad (1.6)$$

In most case of the ZL study, albedo means the geometric albedo for  $\theta = 180^\circ$ , and it was measured by many authors. Albedo of interplanetary dust was estimated to be 0.09-0.13, combining the spatial distribution and the size distribution of dust at 1AU, which was obtained from the impact measurement of micrometeoroids and lunar microcrater analysis (Grun et al. 1985). An albedo was also derived from IRAS measurements to be  $0.08 \pm 0.1$  at 1AU, and dependence on heliocentric distance was  $A(r) \sim r^{-0.32 \pm 0.05}$ . Dumont & Levasseur-Regourd (1988) and Renard et al. (1995) studied properties of zodiacal cloud by using 'nodes of lesser uncertainty' method, and they obtained an albedo at 1AU of 0.08-0.15 at a scattering angle of  $90^\circ$ , which is translated to the geometric albedo of 0.16-0.30 (Hong 1985; Levasseur-Regourd 1996). Ishiguro et al. (2013) observed Gegenschein where a strong intensity peak of ZL toward the anti-solar direction. They derived the geometric albedo of  $0.06 \pm 0.01$  in the optical band. These results of the ZL measurements are consistent with the fact that micrometeorites accumulated around Earth orbit have low albedo  $< 0.1$  (Brownlee 1978; Hanner 1980).

The ZL polarization is also an important quantity to study the interplanetary dust property. The polarization depends on the size distribution, shape, refractive index. In the same way as the scattering function, the degree of polarization as a function of the scattering angle is shown in Figure 1.7. There is

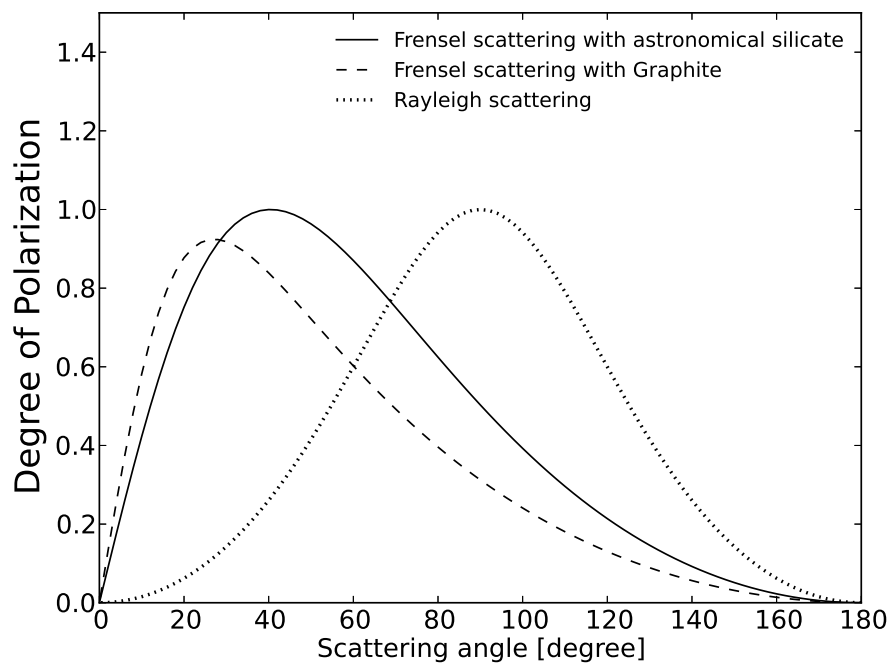


Figure 1.7: The degree of polarization as a function of scattering angle.

a clear difference of polarization between Fresnel scattering and Rayleigh scattering. There is also difference of polarization between astronomical silicate and graphite. Figure 1.8 shows the measured wavelength dependence of polarization of ZL (Leinert et al. 1998). The polarization was measured mostly at optical wavelengths. DIRBE/COBE also measured the polarization in the near-infrared. However, due to the contamination of other diffuse radiation, there is still large uncertainty in the polarization measurements. Thus, an accurate measurement of the ZL polarization is required to probe the physical property of interplanetary dust.

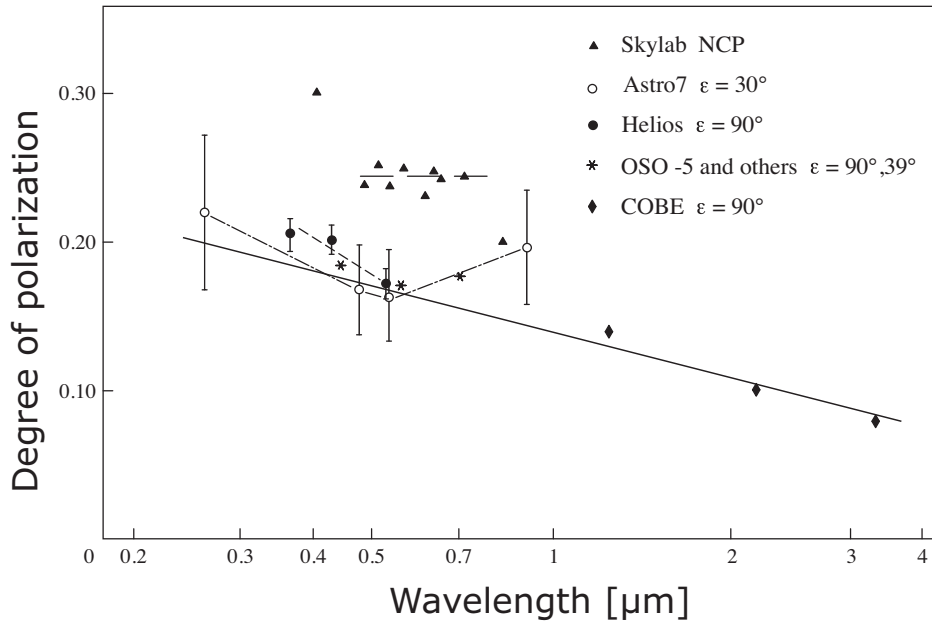


Figure 1.8: Wavelength dependence of polarization of ZL (Weinberg & Hahn 1980). Filled triangle: skylab at the north celestial pole (Pitz et al. 1979) Open circles: rocket Astro 7 at elongation  $\epsilon = 90^\circ$  (Sparrow & Ney 1972, balloon at  $\epsilon = 30^\circ$  (Van de Noord 1970), ground-based  $\epsilon = 39^\circ$  (Wolstencroft & Brandt 1967). Diamonds is DIRBE/COBE result (Berriman et al. 1994). The solid line shows the approximation  $P(\lambda) = p(0.5\mu\text{m})[1 + 0.59 \log(\lambda/0.5\mu\text{m})]$ .

Many of recent studies support that cometary dust is the origin of interplane-

tary dust. Nesvorný et al. (2010) compared their dynamical simulations of interplanetary dust with the IRAS data, and suggested that 85-95% of the observed mid-infrared emission is produced by particles from Jupiter-family comets (JFCs) and <10% by dust from long-period comets. Fernández et al. (2006) showed that geometric albedo of a comet 162P/Siding Spring (P/2004 TU<sub>12</sub>), which is largest radii known among JFCs, is  $0.059 \pm 0.023$  in the H band,  $0.037 \pm 0.014$  in the R band, and  $0.034 \pm 0.013$  in the V band. Soderblom et al. (2002) also measured JFCs 19P/Borrelly and derived a geometric albedo of  $0.03 \pm 0.05$ . These results indicate that interplanetary dust is dominated by low albedo (< 0.1) particles, and is similar to cometary dusts. A combination of amorphous and crystalline silicate grains features was shown in spectral measurements at 9-11 $\mu$ m (Ootsubo et al. 1998; Reach et al. 2003; Ootsubo et al. 2009). The crystalline silicates feature was detected in numerous comets and the collected interplanetary dust particles. On the contrary, the near-infrared spectrum showed similar shape to the reflection spectrum of S-type asteroid, and this analogy suggests that high-albedo particles may dominate in the dust composition near Earth orbit (Tsumura et al. 2010; Matsumoto et al. 1996). The geometric albedo of an S-type asteroid Itokawa was measured to be  $0.25 \pm 0.14$  at I-band (Lederer et al. 2005). Therefore, the asteroid origin of interplanetary dust is not supported from the study in terms of the albedo. Further investigation is required on the fraction of asteroidal particles with respect to cometary dust particles.

The size distribution, composition and origin of interplanetary dust are not fully understood. To investigate these properties, it is important to understand the spectrum nature of the light scattering of interplanetary dust, such as spectral reflectance and polarization. In order to understand interplanetary dust, it is necessary to measure the ZL spectrum in wide wavelength range, especially the near-infrared. In addition, measurement of the polarization spectrum of ZL is also important to obtain independent information about the property of interplanetary dust. However, such observation has never been conducted.

## 1.3 Diffuse Galactic Light

Diffuse Galactic Light (DGL) is the scattered stellar radiation by interstellar dust grains. The DGL spectrum has information of size distribution, composition, and physical environment of interstellar dust, same as the case of ZL.

Historically, DGL has been observed mostly in the optical band. The first photometric measurement was carried out by Elvey & Roach (1937) at  $\lambda = 0.45\mu\text{m}$ . Following the observation, the photometric measurements were conducted by many authors, and they revealed that DGL is starlight scattered off by interstellar medium (Elvey & Roach 1937; Henyey & Greenstein 1941; van de Hulst & de Jong 1969; Elsässer & Haug 1960; Wolstencroft & Rose 1966; Mattila 1979).

After the IRAS discovered diffuse far-infrared emission by interstellar dust (Low et al. 1984, IRAS original map), measurements of extinction (de Vries & Le Poole 1985; Laureijs et al. 1987) and emission of CO molecules (Stark 1995) in interstellar medium indicate that spatial distribution of DGL is well correlated with that of the far-infrared emission. Zagury et al. (1999), Paley et al. (1991), Guhathakurta & Tyson (1989), and Laureijs et al. (1987) measured the DGL distribution around reflection nebula correlating with the IRAS original map in the optical wavelength.

Because the IRAS map had large uncertainty in absolute calibration, Schlegel et al. (1998) revised the IRAS map using absolute calibration of COBE/DIRBE map, hereafter SFD- $100\mu\text{m}$  map. Many recent studies used the SFD- $100\mu\text{m}$  map to measure DGL. Witt et al. (2008) observed optically thin high galactic latitude clouds and found extended red emission in spectral energy distribution of DGL. Matsuoka et al. (2011) measured DGL in one quarter of the entire sky at galactic latitude  $|b| > 35^\circ$  using Pioneer 11/10 data. Ienaka et al. (2013) measured the DGL in B, g, V and R-band in a  $45' \times 45'$  field containing part of the high galactic latitude translucent cloud MBM32. The first spectral measurement was succeeded by Brandt & Draine (2012) using blank-sky spectra from the Sloan Digital Sky Survey (SDSS) in large part of the sky.

On the other hand, DGL has not been measured in the entire near-infrared wavelength range, because the airglow emission due to OH emission in the atmosphere is too high to measure DGL from the ground. At long near-infrared

wavelengths beyond  $2\mu\text{m}$ , Tsumura et al. (2013c) measured the spectrum of DGL using AKARI satellite and detected polycyclic aromatic hydrocarbons (PAHs) emission at  $3.3\mu\text{m}$ , which indicates the existence of very small grains such as nano-meter size particles.

The size distribution and composition of interstellar dust are still under discussion. Many authors constructed models to explain the observed extinction from the near-infrared to the ultraviolet. Mathis et al. (1977) explained the observed extinction using amorphous silicate, carbonaceous material with power-law size distribution as  $dn/da \propto a^{-3.5}$ , called 'MRN' size distribution. After this study, many authors tried to explain the observed extinction by constructing models. However, the size distribution of interstellar dust is still under discussion, and much more observational information on interstellar dust particles is required.

To investigate the size distribution of interstellar dust, the measurements of DGL in wide wavelength range are important. As shown in previous section, the scattered light includes wealth information about the dust size. Especially in the wavelength range of  $0.8\text{-}2.0\mu\text{m}$ , the measurement of continuous spectrum of DGL has been lacking as shown in Figure 1.9. Because of its intrinsic faintness and contamination of other diffuse light, the DGL measurement is difficult in the near-infrared. However we succeeded to measure the spectrum of DGL in  $0.8\text{-}2.0\mu\text{m}$  for the first time by using LRS (Tsumura et al. 2013a, Low Resolution Spectrometer) for the CIBER (Bock et al. 2006; Zemcov et al. 2013, Cosmic Infrared Background Experiment) rocket experiment, thanks to its very high sensitivity which has never been achieved with the other experiments.

## 1.4 Extra Galactic Background Light

After the epoch of recombination at  $z \sim 1100$ , the universe entered the dark ages when there is no light source like stars and galaxies. The first luminous objects formed and reionized the surrounding intergalactic gas after the dark age.

Most direct way to understand the history of star formation, and the reionization is to measure the first luminous objects. However, these objects are too far from us and too dim to detect. On the other hand, their integrated light could

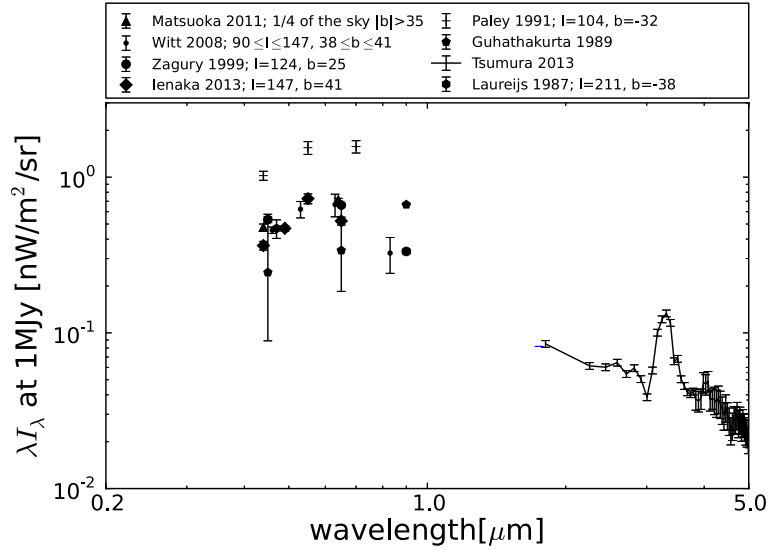


Figure 1.9: The DGL brightness as a function of wavelength from 0.5 to  $5.0\mu\text{m}$  at the  $100\mu\text{m}$  brightness of  $1\text{MJy}\text{sr}^{-1}$ .

be detected as a diffuse emission component of extragalactic background light (EBL).

EBL is the integrated intensity of all of the photons emitted along a line of sight through the universe. Since at near-IR (infrared) wavelengths EBL is thought to be dominated by direct emission from stars, EBL at these wavelengths gives an integral constraint on the total energy released via the process of nucleosynthesis through the history of the universe. Such measurements are a key constraint on all models of galaxy formation and evolution, connecting the global radiation energy density to star formation, metal production, and gas consumption from the present back to the epoch of reionization.

We compiled recent measurements of the EBL in near-infrared/optical in figure 1.10 (see Hauser & Dwek (2001) for a comprehensive review). Cambr esy et al. (2001) measured EBL in near-IR with DIRBE/COBE. They found that there is a large discrepancy between the expected EBL from the deep number counts of galaxies (Totani et al. 2001) and the measured EBL brightness. Matsumoto et al. (2005) measured the EBL spectrum in near-IR. In the optical wavelength

region, Bernstein (2007) measured the EBL using the Hubble Space Telescope. Mattila (2003) reprise Bernstein (2007) data. These data present that there is considerable excess over the EBL brightness estimated from the integrated light of known galaxies.

These absolute brightness of the EBL is confronted with systematic uncertainties of subtraction of the zodiacal light foreground. Matsumoto et al. (2005) and Cambr esy et al. (2001) results used a model of interplanetary scattering and emission based on COBE/DIRBE measurements (Kelsall et al. 1998). Optical measurements Mattila (2003) and Bernstein (2007) subtracted zodiacal light based on the observed strength of scattered Fraunhofer lines from a ground based measurement. On the other hands, Matsuoka et al. (2011) used Pioneer 10 data and measured the EBL from heliocentric distances larger than 3.3AU, where the zodiacal light is found to be negligible (Hanner et al. 1974). Therefore the discrepancy between Matsuoka et al. (2011) and large excess brightness of the other measurements in optical may be due to residual zodiacal light. In addition, the color of the EBL in the near-IR is similar to the color of the zodiacal light. Therefore there may be contamination of residual zodiacal foreground in the measured brightness. Thus, understanding the foreground including ZL and DGL is most important to measure the absolute brightness of EBL.

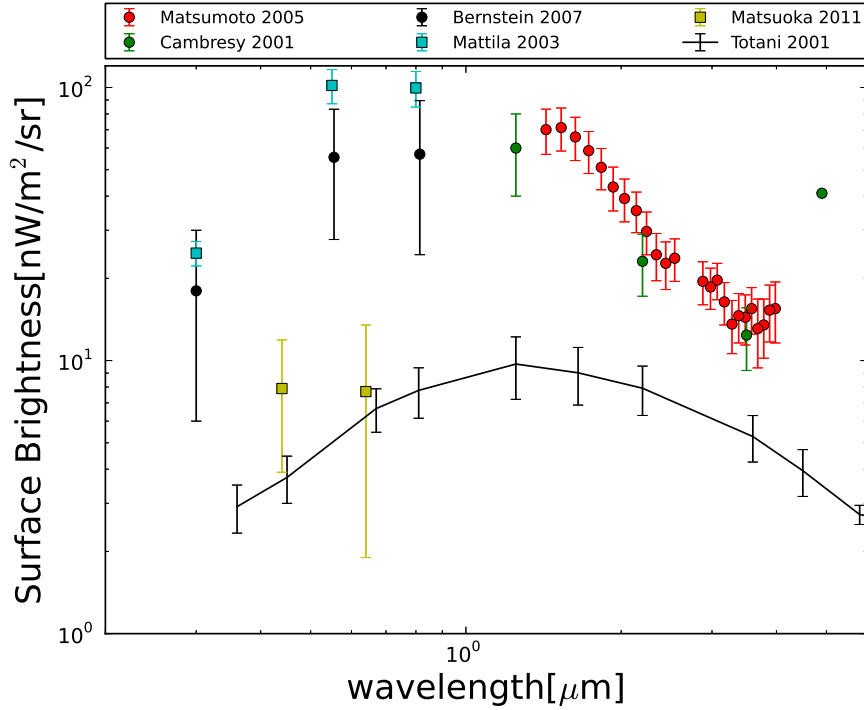


Figure 1.10: EBL at near-IR and optical wavelengths, showing upper limits, reported after subtraction of local foregrounds, and integrated galaxy counts. Green circles present the EBL (Cambresy et al. 2001) measured with COBE/DIRBE. Red circles indicate the spectrum of the EBL (Matsumoto et al. 2005) measured with AKARI. Blue squares and black circles shows optical EBL (Mattila 2003; Bernstein 2007) measured with HST. The yellow squares are observed by Matsuoka et al. (2011) from heliocentric distances  $>3\text{AU}$  using Pioneer 10 data. The black line present integrated galaxy counts calculated by Totani et al. (2001)



## Chapter 2

# CIBER Rocket Experiment

インターネット公表に関する使用承諾が雑誌社（出版社）から得られていないため、本性については非公開。以下の論文を参照。

[ The Cosmic Infrared Background Experiment (CIBER): A Sounding Rocket Payload to Study the near Infrared Extragalactic Background Light ] Zemcov M., Arai T., Battle J., Bock J., Cooray A., Hristov V., Keating B., Kim M. G., Lee D. H., Levenson L. R., Mason P., Matsumoto T., Matsuura S., Nam U. W., Renbarger T., Sullivan I., Suzuki K., Tsumura K., Wada T., 2013, ApJS, 207, 31

[ The Cosmic Infrared Background Experiment (CIBER): The Low Resolution Spectrometer ] Tsumura K., Arai T., Battle J., Bock J., Brown S., Cooray A., Hristov V., Keating B., Kim M. G., Lee D. H., Levenson L. R., Lykke K., Mason P., Matsumoto T., Matsuura S., Murata K., Nam U. W., Renbarger T., Smith A., Sullivan I., Suzuki K., Wada T., Zemcov M., 2013a, ApJS, 207, 33



# Chapter 3

## Observation

### 3.1 Field Selection

Because we want to check the respectability of the measurements, change the instruments, and measure the annual variation of ZL, we launched CIBER payload four times. CIBER flew four times, first flight on Feb 25 2009, second on Jul 10 2010, third on March 22 2011, and fourth on Jun 5 2012. From first to second flight, we used a two stage rocket and launched it from White Sands Missile Range. CIBER payload leveled off at 300km using the two stage rocket. The total exposure time in observation was  $\sim 240$ sec. In the fourth flight, he CIBER arrived at 550km using four stage rocket. And the total exposure time was 335sec. The first result of CIBER was reported by Tsumura et al. (2010). However, in the first flight, the observed sky brightness was deeply contaminated by stray light due to thermal emission of the rocket skin. Thus we installed pop-up baffle for the second flight, and successfully reduced stray light to the negligible level (see chapter 2). In this thesis, we use only data from the second flight to the fourth flight.

Our observed fields are listed in table 3.2. We selected the observed field based on ecliptic latitude and the brightness of thermal emission by interstellar dust to separate ZL and DGL from the observed brightness. Since the ZL brightness depends strongly on ecliptic latitude and increase with decreasing ecliptic latitude, at ecliptic latitude  $10^\circ$  (Elat10) the ZL brightness is brighter than the other

Table 3.1: The  $100\mu\text{m}$  brightness interstellar dust in second flight (Schlegel et al. 1998). The ZL brightness is calculated from Kelsall et al. (1998) at  $1.25\mu\text{m}$ .

Field name	SWIRE	NEP	Elat10	Elat30	BootesA
$100\mu\text{m}$ brightness [ $\text{MJysr}^{-1}$ ]	$0.5\pm 0.1$	$2.5\pm 0.6$	$4.1\pm 1$	$1.6\pm 0.4$	$0.6\pm 0.2$
ZL brightness [ $\text{nWm}^{-2}\text{sr}^{-1}$ ]	$244\pm 12$	$235\pm 12$	$487\pm 24$	$363\pm 18$	$319\pm 16$

field. We selected Elat10 and Elat30 field for the ZL separation. It was reported that the DGL brightness correlates linearly with the brightness of interstellar dust emission measured at  $100\mu\text{m}$  for the optically thin case. We therefore select the fields based on the  $100\mu\text{m}$  brightness measured with IRAS (Schlegel et al. 1998) (see figure 3.2 and 3.2). North Ecliptic Pole and Elat10 of second flight have high  $100\mu\text{m}$  brightness. We selected these fields for the DGL separation. As an example, we present the  $100\mu\text{m}$  brightness and the ZL brightness at  $1.25\mu\text{m}$  estimated from the ZL model Kelsall et al. (1998) for the second flight in 5.1.

Figures 3.3 and 3.4 show the time table of before flight and during flight of the second flight, respectively. Figure 3.6 also shows the time table of during flight. To check the stability of the responsivity of the detector, the calibration lamps were operated before and during flight. To measured dark current of the detector, we closed shutter before flight and between science field of BootesA and BootesB.

Table 3.2: Our observed fields. The unit of coordinate is presented by degree.

Field Name	Exposure time	Altitude	(RA, DEC)	( $\lambda$ , $\beta$ )	(l, b)	$\epsilon$
Second flight						
SWIRE ELAIS-N1	83	139-172	(243.07, 55.28)	(207.68, 72.73)	(84.89, 44.62)	92.8
North Ecliptic Pole	67	199-220	(270.87, 66.00)	(279.88, 89.31)	(96.13, 29.81)	90.2
Elat10 ( $\beta = 10^\circ$ )	9	245-310	(234.34, -8.47)	(233.76, 10.71)	(356.88, 46.08)	115.3
Elat30 ( $\beta = 30^\circ$ )	18	314-295	(223.06, 20.66)	(212.82, 35.10)	(23.52, 63.31)	100.3
BOOTES-A	63	288-232	(218.81, 35.12)	(200.75, 46.72)	(58.76, 66.79)	91.2
Third flight						
Lockman	47	202-265	(161.29, 57.99)	(135.50, 45.27)	(149.75, 52.05)	119.6
SWIRE ELAIS-N1	45	284-315	(242.71, 54.69)	(208.96, 72.37)	(84.48, 44.73)	105.7
North Ecliptic Pole	53	320-324	(270.63, 66.44)	(335.37, 89.72)	(96.25, 29.56)	90.0
Elat30 ( $\beta = 30^\circ$ )	26	319-306	(236.99, 9.50)	(232.23, 28.71)	(18.57, 44.84)	139.9
Bootes-B	50	296-244	(217.23, 33.33)	(200.23, 44.85)	(55.32, 68.11)	132.6
Forth flight						
DGL field	65	272-401	(251.97, 68.85)	(153.32, 82.82)	(100.37, 36.17)	88.3
North Ecliptic Pole	60	425-505	(270.82, 66.24)	(316.56, 89.54)	(96.02, 29.48)	90.2
Lockman	50	520-558	(161.23, 58.58)	(135.02, 45.74)	(149.074, 51.65))	70.4
Elat10 ( $\beta = 10^\circ$ )	50	566-557	(190.49, 8.02)	(186.44, 11.53)	(295.80, 70.77)	110.9
Elat30 ( $\beta = 30^\circ$ )	50	577-562	(193.05, 27.96)	(179.77, 30.63)	(111.34, 89.15)	102.7
BOOTES-B	55	555-509	(217.23, 33.18)	(200.33, 44.71)	(54.90, 68.13)	113.2
SWIRE ELAIS-N1	55	395-275	(242.84, 54.77)	(208.99, 72.48)	(84.56, 44.64)	101.7

Table 3.3: The brightness of calibration lamp with photocurrent unit [e-/sec].

Name	A	B	C	D	R1	R2	R3	R4
laboratory	661±1	418±1	575±1	283±1	341±1	409±1	318±1	318±1
flight	665±1	420±1	955±1	280±1	346±1	414±1	396±1	324±1

## 3.2 Flight Performance

### 3.2.1 Stability of Temperature

We already introduce the stability of temperature during flight in figure ?? and ?. The thermal drift during flights is  $<10\mu\text{Ks}^{-1}$ , corresponding to the dark current drift of  $<0.01\text{e-/sec}$ . Because the mean dark current of the LRS detector is  $\sim 0.6\text{e/sec}$ , this is negligible level.

### 3.2.2 Accuracy of Pointing

The payload is governed by the celestial attitude control system based on the feedback of star tracker and gyroscopes. Figure 3.6 shows the track of the line of sight of the CIBER payload. The circle indicates the pointing error. Even if the worst case, the pointing error is less than  $8''$ . Since the resolution of LRS is  $1.4'$ , the pointing accuracy is sufficient for LRS.

### 3.2.3 Stability of Responsivity

To check the stability of responsivity, we install the calibration lamp on LRS. Figure 3.7 shows the image of calibration lamp taken in the laboratory during the flux calibration test of the second flight. Figure 3.8 shows the image of calibration lamp taken during the second flight. Table 3.3 summarizes the brightness of calibration lamp of several region (see figure 3.7). This result indicates that the responsivity does not change beyond 1% from the laboratory test to the flight.

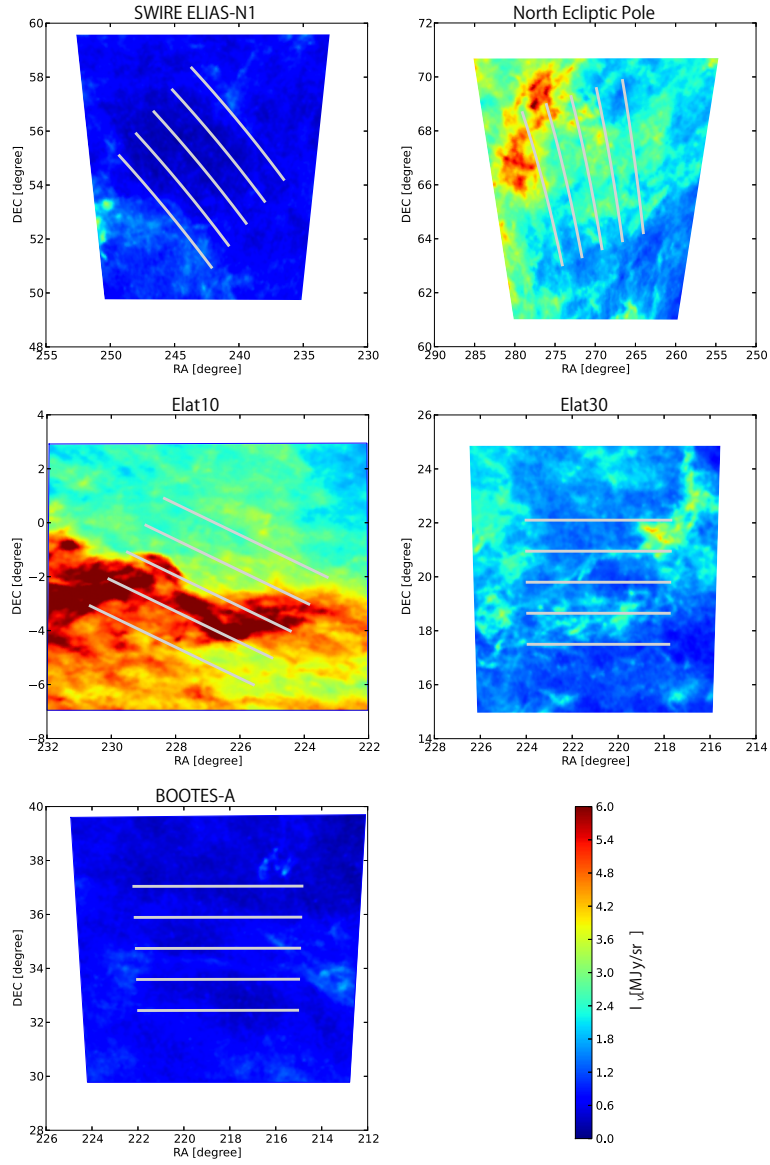


Figure 3.1: The 100 $\mu$ m brightness of our observed field for second flight. The color bar indicate brightness with unit of MJysr<sup>-1</sup> (Schlegel et al. 1998). The five white line indicate the slits of LRS.

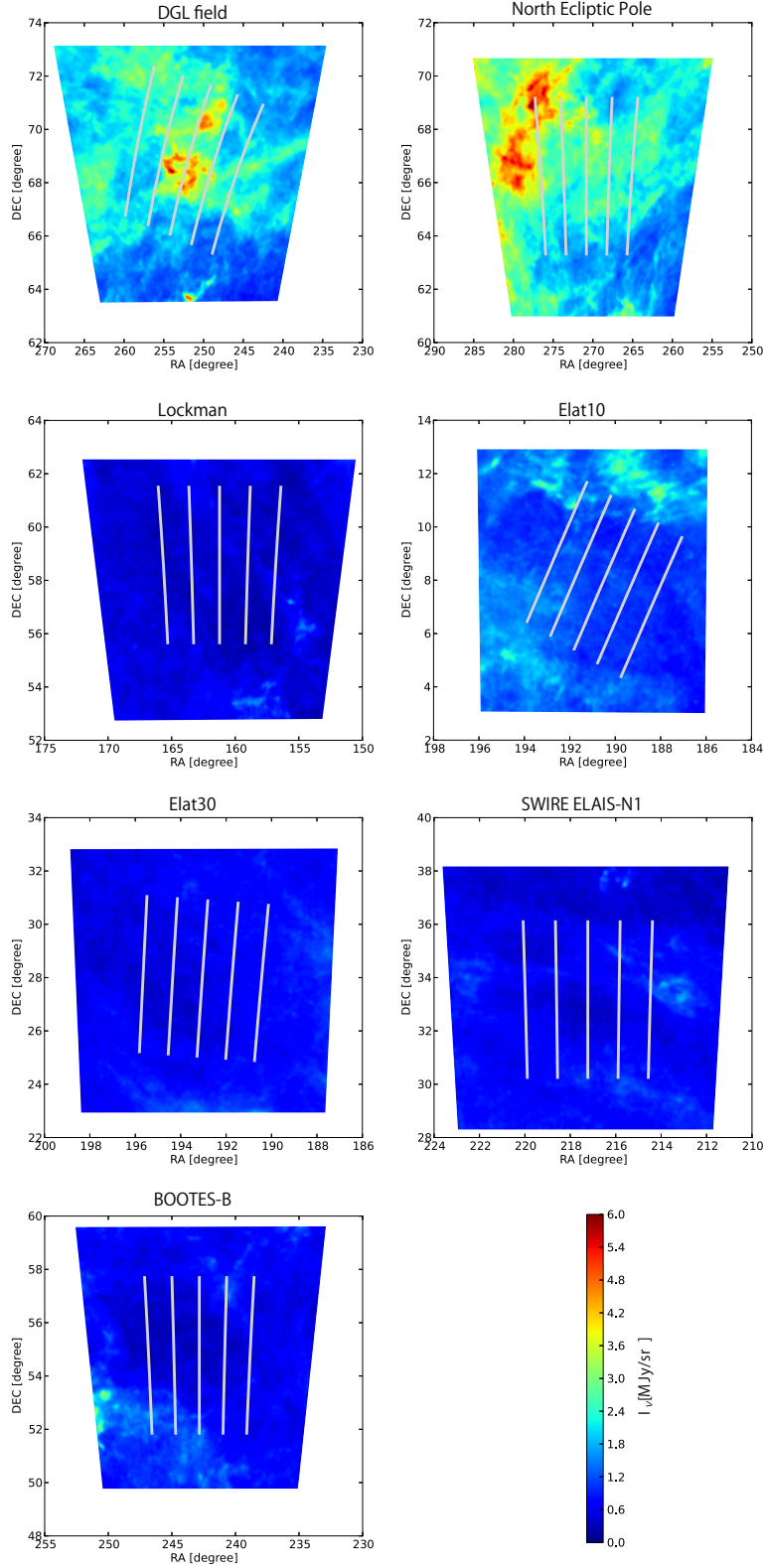


Figure 3.2: The 100 $\mu\text{m}$  brightness of our observed field for fourth flight. The color bar indicate brightness with unit of  $\text{MJy/sr}^{-1}$  (Schlegel et al. 1998). The five white line indicate the slits of LRS.

Sequence	time [sec]	Altitude [km]	Exposure [sec]	Door	Shutter	Calbration lamp	N reset
Shutter Open1	0.00	0.0	112.0	Close	Open	OFF	1
Shutter Open 2	112.25	0.0	2.5				1
Cal on 1	115.00	0.0	51.5			ON	1
Dark1	166.75	0.0	24.25		Close	OFF	1
Dark2	191.25	0.0	87.25				1
Dakr3	278.75	0.0	90.75				1
Dark4	369.75	0.0	82.5				1
Shutter Open 3	452.50	0.0	10.5		Open		1
Cal on 2	463.25	0.0	21.5			ON	1
Shutter Open 3	485.00	0.0	7.75			OFF	1
Cal on 3	493.00	0.0	2.75			ON	1
Shutter Open 4	496.00	0.0	3.5			OFF	1
Shutter Open 5	499.75	0.0	31.75				1

Figure 3.3: Pre-flight sequence for second flight. We conducted several test to check the instruments performance.

Sequence	time [sec]	Altitude[km]	exposure [sec]	Door	Shutter	Calbration lamp	N reset
Launch	0.0	0.0		Close	Open	OFF	
Terrier Burnout	6.2	3.1					
Black Brant Ignition	12.0	6.3					
Black Brant MK1 Burntout	46.2	49.3					
Cal on 4	52.0	62.1	13.75			ON	
Door Deploy	58.0	75.0		Open			
Cla off	67.0	93.6					
Shutter Open 7	82.0	109.6	13.75			OFF	1
Vega	95.0	146.8	2.75				5
Vega	106.0	165.6	2.25				1
Swire	121.0	189.5	83.00				10
NEP	215.0	292.5	56.5				10
Apogee	290.4	317.8					
Elat10	302.0	317.2	9.25				10
Elat30	332.0	310.1	17.75				10
BootesA	363.0	294.3	62.75				10
Shutter Close	427.2	250.0			Close		
BootesA Dark5	427.2	250.0	4.5				0
BootesB Dark6	444.0	212.4	29.75				10
Shutter Open	476.2	163.2			Open		
BootesB	476.2	163.2	35.25	Close			0
Door Close	514.0	92.1	3.25				1
Cal on 5	518.0	84.9	14			ON	1
Shutter Close (Dark5)	534.0	50.6	14.5		Close	OFF	1
Payload Impact	912.6	1.2					

Figure 3.4: In-flight sequence for second flight. We conducted several test to check the instruments performance during flight. The red text indicate science field.

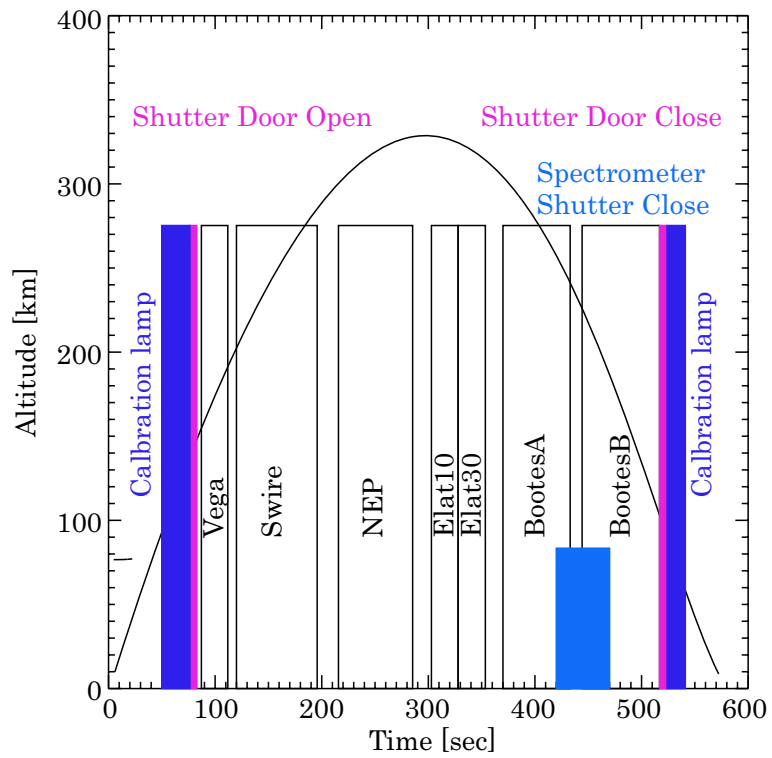


Figure 3.5: In-flight sequence for second flight. The x-axis indicate time from launch. The y-axis indicate the altitude of rocket from the ground.

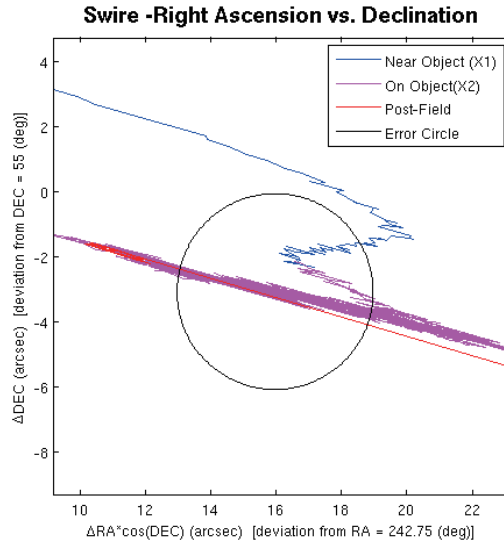


Figure 3.6: The pointing accuracy at the SWIRE of the second flight. The y-axis indicates the error for declination DEC. The x-axis indicates the error for right ascension RA.

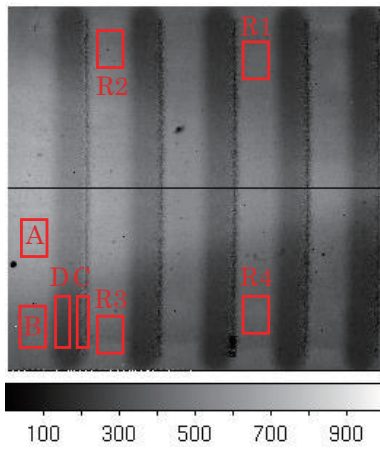


Figure 3.7: The image of calibration lamp in the laboratory at the flux calibration test of the second flight.

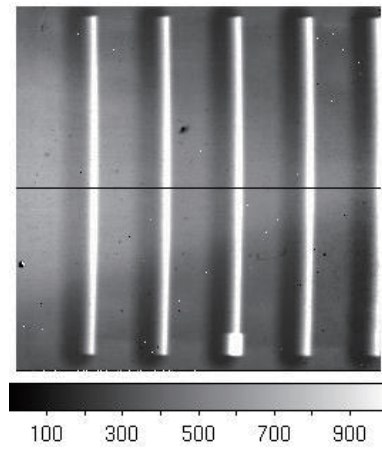


Figure 3.8: The image of calibration lamp during the second flight.

# Chapter 4

## Data Reduction and Analysis

In this chapter, we describe the method of data reduction and analysis. Figure 4.1 shows a flow chart of the data processing. The process starts from the data reduction of the raw data to the raw spectrum at each observation field, followed by the cleaning of the airglow contamination.

Then we process astronomical analysis for the obtained sky spectra  $I_{obs}$  in three ways; (1) separation of Zodiacal Light (ZL) and Diffuse Galactic Light (DGL) from  $I_{obs}$  using their global spatial structure, (2) separation of DGL from  $I_{obs}$  using its local distribution, (3) measuring the polarization of ZL. The results of these processes are compared with each other to check the consistency and also use one result for the other.

### 4.1 Obtaining the Image from the Raw Data

For the charge integrating amplifier of the detector array, the time derivative of the raw signal output from each pixel is proportional to the light power as illustrated in 4.2. We calculate the linear slope of the integrated charge signal with the least-square linear fitting method and obtain the sky input light power in corresponding photocurrent unit. Then we convert the photocurrent to the surface brightness in  $\text{nWm}^{-2}\text{sr}^{-1}$  using the calibration factor derived from the flux calibration.

Figure 4.3 shows a raw image of observation field in photocurrent unit. We

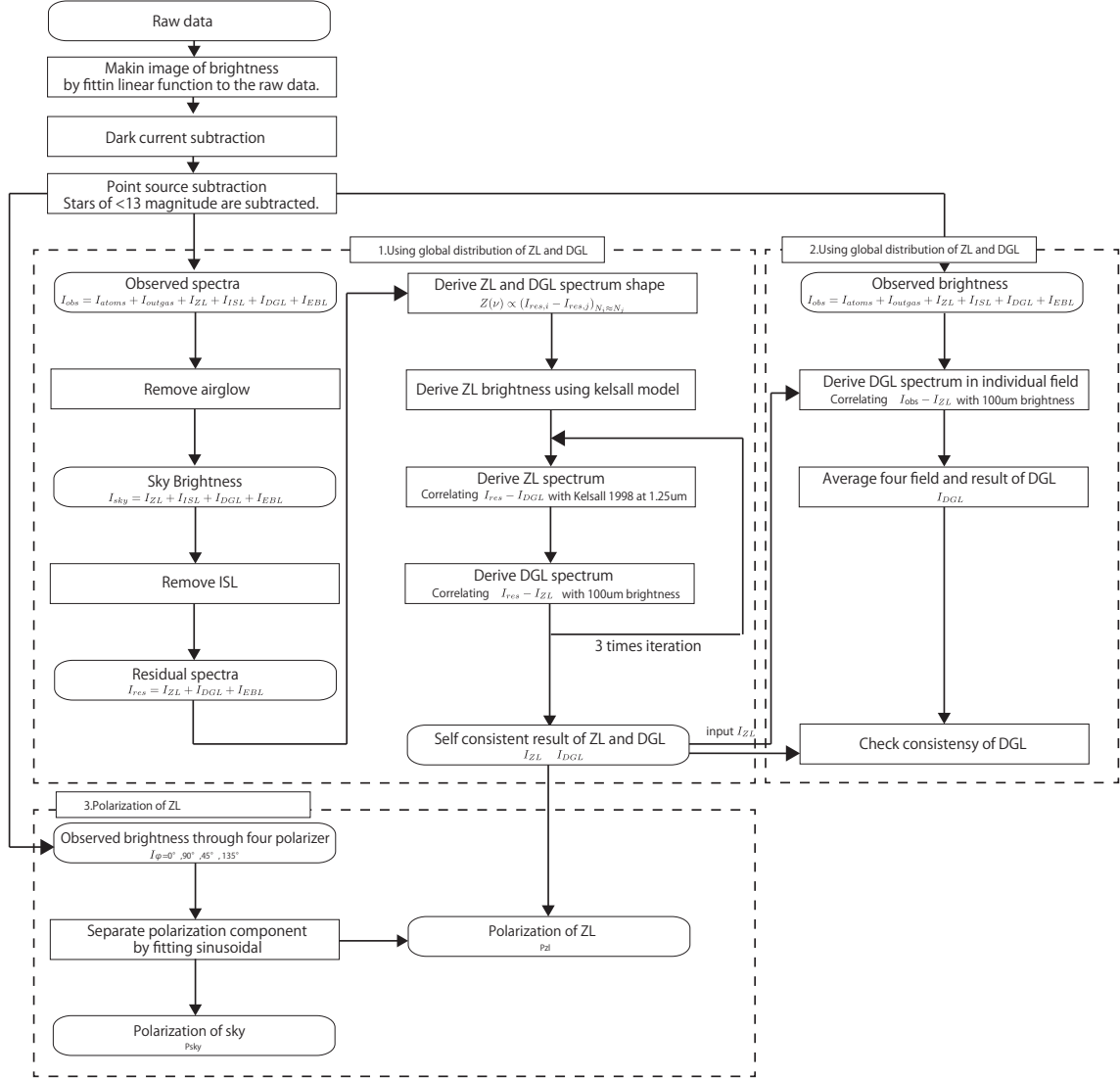


Figure 4.1: Flow Chart: deriving the spectrum of ZL and DGL from the observed brightness.

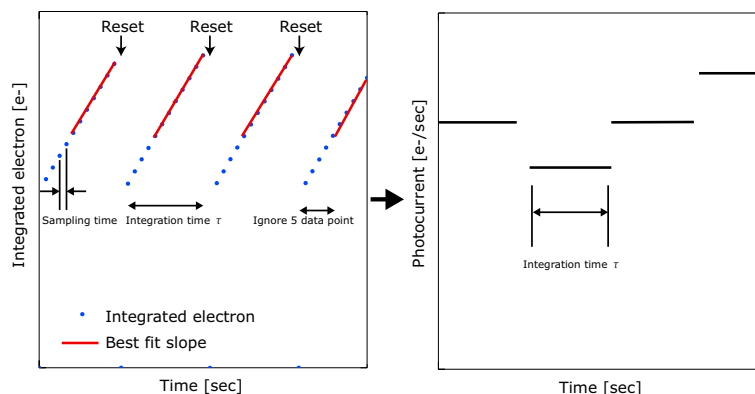


Figure 4.2: The data reduction from the raw data to the differential data.

can see that there are five vertical stripes corresponding to the diffuse light of the five slits of LRS. Dark regions of the top and bottom of the image are masked, to monitor the dark current during the observation. Hereafter, we call this dark region 'masked region'. We call the unmasked region 'FOV region', where the incident light illuminates. We remove the dark current and point sources from such image data.

## 4.2 Subtraction of Dark Current

In absence of incident photons, the HgCdTe infrared detectors always produce a small positive reading for each pixel by the dark current. In order to measure absolute sky brightness, accurate subtraction of dark current is necessary.

Figure 4.4 shows the dark current taken by closing the cold shutter before the launch of the third flight. The median dark current of this image is  $0.82 \pm 0.03$  e-/sec corresponding to the sky brightness of  $\sim 17.9 \pm 0.6$  nWm<sup>-2</sup>sr<sup>-1</sup> at  $1.25 \mu\text{m}$ , which is not negligible compared with the EBL brightness expected from galaxy counts of  $\sim 10$  nWm<sup>-2</sup>sr<sup>-1</sup> (Keenan et al. 2010).

We measured the dark current in the cases of closing the cold shutter and during the observations in both the masked and FOV regions for each quadrant of the detector array shown in Figure 4.4. Figure 4.5 shows the dark current of

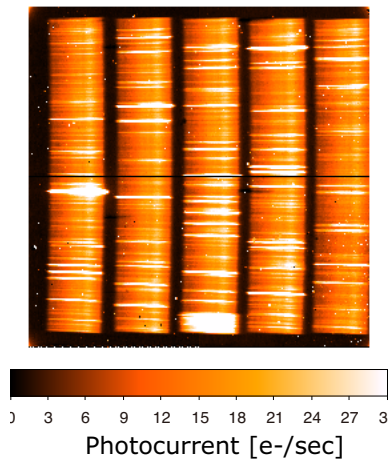


Figure 4.3: A raw image of the detector array in the photocurrent unit taken at an observation field.

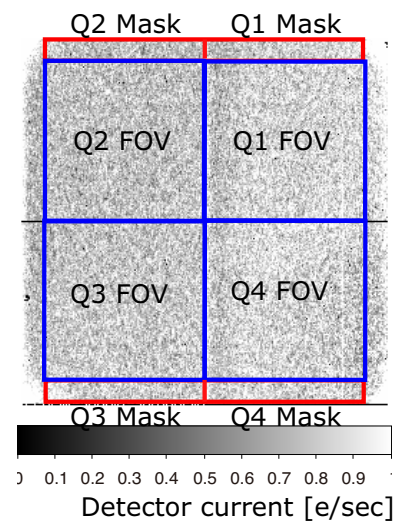


Figure 4.4: The dark current image taken by closing the shutter. The red and blue boxes indicate the masked regions and the FOV regions, respectively.

each quadrant in each flight against the elapsed time after launch.

As see in Figure 4.5, the dark current is not stable during the flight. Thus, we estimate the dark current at each observation field from the masked region for each quadrant.

Since we estimate the dark current only from the masked region, the difference of the dark currents between the masked region and the FOV region causes the systematic error. We measure this difference using the dark current image of the shutter-closed state, and find that the difference current is  $0.03\text{e}^-/\text{sec}$  corresponding to  $\pm 0.7\text{nWm}^{-2}\text{sr}^{-1}$  at  $1.25\mu\text{m}$ . We take this systematic error into account for the measurement error of the sky brightness.

### 4.3 Removal of Bright Star

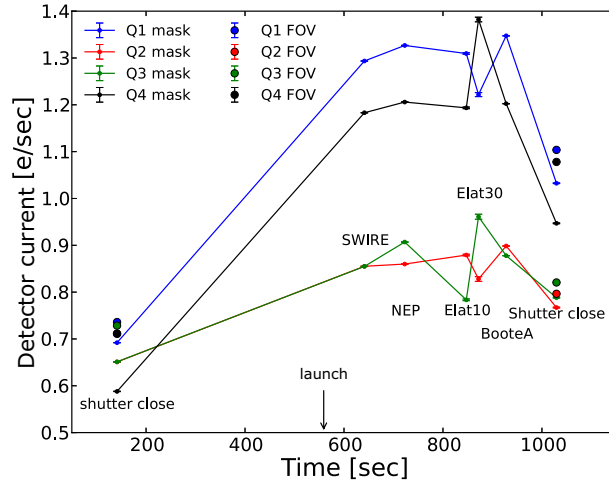
To measure the surface brightness of the diffuse radiation from the obtained image, the point sources of bright stars are removed from the image. Left panel of Figure 4.6 shows the image taken at the NEP field of second flight. One can see that there are many horizontal bright lines. Each horizontal line is a point sources image of the detected star which is dispersed by the prism.

We first integrate the photocurrent of each slits along to the wavelength dispersion direction to improve the signal to noise ratio. The blue line of Figure 4.7 shows the integrated photocurrent. Second, we clip the pixels of the stars, whose photocurrent is above the mean photocurrent of all pixels by  $2\sigma$ , where  $\sigma$  is the standard deviation of the photocurrent. Finally we go back to original images and mask the clipped pixels.

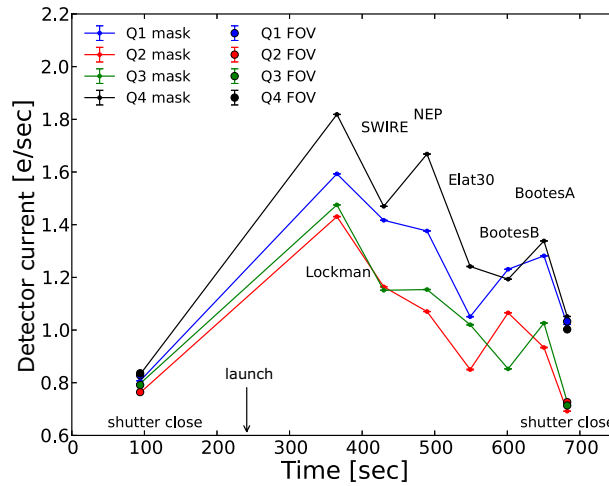
The Right panel of Figure 4.6 is by the masked image. We remove the bright stars found in the images taken by all flights by the same method. 95% of the stars of the 13th magnitude and 63% of the 14th magnitude in the AB system are removed by this method.

#### 4.3.1 Observed Sky Brightness

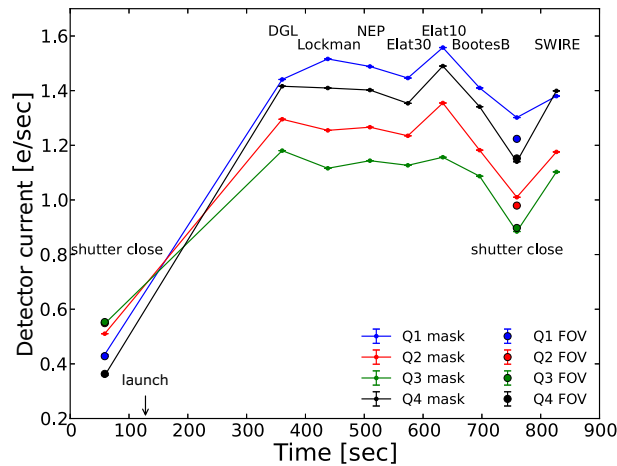
After the above data reduction including obtaining image, dark-current subtraction, and point source subtraction, the mean observed brightness of each field is



(a) Dark current for second flight



(b) Dark current for third flight



(c) Dark current for fourth flight

Figure 4.5: Dark current. The small filled circle present means dark current of all pixels within each masked regions. The large filled circle indicates mean dark current of all pixels within each FOV regions. The uncertainties are estimated from the variance of all pixels in each regions.

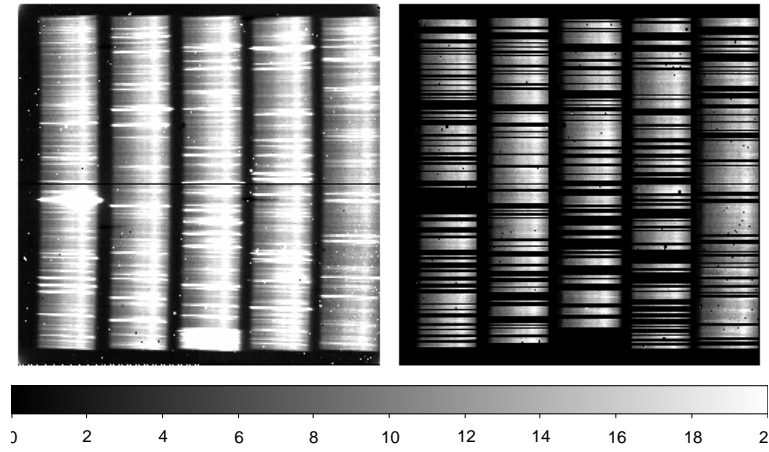


Figure 4.6: Left: original image of the NEP. Right: masked image of the NEP.

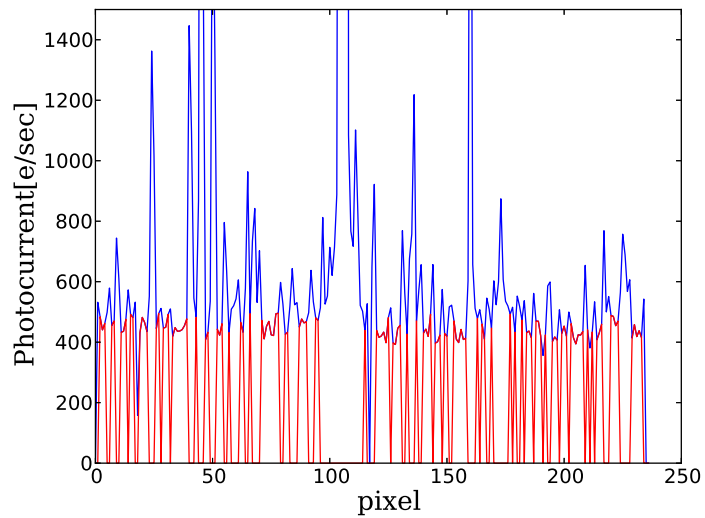


Figure 4.7: The integrated photocurrent of most left slit of the NEP field against pixel number of the slit length direction (space direction) to the wavelength. The blue line indicates original integrated photocurrent. The red line presents residual integrated photocurrent after the  $2\sigma$  clipping.

obtained as shown in Figure 4.8. The sky brightness is calculated by averaging the values of all pixels in the detector array of each field. The error bars are dominated by the flux calibration error, and the statistical error is negligible. Ideally, the observed brightness should consist of only astronomical components: zodiacal light  $I_{ZL}$ , integrated light of faint stars  $I_{ISL}$ , diffuse galactic light  $I_{DGL}$  and extra-galactic background light  $I_{EBL}$ . However, the observed brightness is contaminated by the airglow emission which is composed of stable atmospheric emission showing altitude dependence and time decaying emission may be due to outgassing from the rocket payload. Therefore the observed brightness is written as

$$I_{obs} = I_{airglow} + I_{ZL} + I_{ISL} + I_{DGL} + I_{EBL} \quad (4.1)$$

We must first remove the airglow emission from the observed brightness, to obtain the astronomical sky brightness.

### 4.3.2 Subtraction of Airglow

The contamination by the airglow emission is a serious problem at the beginning of the observation.

The spectrum at the SWIRE field observed at first is obviously contaminated by the airglow emission and different from that of the other field. The altitude dependent component of the airglow decreases with altitude. In addition, amount of out-gas from the payload should decrease with time. Combination of altitude decay and time decay of the airglow emission is clearly seen in the data, as shown in Figure 4.10 and 4.11.

To remove the atmospheric emission and out-gas emission from the observed brightness, we go back to the raw data and construct an exponential decay model of the signal output. The detail of this process is described in Appendix A. We estimate  $I_{airglow} = 327 \pm 16 \text{ nWm}^{-2}\text{sr}^{-1}$  at the SWIRE at  $1.6 \mu\text{m}$ , assuming that time is 183sec from launch and altitude is 278km from the ground.  $I_{airglow} = 22.0 \pm 0.7 \text{ nWm}^{-2}\text{sr}^{-1}$  at NEP field at  $1.6 \mu\text{m}$ . The final sky brightness shown in Figure 4.9 are obtained by subtracting  $I_{airglow}$ .

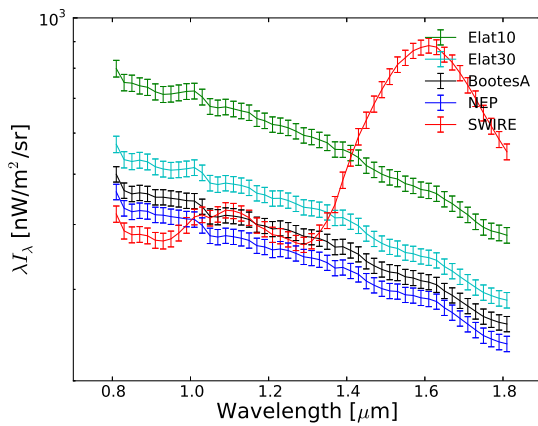


Figure 4.8: The observed brightness of the second flight. The relation between line color and field is presented in the legend. The spectrum shape of the SWIRE field is far different from other field because of the airglow contamination. The error bars are mainly due to flux calibration error.

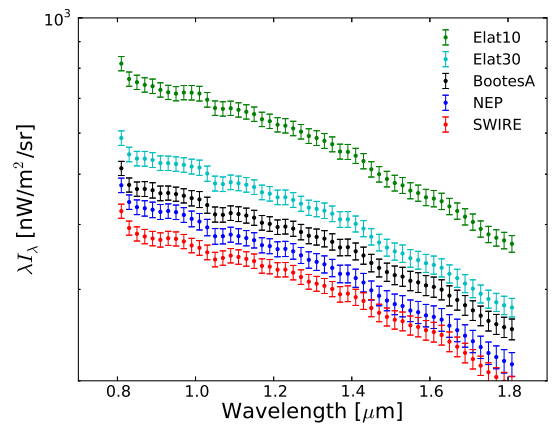


Figure 4.9: The sky brightness of the second flight. The relation between line color and field is presented in the legend. We remove the atmospheric emission and out-gas emission from 4.8. The error bars are mainly due to flux calibration error.

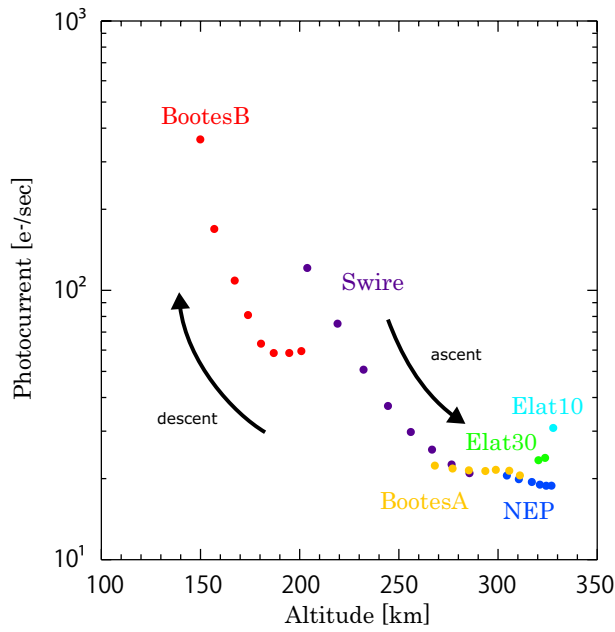


Figure 4.10: Altitude dependence of the observed brightness. The x-axis indicate the altitude of the locket from the ground. The y-axis present the observed brightness. The color of plots presents field as shown in the legend.

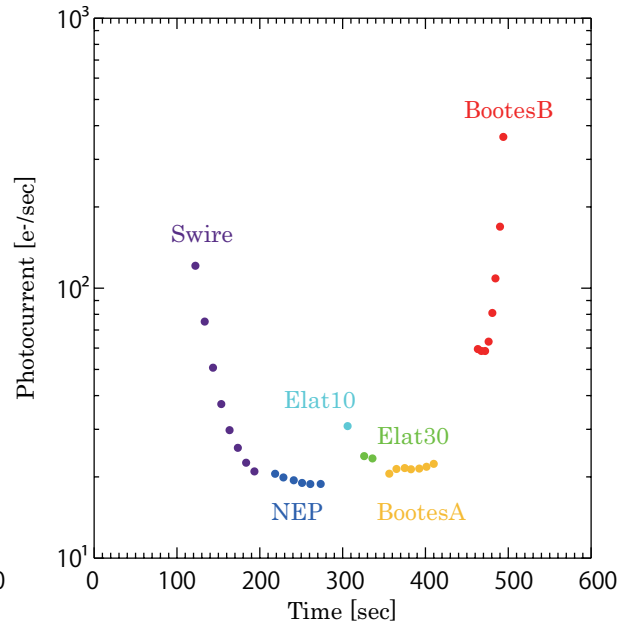


Figure 4.11: Time dependence of the observed brightness. The x-axis indicate the time from launch. The y-axis present the observed brightness. The color of plots presents field as shown in the legend.

### 4.3.3 Astronomical Sky Brightness

The sky brightness consists of only astronomical emission:

$$I_{sky} = I_{ZL} + I_{ISL} + I_{DGL} + I_{EBL} \quad (4.2)$$

To obtain astronomical information from this total sky brightness, we need to decompose it into the emission components.

Separating the  $I_{ISL}$  is easier than separating other components, because there are an observations and a models of deep star counts. To estimate  $I_{ISL}$ , we carry out the Monte-Carlo simulation of star distribution and integrate the fluxes of the faint stars fallen in the FOV. As the input star data for the simulation, we use 2MASS catalog in J-band for the Vega magnitude of  $\leq 17$ th, and contemporary model of star counts named TRILEGAL galaxy model (Girardi et al. 2005) for  $17\text{mag} < \text{J-band Vega magnitude} < 32\text{mag}$ . The detail of the Monte-Carlo simulation is written in Appendix B. We show the result of the ISL calculation in Figure 4.12, for example at the NEP of second flight. The error bars of the ISL present only statistical uncertainty estimated from the Monte-Carlo simulation.

We define the residual sky brightness as

$$I_{res} = I_{ZL} + I_{DGL} + I_{EBL} \quad (4.3)$$

From the next section, we will separate the  $I_{ZL}$  and  $I_{DGL}$  from  $I_{res}$ .

## 4.4 Separation of Zodiacal Light and Diffuse Galactic Light by Differential of Two Field

The simplest way to obtain spectral shape of  $I_{ZL}$  from  $I_{res}$  is to calculate the difference between two fields which have same the  $I_{DGL}$ .  $I_{EBL}$  is assumed to be isotropic. In other words, we can derive

$$I_{ZL,i} - I_{ZL,j} = I_{res,i} - I_{res,j} \quad \text{for} \quad I_{DGL,i} = I_{DGL,j} \quad (4.4)$$

where subscripts  $i$  and  $j$  indicate the fields and must be  $I_{res,i} > I_{res,j}$ . In the same way, we can derive spectrum shape of  $I_{DGL}$  by calculating the difference

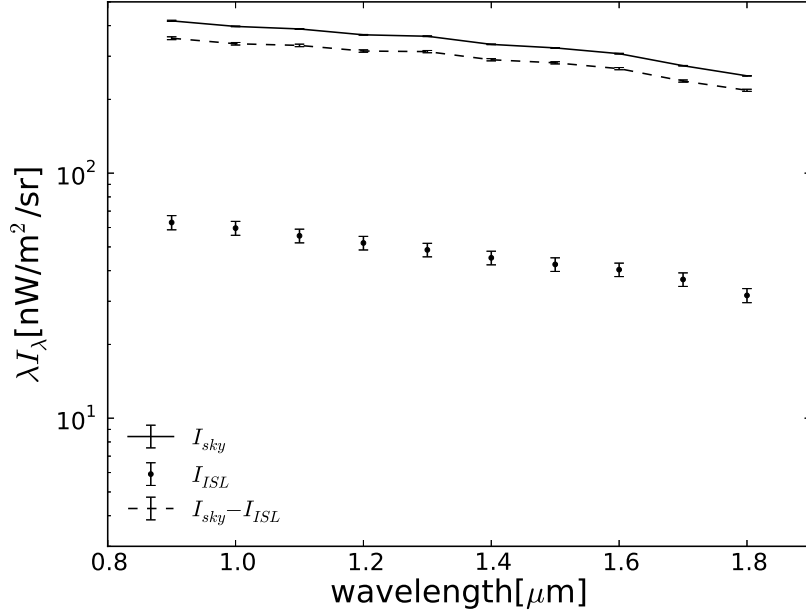


Figure 4.12:  $I_{sky}$ ,  $I_{ISL}$  and  $I_{sky} - I_{ISL}$  of NEP field. The  $I_{ISL}$  is estimated in Appendix B. The error bars of  $I_{sky}$  indicates only statistical uncertainty estimated from the variance of all pixels in the detector. The error bars of  $I_{ISL}$  also present statistical uncertainty estimated from Monte-Carlo simulation.

Table 4.1: The  $100\mu\text{m}$  brightness interstellar dust in second flight (Schlegel et al. 1998). The ZL brightness is calculated from Kelsall et al. (1998) at  $1.25\mu\text{m}$ .

Field name	SWIRE	NEP	Elat10	Elat30	BootesA
$100\mu\text{m}$ brightness [ $\text{MJy}^{-1}$ ]	$0.5\pm 0.1$	$2.5\pm 0.6$	$4.1\pm 1$	$1.6\pm 0.4$	$0.6\pm 0.2$
ZL brightness [ $\text{nWm}^{-2}\text{sr}^{-1}$ ]	$244\pm 12$	$235\pm 12$	$487\pm 24$	$363\pm 18$	$319\pm 16$

between the two fields which have the same  $I_{ZL}$ :

$$I_{DGL,i} - I_{DGL,j} = I_{res,i} - I_{res,j} \quad \text{for} \quad I_{ZL,i} = I_{ZL,j} \quad (4.5)$$

However we do not know  $I_{ZL}$  and  $I_{DGL}$ , and we therefore calculate the above equation on the assumption that the spatial distribution of ZL is the same as the ZL model in Kelsall et al. (1998), and that the spatial distribution of DGL is the same as the  $100\mu\text{m}$  brightness (Schlegel et al. 1998).

The ZL model is the most conventional and it reproduces the all-sky data by DIRBE/COBE with a few percent level. For the second assumption, the  $100\mu\text{m}$  brightness traces thermal emission from interstellar dust, and it can be written as

$$I_{100\mu\text{m}} \propto \sigma N_{ISD} B(100\mu\text{m}) \quad (4.6)$$

where  $N_{ISD}$  indicates the column number density of interstellar dust which emits thermal emission, and  $B$  is plank function corresponding to the temperature of the dust.  $\sigma$  is the emissivity of the dust. On the other hand, the scattered light by interstellar dust is presented as

$$I_{DGL} \propto \kappa N'_{ISD} I_{star} \quad (4.7)$$

where the  $\kappa$  indicates scattering coefficient,  $N'_{ISD}$  indicates number density of interstellar dust which contributes to the scattering, and  $I_{star}$  is the interstellar radiation field (ISRF). In optically thin limit, number density of the interstellar dust should be  $N_{ISD} = N'_{ISD}$ . Therefore, from these two equations,

$$I_{DGL} \propto \frac{\kappa I_{star}}{\sigma B} I(100\mu\text{m}) \quad (4.8)$$

Thus there is a simple linear relation between the spatial distribution of the  $100\mu\text{m}$  brightness and that of the DGL brightness.

Table 5.1 summarizes the predicted  $I_{DGL}$  and  $I_{ZL}$  at the observed fields. According to this, we have the required condition of  $I_{DGL,SWIRE} \approx I_{DGL,BootesA}$  and  $I_{ZL,SWIRE} \approx I_{ZL,NEP}$ . We calculate Equations 4.4 and 4.5 for these fields and presented them in Figure 4.13 with solid line and Figure 4.14 with small circles, respectively.

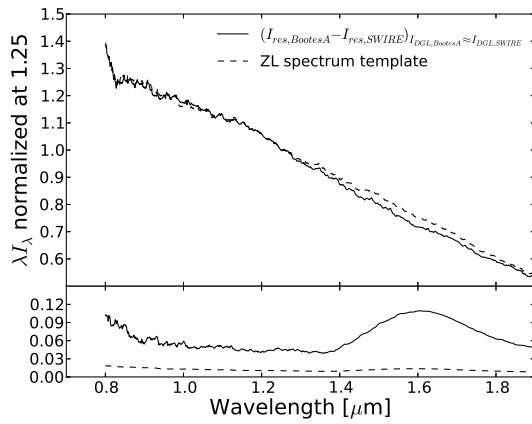


Figure 4.13: ZL spectrum normalized at  $1.25\mu\text{m}$ . The solid line indicates difference of  $I_{res,BootesA} - I_{res,SWIRE}$ . The dashed line indicates the ZL spectrum derived from the global-method. The bottom panel shows the error of the spectrum.

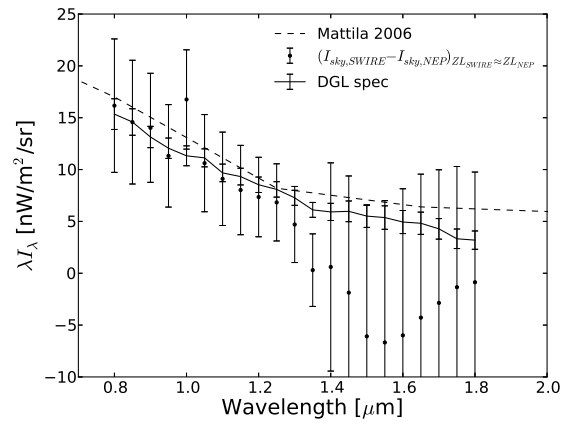


Figure 4.14: DGL spectrum normalized. The small circles indicate  $I_{res,NEP} - I_{res,SWIRE}$ . The dashed line present the DGL estimated by Mattila (2006). The solid line indicates the DGL spectrum derived from the global method at  $I(100\mu\text{m}) = 1\text{MJysr}^{-1}$ .

Next, we estimate the ZL brightness and the DGL brightness at  $1.25\mu$ . We assume that the our observed ZL brightness has the same spatial distribution as the ZL model (Kelsall et al. 1998). In other words, the ZL brightness can be represented as follows in this assumption.

$$I_{ZL}(1.25\mu\text{m}) = a(1.25\mu\text{m})I_{ZLmodel}(1.25\mu\text{m}) \quad (4.9)$$

where  $I_{ZLmodel}$  is the ZL brightness of the model, subscript  $i$  and  $j$  indicate the field. Thus we can easily calculate the ZL brightness from the difference between two fields as follows.

$$\begin{aligned} a &= \frac{I_{ZL,i}(1.25\mu\text{m}) - I_{ZL,j}(1.25\mu\text{m})}{I_{ZLmodel,i}(1.25\mu\text{m}) - I_{ZLmodel,j}(1.25\mu\text{m})} \\ &= \frac{I_{res,i}(1.25\mu\text{m}) - I_{res,j}(1.25\mu\text{m})}{I_{ZLmodel,i}(1.25\mu\text{m}) - I_{ZLmodel,j}(1.25\mu\text{m})} \end{aligned} \quad (4.10)$$

$$\text{for } I_{DGL,i} = I_{DGL,j}$$

In the same way, we can calculate the DGL brightness by assuming optical thin limit as follows.

$$I_{DGL}(\lambda) = bI_{100\mu\text{m}} \quad (4.11)$$

We already have the required condition of  $I_{DGL,SWIRE} \approx I_{DGL,BootesA}$  and  $I_{ZL,SWIRE} \approx I_{ZL,NEP}$ . Thus we obtain  $a = 1.05 \pm 0.2$  and  $b = 0.133 \pm 0.05$  at  $1.25\mu\text{m}$ .

We successfully derive not only the spectrum shape but also the brightness of ZL and DGL by the differencing of the two field. However, the derived spectra has large error bars as shown in Figure 4.13 and 4.14. The determination error for  $a$  and  $b$  are too large to obtain any scientific result including the measurement of EBL. In the next section, we find self consistent solution of  $I_{ZL}$  and  $I_{DGL}$  iteratively using the data of all field.

## 4.5 Separation of Zodiacal Light and Diffuse Galactic Light by Global-Structure Method

To obtain high S/N solution of  $I_{ZL}$  and  $I_{DGL}$ , we iteratively find the self consistent solution using the data of all the observation field. We term this iterative

analysis as 'global-structure' method, because we use the global structure of dust distribution to correlate the sky brightness with the ZL model and the  $100\mu\text{m}$  brightness.

In the first step of this iteration, we use the result of  $I_{res}$  derived by the differencing of the two field, and subtract it from  $I_{ZL}$ . Then we correlate  $I_{res} - I_{ZL}$  with the  $100\mu\text{m}$  brightness. In this correlation, we assume that the spectra shape of the ZL does not depend on the ecliptic coordinate. We verify the validity of this assumption in section 5.1. Figure 4.15 shows the correlation between  $I_{res} - I_{ZL}$  and the  $100\mu\text{m}$  brightness. The slope of best-fit linear function presents  $b(\lambda)$ . Minimum  $\chi^2$  analysis is applied to fit a linear function to this correlation.

In the second step of this iteration, we use  $b(\lambda)$  derived in the first iteration and the  $100\mu\text{m}$  brightness to derive  $I_{DGL}$ , and subtract it from  $I_{res}$ . Figure 4.15 shows the correlation between  $I_{res} - I_{DGL}$  and the ZL model. We also obtain  $a(\lambda)$  from the slope of the best-fit linear function. In the third step of this iteration, we feed back the  $a(\lambda)$  to reprocess the DGL correlation analysis, and such iterations are processed.

This iteration converges at three times. We find that  $b(\lambda) = 0.27 \pm 0.03$  for DGL, and  $a(\lambda) = 1.00 \pm 0.01$  for ZL. These uncertainties are estimated from  $\sigma_{slope}$  as follows.

$$\sigma_{slope} = \frac{1}{\Delta} \sum \frac{x_i^2}{\sigma_i^2} \quad (4.12)$$

$$\sigma_{intercept} = \frac{1}{\Delta} \sum \frac{1}{\sigma_i^2} \quad (4.13)$$

$$\Delta = \sum \frac{1}{\sigma_i^2} \sum \frac{x_i^2}{\sigma_i^2} - \left( \frac{\sum x_i^2}{\sum \sigma_i^2} \right)^2 \quad (4.14)$$

This result indicates that the ZL brightness derived by the global-structure method is consistent with the ZL model with 1% accuracy.

The dashed line of Figure 4.13 shows the ZL spectrum derived by this iterative method. The ZL spectrum of the global-structure method is consistent with the ZL spectrum of the differential method with in the error bars. The solid line of Figure 4.14 shows the DGL spectrum derived by the global-structure method. The DGL spectrum of the global-structure method is also well consistent with the DGL spectrum of the differential method.

We successfully obtain high S/N solution of  $I_{ZL}$  and  $I_{DGL}$  by the global-structure method. In the next section, we derive the DGL spectrum by different method. We correlate the sky brightness with the  $100\mu\text{m}$  brightness in individual field.

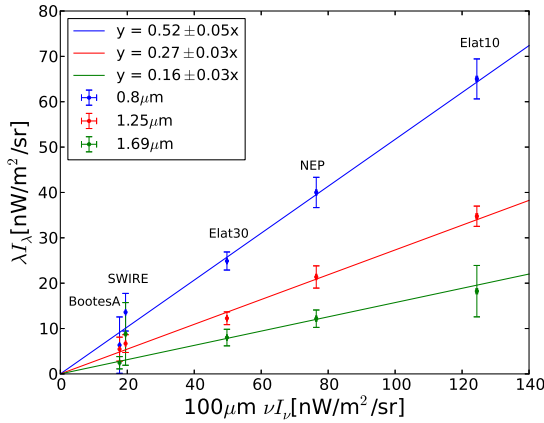


Figure 4.15: Correlation between  $I_{res} - I_{ZL}$  which we observed (y-axis) and  $100\mu\text{m}$  brightness of interstellar dust (x-axis). The lines indicate the best fit line of each wavelength. The slopes provide the DGL to  $100\mu\text{m}$  brightness ratio  $b(\lambda)$ . The intercept provide EBL, but we do not show the intercept in this plot. The error bars consist of statistical error and the uncertainty of subtraction of airglow, and the ZL and ISL.

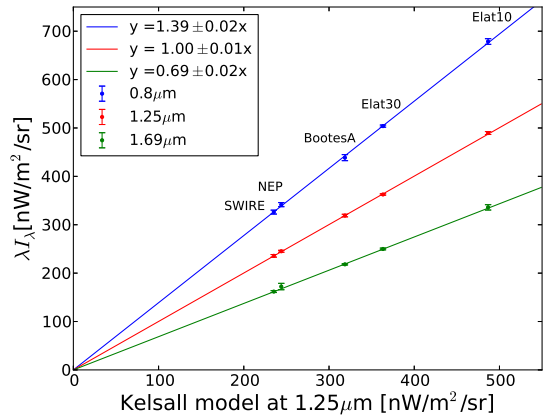


Figure 4.16: Correlation between  $I_{res} - I_{DGL}$  which is our result (y-axis) and ZL brightness derived from Kelsall et al. (1998). The lines indicate the best fit line of each wavelength. The slopes  $a(\lambda)$  provide the spectrum shape of ZL. The intercept provides EBL, but we do not show the intercept in this plot. The error bars consist of statistical error and the uncertainty of subtraction of the atmospheric emission, out-gas emission, the ISL and DGL.

## 4.6 Separation of Diffuse Galactic Light by Local-Structure Method

By the global-structure method, we derive the DGL spectrum using the data of all the observation field. In other words, we correlate the sky brightness with the  $100\mu\text{m}$  brightness based on global structure of column density of interstellar dust. It is known that the  $100\mu\text{m}$  brightness has not only global structure but also local structure on spatial scales smaller than a degree (see 3.2). On the other hand, the ZL brightness is known to be spatially uniform on spatial scales smaller than a degree (Abraham et al. 1997; Kashlinsky et al. 2005). Thus we can separate DGL from the sky brightness based on this local structure, hereafter the local-structure method.

To separate  $I_{DGL}$  using such a local structure, we correlate  $I_{obs}$  with the  $100\mu\text{m}$  brightness in an individual field. We remove brighter the stars ( $<13\text{th}$  AB magnitude) than the detection limit of LRS by two sigma clipping as discussed in previous section. We assume that the faint stars are distributed randomly in FOV. In addition, because the airglow emission do not have such a small structure. Thus we assume that these emissions do not affect this correlation analysis. The ZL brightness has only large smooth structure, but it makes some gradient of brightness in FOV. We therefore remove  $I_{ZL}$  from  $I_{obs}$  using the result of the global-structure method.

Figure 4.17 shows the correlation between  $I_{obs} - I_{ZL}$  and the  $100\mu\text{m}$  brightness of the Elat10 of the second flight. These four panels of Figure 4.17 present different wavelength. The solid line indicates best-fit linear function. To decrease a read out noise and the flat-field error, we divide the LRS resolution of  $1.4'$  into  $90'$ . We also average the wavelength bins to resolution of  $\Delta\lambda = 200\text{nm}$ . The error bars are dominated by the flat-field error. One can see clear correlation, even if the large error bar.

Figure 4.18 also shows the correlation between  $I_{obs} - I_{ZL}$  and the  $100\mu\text{m}$  brightness of all the four field where we can see the correlation. These four panel of Figure 4.18 present same wavelength of  $1.0\mu\text{m}$ . The error bars are dominated by the flat-field error. The solid line indicates best-fit linear function. We can see

correlation in all four field.

Figure 4.19 shows the correlation between  $I_{obs} - I_{ZL}$  and the  $100\mu\text{m}$  brightness of the BootesA of the second flight. These four panels of Figure 4.17 present different wavelength. The solid line indicates best-fit linear function. We can not see correlation in the BootesA. The  $100\mu\text{m}$  brightness of the BootesA is too faint to indicate significant correlation with the DGL brightness. We present it for a null test.

To separate DGL from the sky brightness, we fit a linear function to the data to find obtain the slope. The slope of this linear function present a conversion factor  $b(\lambda)$  from the  $100\mu\text{m}$  brightness to the DGL brightness. Figure 4.20 shows this conversion factor  $b(\lambda)$  derived from the NEP of the second flight and the third flight, and the Elat10 of the second flight, and the DGL field of the fourth flight. The error bars are estimated from Equation 4.12. Although the error bars are large, the conversation factors of every field are consistent with each other within error bar.

Figure 4.19 shows mean of  $b(\lambda)$  of all the four fields derived in here together with the result of the global-structure method derive above. The y-axis indicates  $b(\lambda)$ . The x-axis indicates wavelength. These results are consistent with each other within the error bars. This result indicates that there is not the systematic error due to the separation method.

## 4.7 ZL polarization

We measure the ZL polarization from the data taken in the third flight. In addition, the wavelength dependence of polarization of ZL has never been observed.

In the observation, we measure the ZL polarization with the four polarizer installed in LRS. The relative angles of these four polarizers are  $\phi = 0^\circ, 90^\circ, 45^\circ$  and  $-45^\circ$ , we call the measured sky brightness at these four angle as  $I(0^\circ)$ ,  $I(90^\circ)$ ,  $I(45^\circ)$  and  $I(-45^\circ)$

Figure 4.22 shows the measured  $I(\phi)$  as a function of  $\phi$  at the NEP field. The y-axis indicates the measured sky brightness  $I(\phi)$ . The red circles present the measured data. The error bars are dominated by the flat-field error. The black

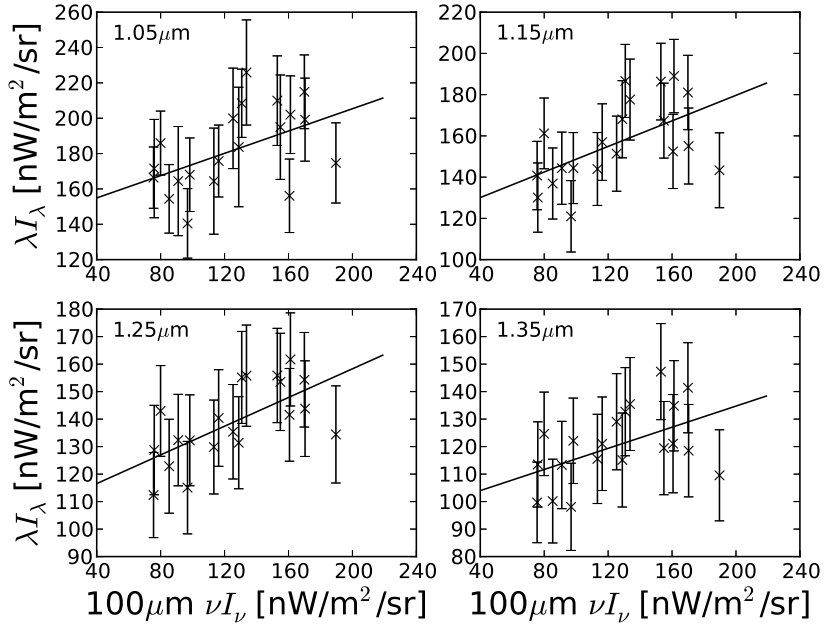


Figure 4.17: Correlation between  $I_{obs} - I_{ZL}$  (y-axis) and the  $100\mu\text{m}$  brightness of interstellar dust (x-axis) in Elat10 of the second flight. We show the correlation of four different wavelength in each panel. The lines present the best fit linear function. The error bars consist of variance of pixels, flat field error, and uncertainty of subtraction of the ZL.

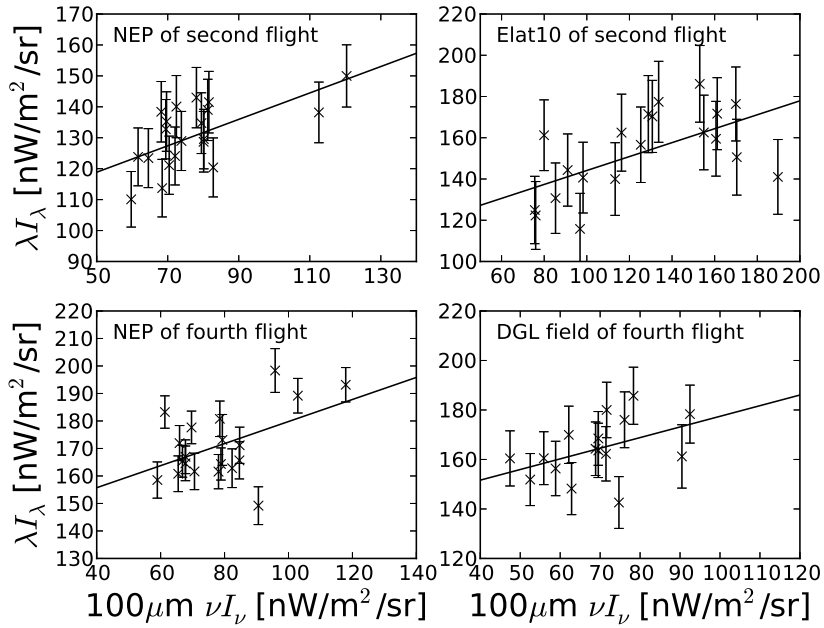


Figure 4.18: Correlation between  $I_{obs} - I_{ZL}$  (y-axis) and the  $100\mu\text{m}$  brightness of interstellar dust (x-axis) in an individual field. Top left is the correlation of the NEP field for the second flight. Top right is Elat10 for the second flight. Bottom left is NEP for the fourth flight. Bottom right is DGL field for the fourth flight. X marks indicate data point. The lines present the best fit linear function. The error bars consist of variance of pixels, flat field error, and uncertainty of subtraction of ZL.

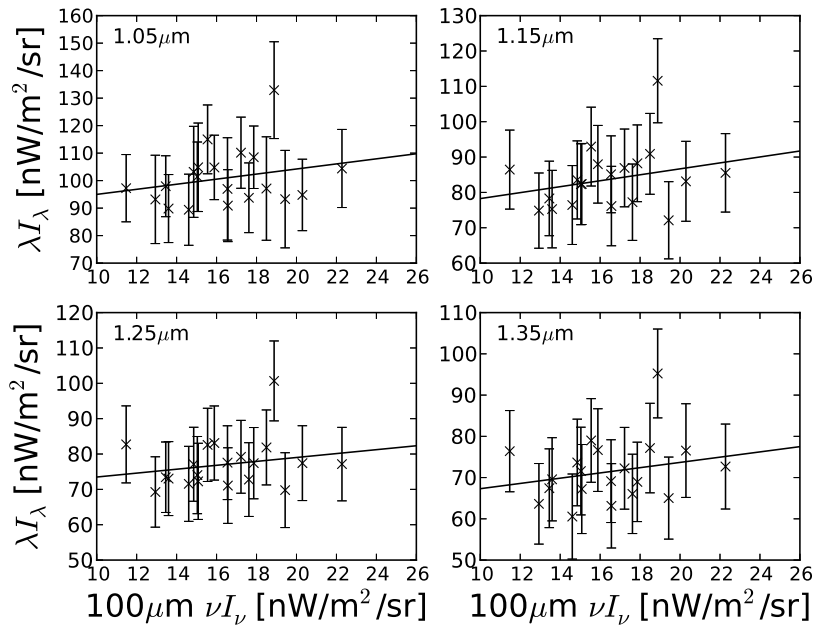


Figure 4.19: Correlation between  $I_{obs} - I_{ZL}$  (y-axis) and the  $100\mu\text{m}$  brightness of interstellar dust (x-axis) in BootesA of the second flight. We see no correlation.

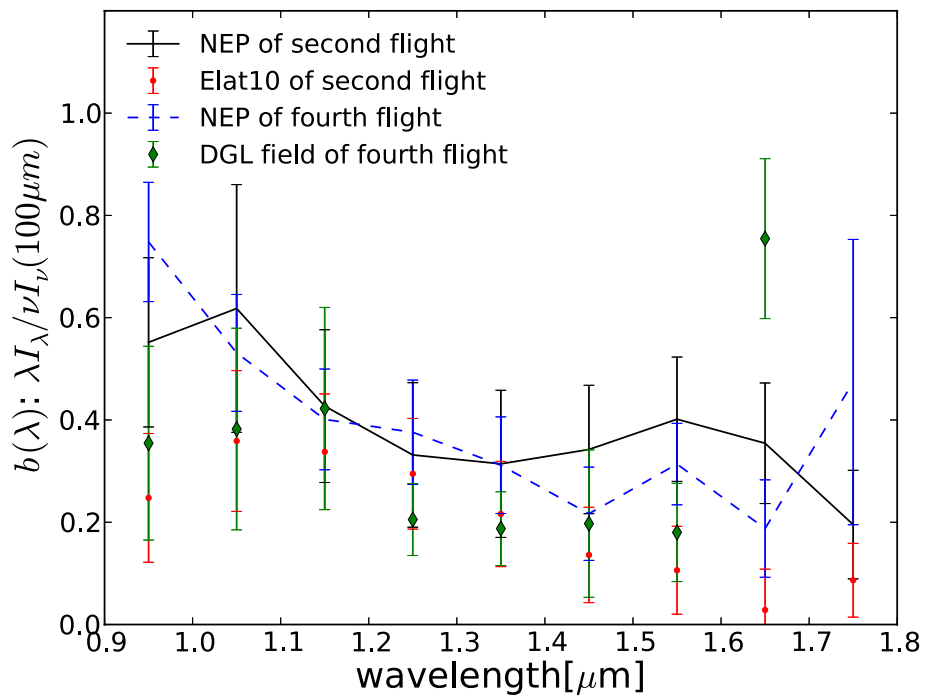


Figure 4.20: The slope  $b(\lambda)$  as a function of wavelength in all four fields. The black solid line, blue dashed line, green squares, red dots indicate the NEP of the second flight, the NEP of the third flight, the DGL-field of the fourth flight, and the Elat10 second flight respectively.

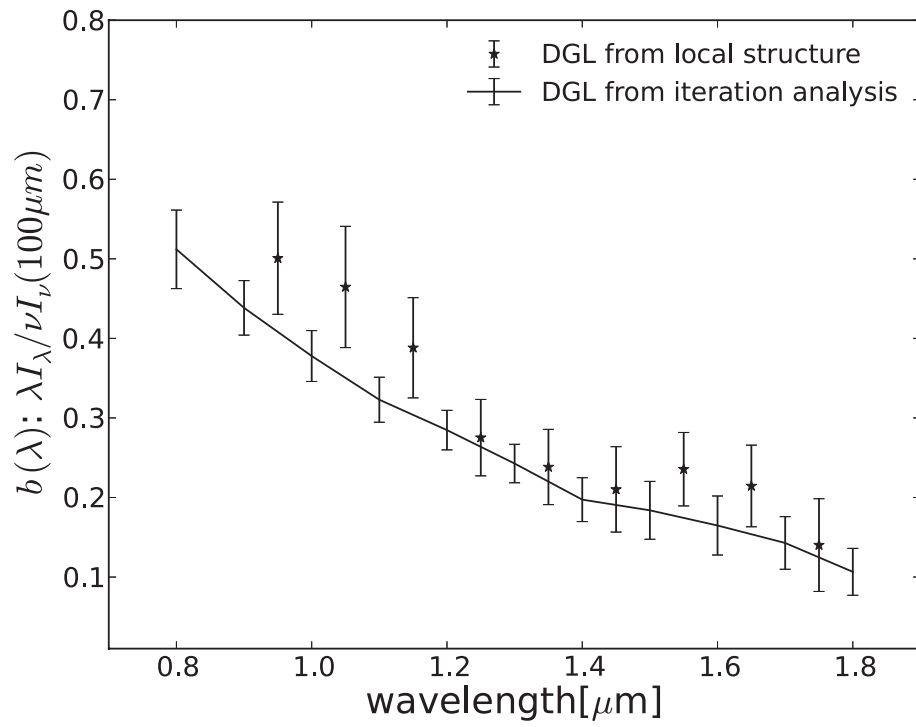


Figure 4.21: The slope  $b(\lambda)$  derived from global distribution and local distribution of interstellar dust. The solid line indicates  $b(\lambda)$  derived from global distribution (iterative analysis). The asterisk indicates mean  $b(\lambda)$  of four fields, derived from local distribution.

line indicates the best-fit result of following the equation,

$$I(\theta, \nu) = a(\nu) \sin(2\pi(\phi - \phi_0(\nu))/180) + b(\nu) \quad (4.15)$$

where  $\phi_0$  presents the phase angle of the ZL polarization,  $a$  indicates the brightness of the polarized component,  $I_{pol} = a$ , and  $b$  indicates the unpolarized component of the sky brightness:  $I_{sky} = b$ . We use Levenberg-Marquardt algorithm to find best-fit parameters. As an example, we find  $b = 441 \pm 7 \text{ nWm}^{-2} \text{ sr}^{-1}$ ,  $a = 60 \pm 10 \text{ nWm}^{-2} \text{ sr}^{-1}$ , and  $\phi_0 = 29 \pm 3^\circ$  for the solid line of Figure 4.22. We can calculate the degree of polarization of the sky brightness as  $P_{sky} = I_{pol}/I_{sky} = 13.6 \pm 0.2\%$ .

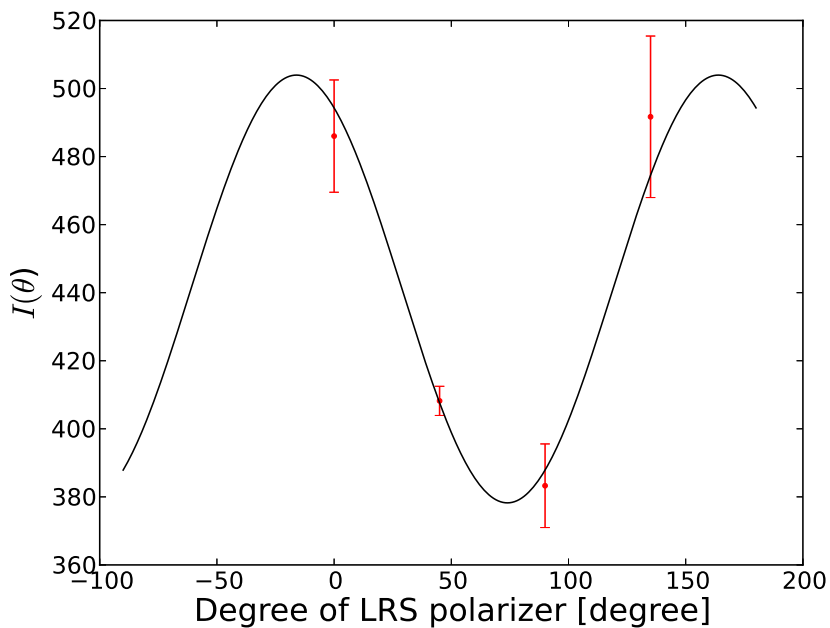


Figure 4.22: The red circles indicate the sky brightness through the four polarizer:  $I(0^\circ)$ ,  $I(90^\circ)$ ,  $I(45^\circ)$  and  $I(-45^\circ)$  at  $1.0\mu\text{m}$ . The black line presents result of best fit Equation 4.15.

The polarization component  $I_{pol}$  is dominated by the ZL polarization. The polarization of other diffuse radiation is negligible. The polarization of star light

by interstellar dust is known to be less than 1% at high galactic latitude  $> 30^\circ$  (Heiles 2000). The EBL would not be polarized, because the EBL arises from randomly oriented extragalactic sources. Thus we can assume that  $I_{pol}$  is due to the polarization of ZL.

Figure 4.23 shows both  $I_{pol}/I_{sky}$  and  $I_{pol}/I_{ZL}$  as a function of wavelength at the NEP field. The error bars are estimated from the fitting errors of the parameters  $b$  and  $a$ . We also add the calibration error of polarization of 1%. We use  $I_{ZL}$  derived by the iterative method. The result show that the contribution of  $I_{ISL}$ ,  $I_{DGL}$  and  $I_{EBL}$  to the sky brightness makes  $\sim 10\%$  lowering of the polarization at NEP. If we do not remove these contributions, we underestimate the polarization of ZL. Both  $I_{pol}/I_{sky}$  and  $I_{pol}/I_{ZL}$  show little wavelength dependence in the whole wavelength range.

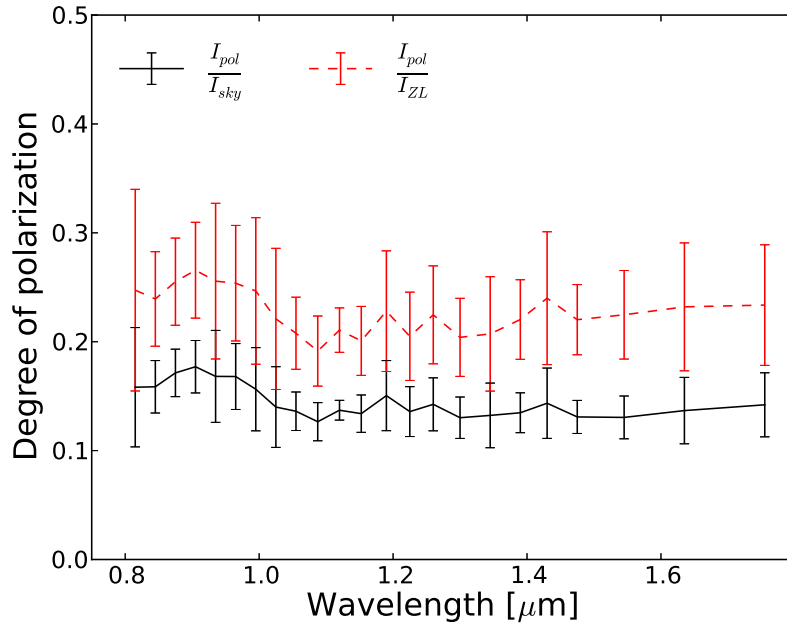


Figure 4.23: The degree of polarization as a function of wavelength. We show both  $\frac{I_{pol}}{I_{sky}}$  with black solid line and  $\frac{I_{pol}}{I_{ZL}}$  with red dashed lines.

When we fit Equation 4.15 to the data, we set  $\phi_0$  as a free parameter, because

Table 4.2: Expected phase angle  $\phi_{0,exp}$  and measured phase angle  $\phi_{0,meas}$ . The unit is degree.

	Lockman	SWIRE	NEP	Elat30	BootesB
Expected phase angle	$23\pm 1$	$-23\pm 3$	$30\pm 2$	$-41\pm 2$	$-80\pm 2$
Measured phase angle	$29\pm 4$	$-26\pm 2$	$29\pm 2$	$-42\pm 8$	$-102\pm 17$

the rotational angle of LRS is not determined yet. The angle determination by the identification of the detected stars is under process.

On the other hand, we can predict the phase angle of the ZL polarization from geometry of the dust scattering of sunlight and the line of sight of the observation as depicted in Figure 4.24 and 4.25. The ZL should be polarized to the direction perpendicular to the plane of incidence.

Thus we need to calculate only angle of plane of incidence  $\gamma$  and rotational angle  $A$ , because the phase angle can be calculated as;  $\phi_0 = A + \gamma - 45^\circ$ . We summarize the result of phase angle in Table 4.2. The measured phase angle is consistent with the expected phase angle from the data of the altitude control system.

This result is first measurements of the spectrum of ZL polarization.

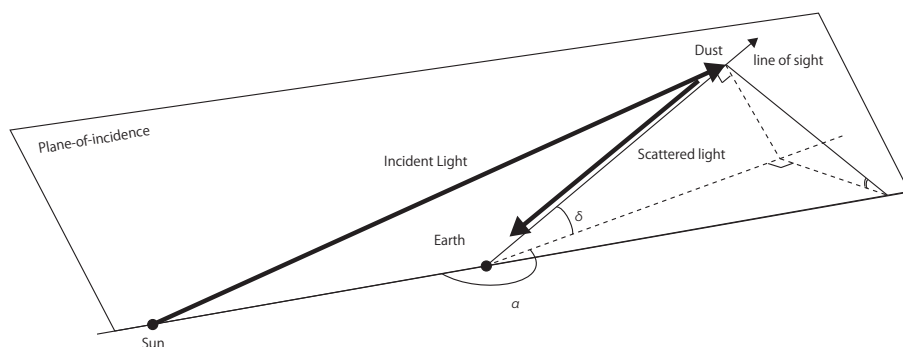


Figure 4.24: The picture of geometry of the ZL observation, viewed from outside of the solar system.

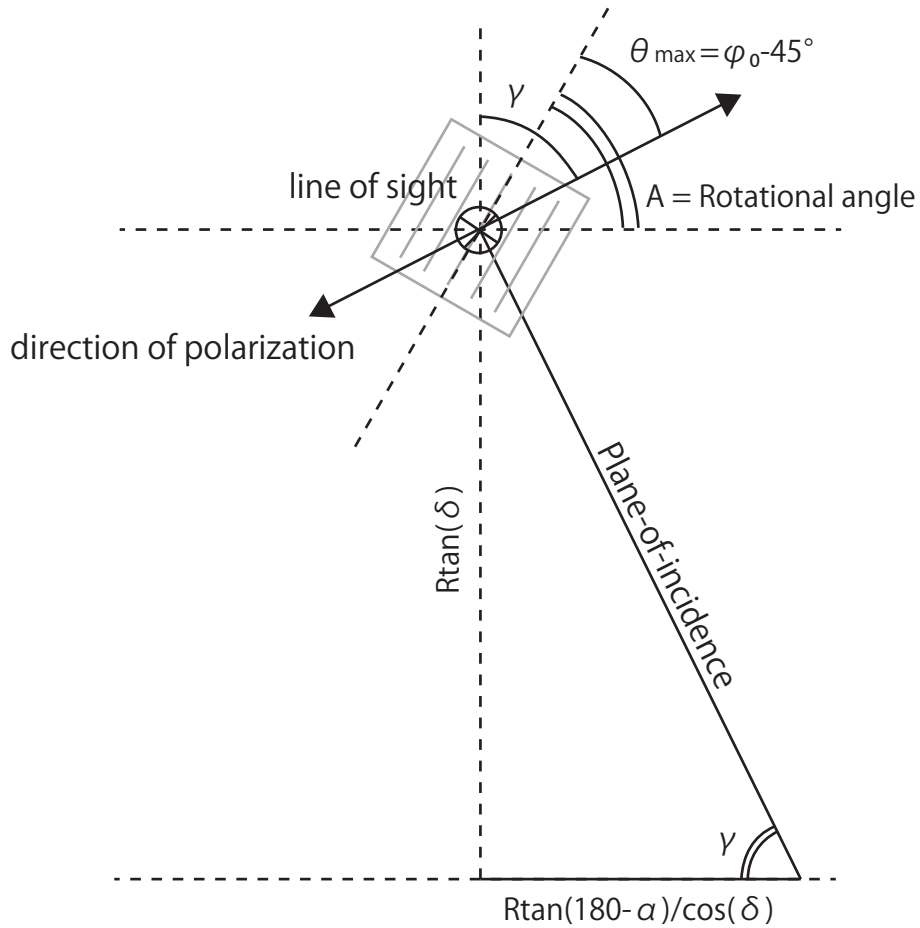


Figure 4.25: Orientation of the FOV of LRS respect to the direction of the ZL polarization, viewed from LRS toward the line of sight.

## 4.8 Summary of the Data Reduction and Analysis

In this chapter, we introduce the data reduction and analysis. The summary of this chapter is as follows.

- We described the data reduction from the raw data to the sky spectra and the astronomical analysis to decompose the sky spectra in to ZL and DGL in details.
- We obtained the sky spectra at observation fields with accuracy of 1% limited by the dark-current subtraction error and the airglow subtraction error.
- The ZL and DGL spectra are decomposed from the sky spectra by using their correlation relations with the modeled ZL distribution and the  $100\mu\text{m}$  dust emission map.
- We first detected the ZL polarization and its wavelength dependence.



# Chapter 5

## Result and Discussion

In this chapter, we present our results of the Zodiacal Light (ZL) spectrum, the ZL polarization, and the Diffuse Galactic Light (DGL) spectrum estimated from the observed sky brightness in Chapter 4. We derive size distribution and composition of interplanetary dust, which is responsible for ZL, and interstellar dust, which is the source of DGL, based on observed data.

### 5.1 Zodiacal Light

#### 5.1.1 Spectrum of Zodiacal Light

We estimate the ZL spectrum in Chapter 4. When we correlate the sky brightness with the DIRBE/COBE map to separate ZL from sky brightness, we assume that the spectrum shape of ZL,  $Z(\nu)$ , does not depend on ecliptic coordinates. Firstly in this subsection, we check the validity of this assumption. Secondly, we compare our observed ZL spectrum with other observations.

Figure 5.1 shows the difference of the ZL spectrum between a pair of the two fields.  $I_{ZL,Elat10} - I_{ZL,BootesA}$  indicates difference of the ZL spectrum between the Elat10 and the BootesA of the second flight. In the same way,  $I_{ZL,Elat30} - I_{ZL,NEP}$  and  $I_{ZL,BootesA} - I_{ZL,NEP}$  indicate differences between two different fields. The bottom panel of the figure indicates  $1\sigma$  uncertainty of these difference with the same unit of that of the top panel.

All of the three differences are consistent with each other within error. This result indicates that the ZL spectrum shape does not change with ecliptic coordinates. Note that we can not know dependence of ecliptic coordinates. We can only check the ZL spectrum shape does not change in our observed field. Thus, we can verify the assumption of the independent of the ZL spectrum shape from ecliptic latitude in our field.

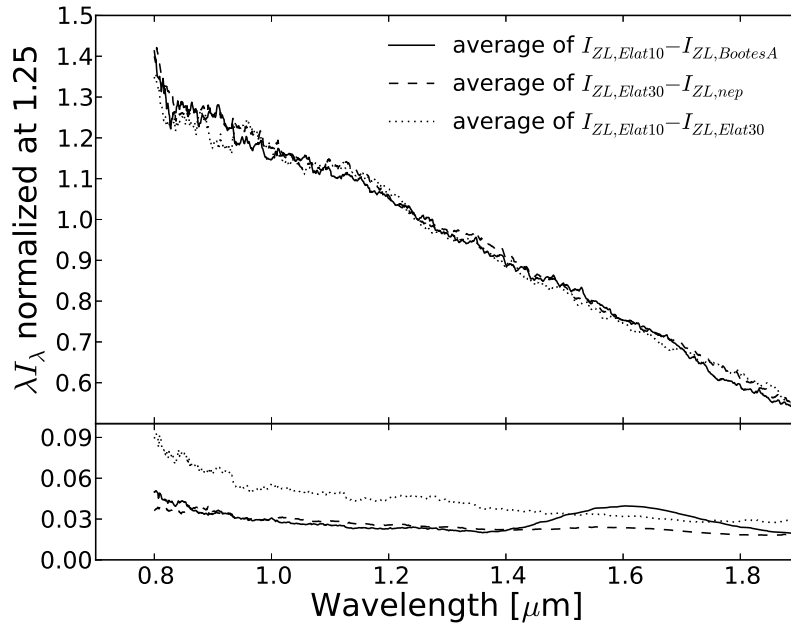


Figure 5.1: Normalized ZL spectrum of the second flight. The solid line indicates average of  $I_{ZL,Elat10} - I_{ZL,BootesA}$ . The dashed line presents average of  $I_{ZL,Elat30} - I_{ZL,NEP}$ . The dot line indicates  $I_{ZL,BootesA} - I_{ZL,NEP}$ . The bottom panel presents  $1\sigma$  uncertainty of the ZL spectrum.

Figure 5.2 shows the ZL spectrum; the ZL brightness at ecliptic coordinate of  $\beta = 0^\circ$  as a function of the wavelength. The error bar of ZL is derived from uncertainty of best-fit parameter of correlation analysis. The systematic uncertainty of the flux calibration, 3%, is not added to the error bar. We find that the ZL spectrum shows redder color than the solar spectrum (black lines)

does from  $0.8\mu\text{m}$  to  $1.5\mu\text{m}$ . On the other hand, our result shows the same color as the solar spectrum does from  $1.5\mu\text{m}$  to  $1.8\mu\text{m}$ .

We compare our result with other observations also in Figure 5.2. Because we do not observe the ecliptic coordinate, we normalize our result to the IRTS data at  $1.8\mu\text{m}$  (Matsumoto et al. 1996). Our result is consistent with long infrared measurements of IRTS data (small circles) and DIRBE/COBE data (Spiesman et al. 1995), and with optical measurement (Frey et al. 1974). Deviation of the ZL spectrum from the solar spectrum at  $>3.0\mu\text{m}$  is caused by thermal emission of interplanetary dust.

From our result we find that the ZL spectrum has neutral or redder color than the solar spectrum does in the near-infrared. The ZL spectrum shape does not change with ecliptic coordinates. Our result is consistent with other observations.

### 5.1.2 Discussion on Spectrum of Zodiacal Light

Size distribution, composition and origin of interplanetary dust are still under debate. In this subsection, we discuss these properties of interplanetary dust based on the observed spectrum color. Firstly, to understand property of interplanetary dust, we compare the color of ZL with color of simple models of Rayleigh scattering, Mie scattering, and Fresnel scattering. Secondly we compare the color of ZL with color of asteroids and comets, because the asteroids and comets are regarded the origin of interplanetary dust.

In the following, we define the reflectivity of ZL with following equation.

$$C_{ZL} = \frac{I_{ZL}(\lambda)/I_{ZL}(\lambda_0)}{F_{solar}(\lambda)/F_{solar}(\lambda_0)} \quad (5.1)$$

#### Rayleigh scattering

As shown in Figure 5.2, the ZL spectrum shape shows redder color than the solar one. If dust radius is smaller than the wavelength,  $2\pi a/\lambda \ll 1$ , particles are responsible for ZL, the scattered spectrum can be approximated by Rayleigh scattering and shows blue color because extinction efficiency by Rayleigh scattering is proportional  $\lambda^{-4}$ . However, the observed ZL spectrum shows neutral or

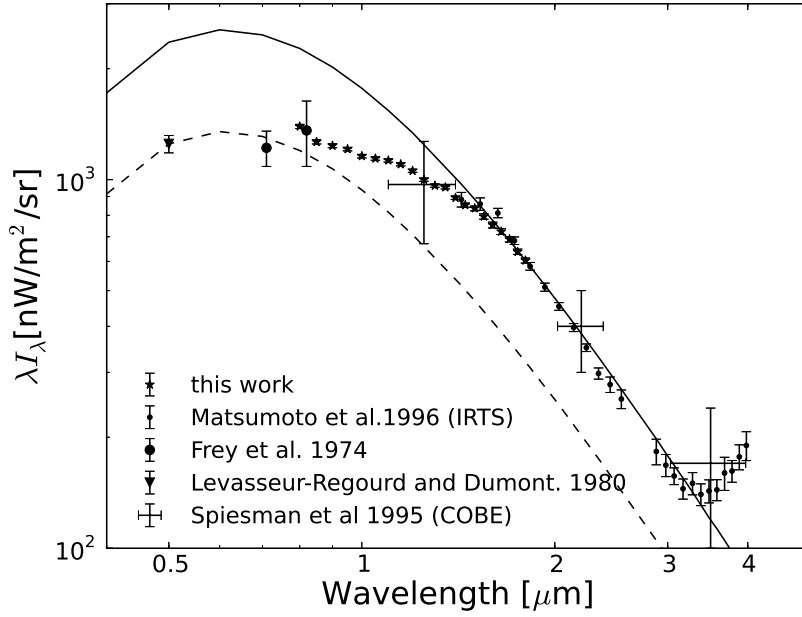


Figure 5.2: The spectrum of the ZL at  $\beta = 0^\circ$  and  $\lambda - \lambda_\odot = 90^\circ$ . Asterisks indicate our result of the ZL spectrum. It is mean of all three spectra in 5.1. Because we does not observe the ecliptic coordinate, we normalize our result to the IRTS data at  $1.8\mu\text{m}$ . The small black circles indicate the result of Matsumoto et al. (1996) with IRTS. The cross present result of Spiesman et al. (1995) with DIRBE/COBE. The large circles indicate optical wavelength measurements from Levasseur-Regourd & Dumont (1980). The triangle is Frey et al. (1974). The solid and dashed lines are solar spectrum with different scaling.

red color. Therefore this ZL spectrum shape cannot be explained by Rayleigh scattering.

### Mie scattering

Next, we consider particles with almost the same size with the wavelength;  $2\pi a/\lambda \approx 1$ . Model of Mie scattering can be used to calculate the spectrum of scattering light by particles with comparable size with the wavelength.

Figure 5.12 shows the reflectivity of ZL and five Mie scattering models as a function of wavelength. These five Mie scattering models are calculated by Berriman et al. (1994). The models assume a uniform composition and particle mass distribution along the line of sight out to 5AU from the earth. The number density of the interplanetary dust is assumed to decline with heliocentric distance from the Sun as  $r^{-1.3}$  (Leinert et al. 1981). Berriman et al. (1994) assumes pure spherical silicate with a power law number distribution by mass of  $dn/d\log m \propto m^{-0.56}$ , as shown in the dot line of the figure. The chain line indicates pure spherical graphite with same size distribution. The solid line indicates a mixture of 50% silicate and 50% graphite with same number distribution. Berriman et al. (1994) also calculated different number distribution model (Grun et al. 1985) with pure spherical silicate, which is presented with the dashed line. Interplanetary dust with the size of  $\sim 30\mu\text{m}$  is predominant in model of Grun et al. (1985). The porous silicate (Bohren & Huffman 1983) is also calculated for particles of radius  $a$  and density  $\rho = \rho_0(a/0.1\mu\text{m})^{2.75-3}$  with the same power law number distribution, presented with black dots and solid line.

None of these Mie models reproduce the reflectivity of ZL. All models show flat reflectivity which is inconsistent with the observed ZL reflectivity. This result indicates that the color of ZL cannot be explained by either Rayleigh scattering or Mie scattering. Thus, we conclude that the cause of the observed red color of ZL is not the particle size effect, but intrinsic reflectance of the dust material determined by its refractive index. And, the dust size is plausibly larger than the wavelength  $2\pi a/\lambda \gg 1$ , as we state in Section 1.2.

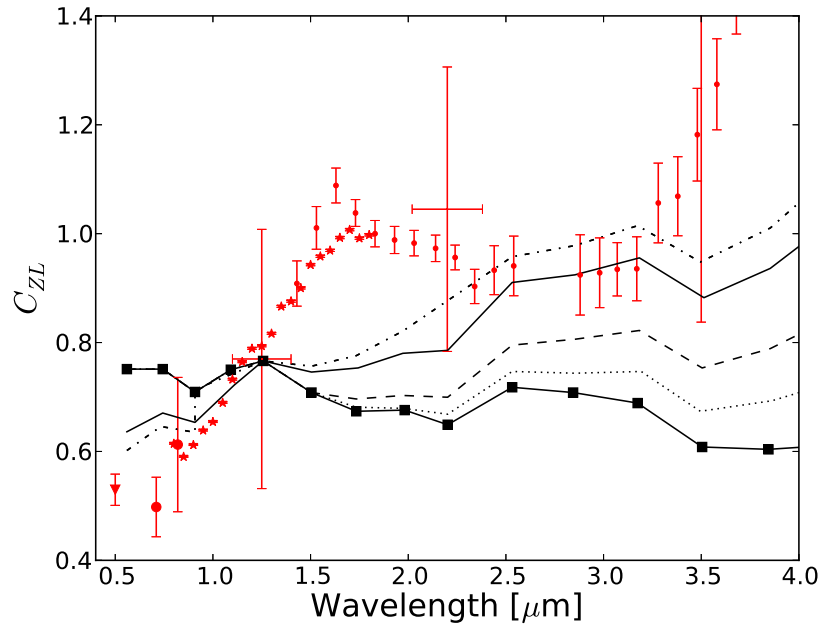


Figure 5.3: Comparison of the reflectivity of ZL with those of Mie scattering models. The plots indicate same as Figure 5.2. The color of ZL is calculated as Equation 5.1. The five Mie scattering are also presented. Dot line: spherical silicate with power low. Dashed line: spherical silicate with dust mass distribution of Grun et al. (1985). Chain line: graphite grains with power low. Solid line: mixture of 50% spherical silicate and 50% spherical graphite. Dots with solid line: Porous silicates with power low.

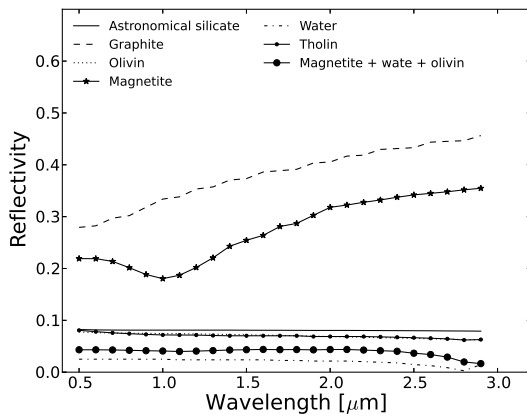


Figure 5.4: Reflectivity of several materials derived from Equation 5.4.

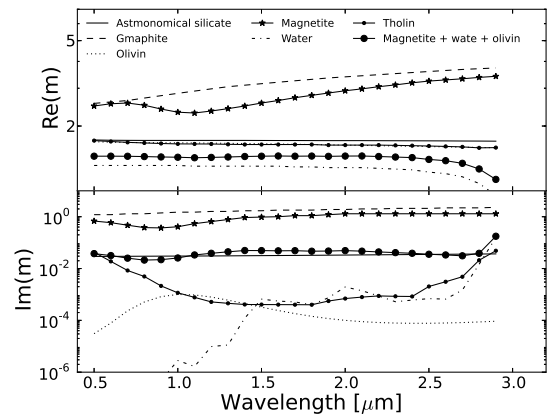


Figure 5.5: Refractive indices used in Figure 5.4. The top panel indicates real part of refractive index. The bottom panel indicates imaginary part of refractive index.

### Fresnel scattering

Since the color of ZL cannot be explained by either Rayleigh scattering or Mie scattering, we consider the Fresnel scattering as approximation of huge particles. Here we consider the Fresnel scattering as approximation of huge particles. The reflected light of Fresnel scattering as follows (Bohren & Huffman 1983).

$$R_{\perp} = \left( \frac{E_{\perp r}}{E_{\perp i}} \right)^2 = \left( \frac{\cos \Theta_i - m \cos \Theta_t}{\cos \Theta_i + m \cos \Theta_t} \right)^2 \quad (5.2)$$

$$R_{\parallel} = \left( \frac{E_{\parallel t}}{E_{\parallel i}} \right)^2 = \left( \frac{\cos \Theta_t - m \cos \Theta_i}{\cos \Theta_t + m \cos \Theta_i} \right)^2 \quad (5.3)$$

The  $E_{\perp}$  and  $E_{\parallel}$  indicate the electric field perpendicular and parallel to the plane of incidence, respectively. The subscripts  $i$ ,  $r$  and  $t$  indicate incident, reflection and transmission, respectively. The  $m = m_1 + im_2$  presents the complex refractive index. One can calculate the reflectivity of the Fresnel scattering as

$$C_{\text{Fresnel}} = \frac{1}{2} (R_{\perp} + R_{\parallel}) \quad (5.4)$$

Figure 5.4 shows reflectivity of the Fresnel scattering derived from Equation 5.4 for several materials. Refractive indices which are used for Figure 5.4 are shown in Figure 5.5. We calculate the reflectivity for a typical materials. None of these materials reproduce the color of ZL. However one can get a implication of the relation between the reflectivity and the refractive index. However one can see that graphite and magnetite show redder color than other materials. Graphite and magnetite have refractive index which is an increasing monotonic function of wavelength. Thus we assume a material which can reproduce the color of ZL. The material has refractive index of  $m = 1.71 + 0.03i$  at  $1.6\mu\text{m}$ , which is same as that of astronomical silicate at the same wavelength. The real part of the refractive index  $Re(m)$  is a monotonic function of wavelength from  $0.8$  to  $1.5\mu\text{m}$ , and a flat from  $1.5$  to  $3.0\mu\text{m}$ . Figure 5.4 shows the reflectivity of ZL with that of Fresnel scattering with this material. The Fresnel scattering with the material could explain the color of ZL. Thus if there is a material which has such a refractive index, we could explain the color of ZL.

We compare the reflectivity of ZL with that of Rayleigh scattering, Mie scattering, and Fresnel scattering. Rayleigh and Mie scattering can not explain the

observed color of ZL. Fresnel scattering with the refractive index can explain the observed color of ZL.

The size of interplanetary dust may be  $a \sim 100\mu\text{m}$  which are expected from dynamical simulation of zodiacal cloud (Nesvorný et al. 2010) and far-infrared measurements (Reach et al. 2003). This is consistent with our result, which requires dust grain much larger than the wavelength.

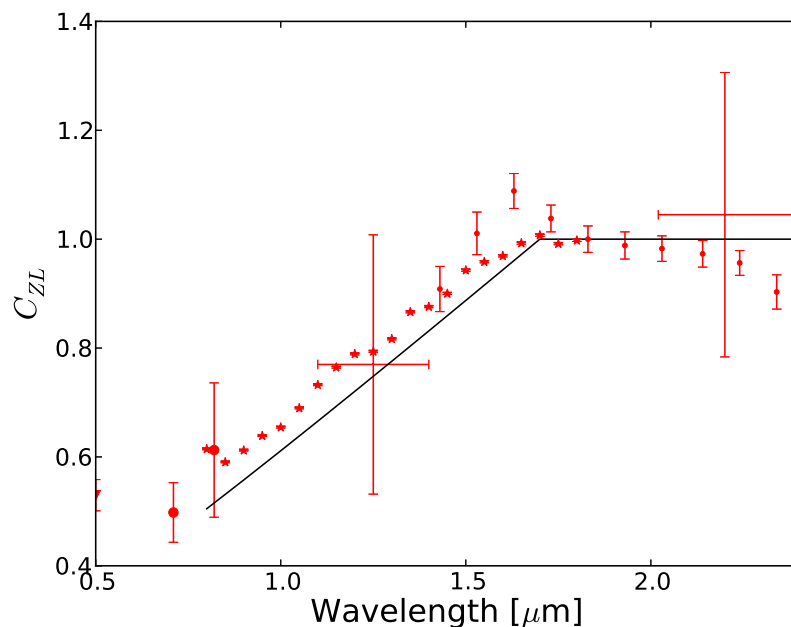


Figure 5.6: Comparison of observational normalized reflectivity of ZL with a material which has a refractive index of  $m = 1.71 + 0.03i$  at  $1.6\mu\text{m}$ . The real part of the refractive index  $Re(m)$  decreases at short wavelength. Red plots indicate observational data, same as Figure 5.2. The black line indicates reflectivity of the material.

### Comparison of the color of Zodiacal Light with those of asteroids and comets

To find the material which reproduce the color of ZL, we compare the color of ZL with those of asteroids and comets.

Figure 5.7 shows the color of ZL with color of several types of asteroids as a function of wavelength. Only the color of S-type asteroid is consistent with the color of ZL from  $1.0\mu\text{m}$  to  $2.0\mu\text{m}$ .

But there is discrepancy between the color of S-type and that of ZL for  $<1.0\mu\text{m}$ . This discrepancy could be explained by the reddening effect of space weathering and/or roughness of surface (Nimura et al. 2008). The space weathering effect on the surface of asteroids explains the difference between color of S-type asteroid and one of ordinary chondrites in optical wavelength.

The space weathering due to vapor coating which includes nanophase-reduced iron ( $\text{npFe}^0$ ) particles changes surfaces reflectivity of regolith particles (Nimura et al. 2008). As an example, some regions on Itokawa has a lower albedo than other regions and shallower  $1\mu\text{m}$  absorption feature (Abe et al. 2006). Abe et al. (2006) also assumes that this difference is caused by the effect of space weathering and/or roughness of surface. Thus, space weathering effects on the surface of S-type asteroids are candidate of origin of the material which reproduces the color of ZL.

We have another possibility. Figure 5.8 shows the color of ZL (red plots) with color of several comets (black lines) as a function of wavelength. The color of comets (Kelley et al. 2004; Cruikshank et al. 1985; Tokunaga et al. 1986) is consistent with the color of ZL. This result indicates that comets are also one possibility for the origin of the material which reproduces the color of ZL. Comets are thought to be supplier of interstellar dust in many studies (Nesvorný et al. 2010). Thus, not only asteroids but also comets are candidate of origin of the material which reproduces the color of ZL.

As discussed above, S-type asteroids (with space weathering effect) and comets can explain the color of ZL. We now know that there is materials which reproduce the color of ZL in our solar system.

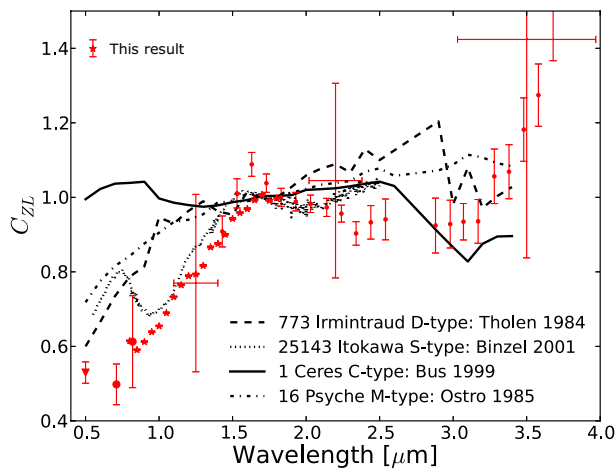


Figure 5.7: Comparison of normalized reflectivity of ZL with that of the asteroids. The colors of D type asteroids, C type asteroids, M type asteroids and S type asteroids are also presented.

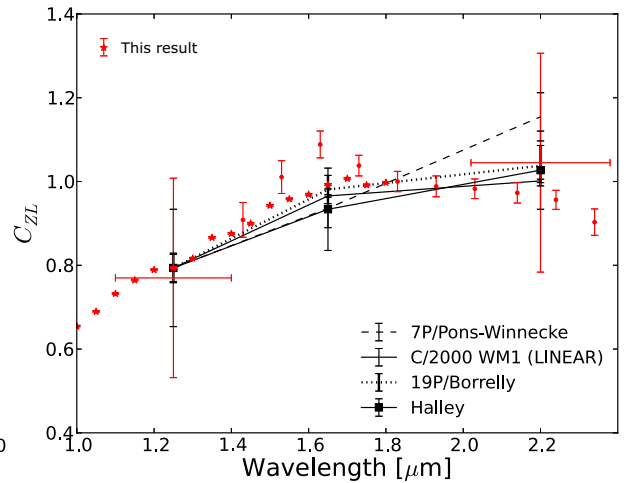


Figure 5.8: Comparison of normalized reflectivity of ZL with the one of the comets. The 7P/Pons-Winnecke, C/2000 WM1 (LINEAR), and 19P/Borrelly were observed by Kelley et al. (2004). The squares indicate the average color of comet Halley which was measured by combining the color of the nuclei (Cruikshank et al. 1985) and the coma (Tokunaga et al. 1986).

### Summary of discussion on the spectrum of Zodiacal Light

We estimate the ZL spectrum from the observed diffuse sky radiation. The ZL spectrum shows redder color than the solar spectrum does. To reveal size of interplanetary dust which is responsible for ZL, we compare the color of ZL with color of Rayleigh scattering, Mie scattering, and Fresnel scattering. Since neither Rayleigh scattering nor Mie scattering can explain the color of ZL, we conclude that the size of interplanetary dust is predominated by much larger particles than wavelength. If we assume the material with refractive index, we can reproduce the color of ZL with Fresnel scattering. We discuss the origin of interplanetary dust. Both color of S-type asteroids and comets can reproduce the color of ZL. Thus both comets and S-type asteroids can be a candidate of the origin of interplanetary dust.

#### 5.1.3 Polarization of Zodiacal Light

We derive the ZL polarization in chapter 4. This is the first measurements of wavelength dependence of polarization of ZL in the near-infrared. In this subsection, we discuss the implication of the ZL polarization. As defined in Chapter 4, we use  $P$  for the degree of polarization.

Figure 5.9 shows the observed polarization as a function of wavelength in six fields. We shows both  $P_{sky} = \frac{I_{pol}}{I_{sky}}$  and  $P_{ZL} = \frac{I_{pol}}{I_{ZL}}$  in this Figure 5.9. There is notable difference between  $P_{sky}$  and  $P_{ZL}$ . Generally speaking  $P_{sky}$  is lower than  $P_{ZL}$ , since  $I_{sky} = I_{ZL} + I_{ISL} + I_{DGL} + I_{EBL}$ . Contribution of  $I_{ISL}$ ,  $I_{DGL}$ , and  $I_{EBL}$  enable  $I_{sky}$  over  $I_{ZL}$  significantly ( $\sim 50\%$ ).

Both  $P_{sky}$  and  $P_{ZL}$  show weak wavelength dependence in all fields. The wavelength dependence of  $P_{sky}$  and  $P_{ZL}$  do not depend on coordinate. On the other hand, absolute value of  $P_{sky}$  and  $P_{ZL}$  depend on coordinate.

We show the observed polarization as a function of solar elongation in Figure 5.10. This Figure shows clear dependence of  $P_{ZL}$  on solar elongation. Generally speaking the degree of polarization is a function of scattering angle. The difference of the absolute value of  $P$  can be explained by difference of solar elongation. We present the dependence of  $P$  as a function of scattering function calculated by

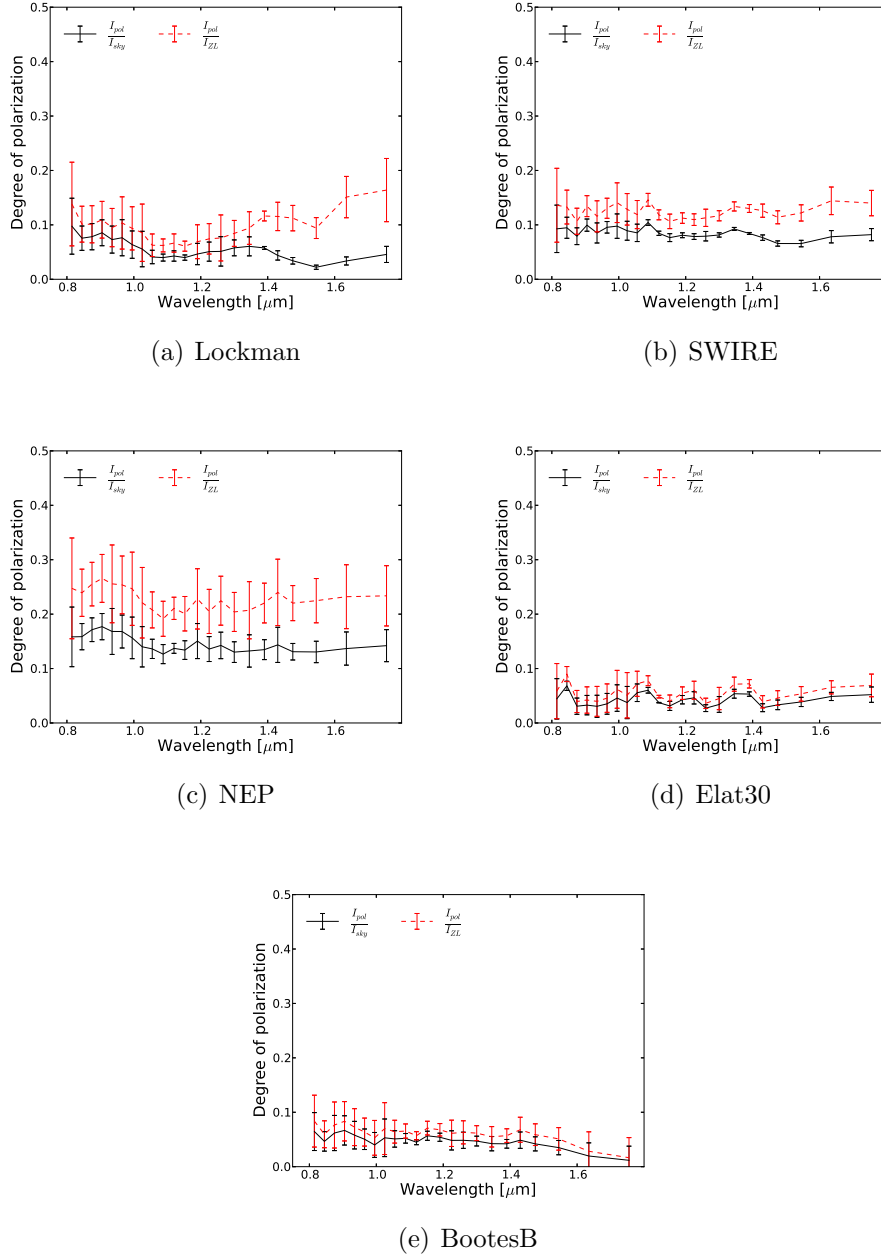


Figure 5.9: The degree of polarization as a function of wavelength. We show both  $\frac{I_{pol}}{I_{sky}}$  with black solid lines and  $\frac{I_{pol}}{I_{ZL}}$  with red dashed lines.

Fresnel scattering and Rayleigh scattering. In this calculation, we assume only closest particles contribute to light scattering, instead of full calculation of the brightness integral along the line of sight, for simplicity. Fresnel model is much more similar to our result than Rayleigh model.

We also compare our result with other experiments in Figure 5.11. Because DIRBE/COBE result indicates that  $P_{sky}$  and the bright star-subtraction are not the same with our result, we cannot directly compare their result with our result. Thus we calculate  $P_{ZL}$  of DIRBE/COBE measurements for direct comparison. We summarize  $I_{sky}$ ,  $I_{ZL}$ , and contribution of  $I_{ISL}$ ,  $I_{DGL}$  and  $I_{EBL}$ , and  $\frac{I_{pol}}{I_{ZL}}$  in Table 5.1.  $P_{ZL}$  of polarization of DIRBE/COBE also show flat wavelength dependence of polarization from  $1.25\mu\text{m}$  to  $2.2\mu\text{m}$ . The wavelength dependence of DIRBE/COBE result is consistent with that of our result.

We are also present  $P_{sky}$  of optical wavelength at the same field as NEP (Leinert 1975) and the same field as DIRBE/COBE (Levasseur-Regourd & Dumont 1980). Optical wavelength data are smoothly connected to our data.

We obtain the polarization of ZL from the third flight observation. This is first measurement of the polarization spectrum of ZL. From our result, we find weak wavelength dependence of  $P$  in the near-infrared. We also see clear dependence of  $P$  on solar elongation, which is consistent with Fresnel scattering. In addition, our result is consistent with  $P_{ZL}$  estimated from DIRBE/COBE result. In the next section, we discuss about size distribution and origin of interplanetary dust based on these result.

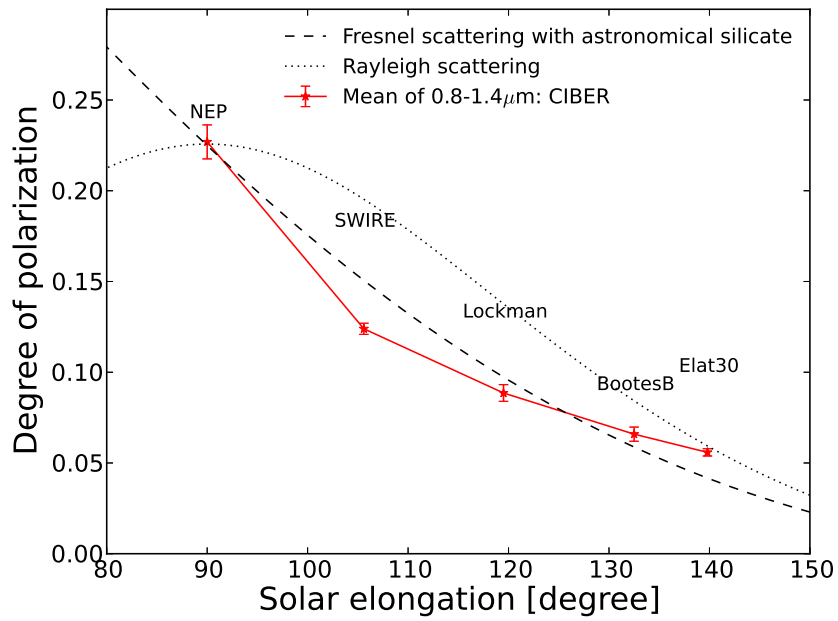


Figure 5.10: The degree of polarization as a function of solar elongation. The red line with asterisks indicates our result. The y-axis indicates mean polarization from  $0.8\mu\text{m}$  to  $1.4\mu\text{m}$ . The x-axis indicates solar elongation. We present Fresnel scattering with astronomical silicate (dashed line) and Rayleigh scattering (dot line). The models are normalized at  $90^\circ$ .

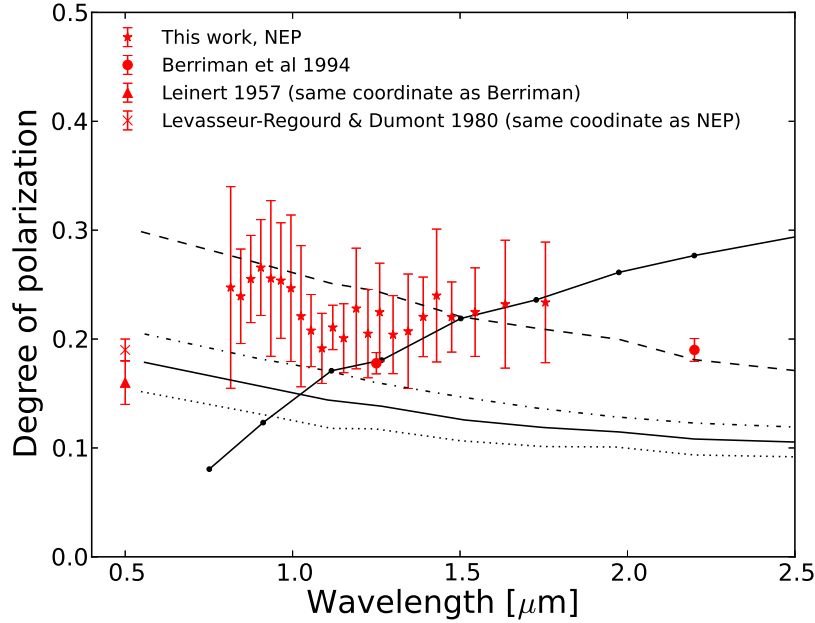


Figure 5.11: Comparison of the our observed degree of polarization of the ZL with Mie scattering model and past observation. Asterisks indicate our result of  $P_{ZL}$  at NEP. The circles indicate DIRBE/COBE data (Berriman et al. 1994). But we recalculate the  $P_{ZL}$  as shown in table 5.1. The triangle is the  $P_{sky}$  of optical wavelength at same coordinate with 5.1,  $\lambda = 10^\circ$  and  $\beta = 0^\circ$  (Leinert 1975). The cross indicates the  $P_{sky}$  of optical wavelength at the same coordinate with NEP of the third flight (Levasseur-Regourd & Dumont 1980). The five Mie scattering is also presented. Dot line: spherical silicate with power low. Dashed line: spherical silicate with dust mass distribution of Grun et al. (1985). Chain line: graphite grains with power low. Solid line: mixture of 50% spherical silicate and 50% spherical graphite. Dots with solid line: Porous silicates with power low.

Table 5.1: Degree of polarization measured by DIRBE/COBE (Berriman et al. 1994). The detection limit of the discrete sources is presented in Arendt et al. (1998), and unit is Jy. The brightness of ZL is calculated with Kelsall et al. (1998). The ISL is integrated more faint stars than the detection limit. The DGL is estimated from our result and Tsumura et al. (2013c). The EBL is referred from Cambr esy et al. (2001). The unit of wavelength  $\lambda$  is  $\mu\text{m}$ . The unit of  $I_{ZL}$ ,  $I_{ISL}$ ,  $I_{DGL}$  and  $I_{EBL}$  is  $\text{nWm}^{-2}\text{sr}^{-1}$ . The  $I_{pol}/I_{sky}$  and  $I_{pol}/I_{ZL}$  is presented by %.

$\lambda$ $\mu\text{m}$	$I_{pol}/I_{sky}$ %	detection limit Jy	$I_{ZL}$ $\text{nWm}^{-2}\text{sr}^{-1}$	$I_{ISL}$ $\text{nWm}^{-2}\text{sr}^{-1}$	$I_{DGL}$ $\text{nWm}^{-2}\text{sr}^{-1}$	$I_{EBL}$ $\text{nWm}^{-2}\text{sr}^{-1}$	$I_{pol}/I_{ZL}$ %
1.25	$12.00 \pm 0.005$	15	$831 \pm 41$	$318 \pm 15$	$10 \pm 1$	$54 \pm 17$	$18 \pm 1$
2.2	$10.00 \pm 0.05$	15	$302 \pm 15$	$257 \pm 13$	$5 \pm 1$	$28 \pm 7$	$19 \pm 1$

### 5.1.4 Discussion on Polarization of Zodiacal Light

In the third flight, we observe the polarization of ZL,  $P_{ZL}$ . We successfully obtain the spectrum of  $P_{ZL}$  in 0.8-1.8 $\mu\text{m}$ .  $P_{ZL}$  shows weak wavelength dependence.  $P_{ZL}$  includes wealth information about interplanetary dust as the ZL spectrum. We also compare  $P_{ZL}$  with polarization of scattering models in this section.

We compare the polarization of ZL with polarization of the Mie scattering in Figure 5.11. The five Mie scattering models by Berriman et al. (1994) show different wavelength dependence from that of the ZL polarization. This result is consistent with the result derived from the discussion on the ZL spectrum.

From the discussion on the spectrum of ZL, we showed that only Fresnel scattering could explain the ZL spectrum. We compare the polarization of ZL with the polarization of Fresnel scattering. One can calculate the polarization of Fresnel scattering as

$$P = \frac{R_{\parallel} - R_{\perp}}{R_{\parallel} + R_{\perp}} \quad (5.5)$$

Figure 5.12 shows the degree of polarization of Fresnel scattering for several materials. We assume the scattering angle of 90° in this Figure. Some materials which have wavelength dependence of the refractive index (see Figure 5.5) makes wavelength dependence of polarization.

We also compare the polarization of ZL with the polarization of the material which can reproduce the color of ZL as shown in Figure 5.6. Figure 5.13 shows the result. The polarization of Fresnel scattering model can explain the polarization of ZL. The dependence of polarization on the solar elongation could be reproduced by the Fresnel model. The result of the ZL polarization also supports the domination of interplanetary dust with the size larger than the wavelength.

From the above discussion, the Fresnel scattering can explain weak wavelength dependence of polarization in the near-infrared. When we assume the material which can reproduce the color of ZL, The Fresnel scattering with the same material also reproduce the polarization of ZL. By comparison the color of ZL with the color of comets and asteroids, we assumed the possibility that the origin of the material can be explained by the comets and asteroids. Thus, we also compare the polarization of ZL with the polarization of comets. Since an asteroid is a

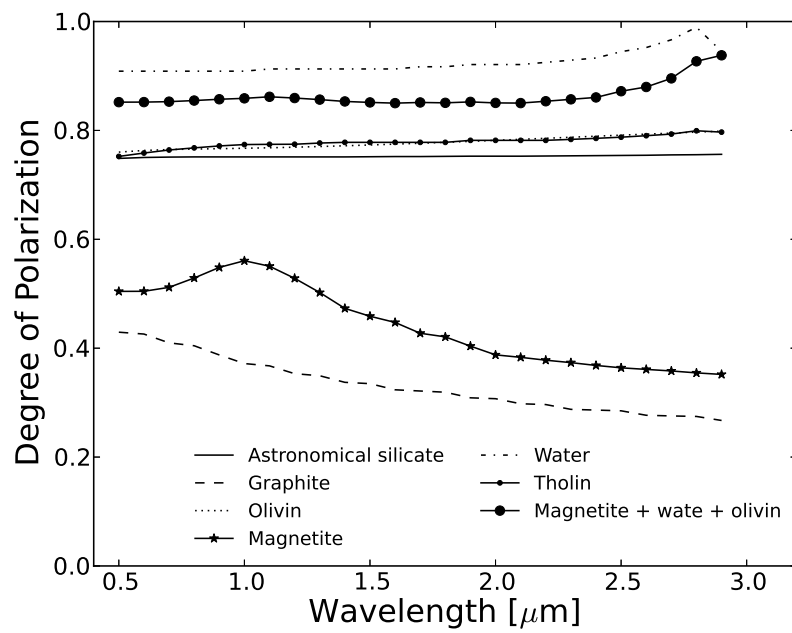


Figure 5.12: Polarization of several materials at scattering angle of  $90^\circ$ , calculated by Fresnel reflection. Relation between lines and materials is presented in legend.

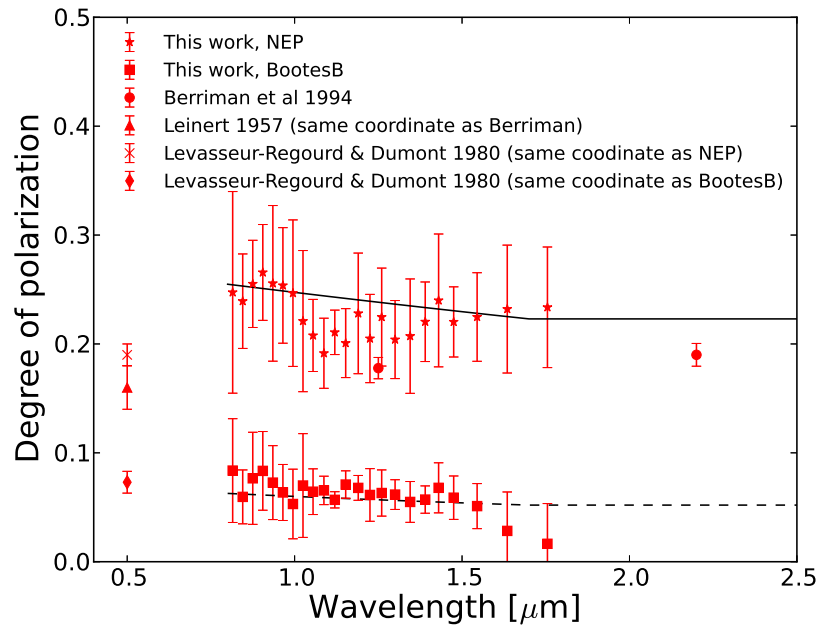


Figure 5.13: Polarization of several materials at scattering angle of  $90^\circ$ , calculated by Fresnel reflection. We assume the material which can reproduce the color of ZL in this calculation. Black lines indicate this Fresnel reflection for NEP and BootesA field. Red asterisks and red squared indicate the polarization of ZL.

bulk body with complex surface structure covered with regolith, it should show different polarization property.

Figure 5.14 shows the polarization of comet C/1995 O1 (Hale-Bopp) from optical to near-infrared measured by several authors. The polarization of the comet also shows weak wavelength dependence. This result indicates that cometary dust can explain not only the color of ZL but also the polarization of ZL. Therefore we consider that comets are candidate of origin of interplanetary dust.

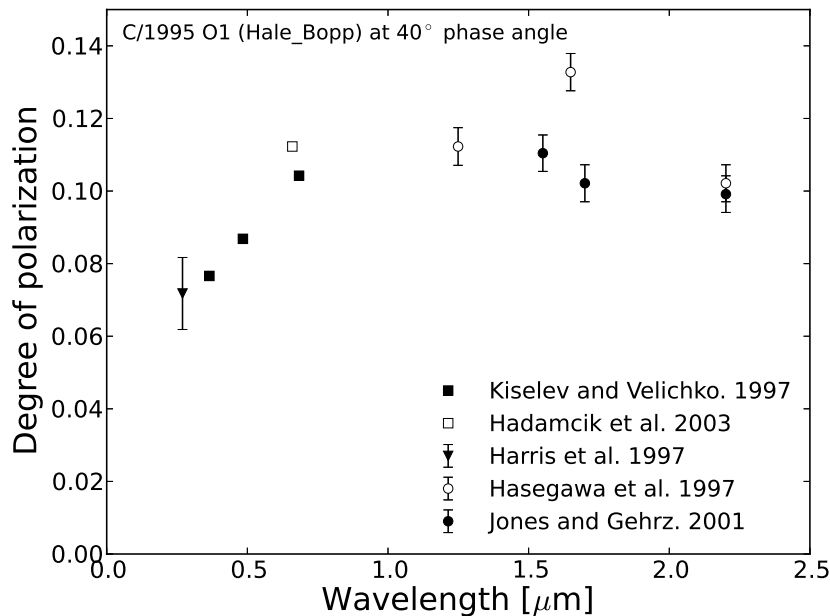


Figure 5.14: Degree of polarization of C/1995 O1 (Hale-Bopp) as a function of wavelength (Kelley et al. 2004). The observation did not conduct simultaneously. The plotted data are extrapolated to  $40^\circ$  phase angle from published data.

### 5.1.5 Summary of Zodiacal Light

The ZL spectrum shows the redder color than that the solar spectrum from 0.8-1.5 $\mu\text{m}$ . This color of ZL can be explained by neither Rayleigh nor Mie scattering.

This result indicates that the interplanetary dust is predominated by larger size dust than the wavelength;  $2\pi a/\lambda \gg 1$ . The size may be  $\sim 100\mu\text{m}$ , which is expected from dynamical simulation of interplanetary dust (Nesvorný et al. 2010), thermal emission of interplanetary dust (Reach et al. 2003), and the direct measurements of the interplanetary dust flux (Grun et al. 1985). The color of the ZL can be explained by the Fresnel scattering with refractive index. In addition, the ZL shows similar color as both comets and S-type asteroids. These results suggest that the origin of interplanetary dust is comets and S-type asteroids.

The polarization of ZL shows weak wavelength dependence in the near-infrared. The polarization of ZL also can be reproduced by the Fresnel scattering with refractive index. This is consistent result of the color of ZL. In addition, the polarization of ZL shows similar wavelength dependence as comets. This result is also consistent with the color of ZL. Both the color and polarization of ZL present same result of size and property of interplanetary dust.

## 5.2 Diffuse Galactic Light

### 5.2.1 Spectrum of Diffuse Galactic Light

As discussed in Chapter 4, we separate the DGL spectrum from the observed sky brightness with two different methods. First one is the global-structure method, we iteratively separate ZL and DGL using global structure of the  $100\mu\text{m}$  brightness. Second one is the local-structure method, we derive DGL from the sky spectrum correlated with the local structure of the  $100\mu\text{m}$  brightness in local field. The spectra of DGL observed with two methods are consistent with each other within the error bar. Figure 5.15 shows the DGL spectrum derived from two different methods of the global-structure method and local-structure method together with optical measurements ( $0.5\sim 0.9\mu\text{m}$ ) and near-Infrared measurements ( $1.7\sim 5.0\mu\text{m}$ ). Our result is consistent with other observations.

Figure 5.16 shows comparison of the DGL spectrum with the ISL spectrum. The x-axis indicate the wavelength. The observed DGL shows the bluer spectrum than the typical star spectrum (solid line).

In the optical wavelength, Ienaka et al. (2013), Matsuoka et al. (2011) and Witt

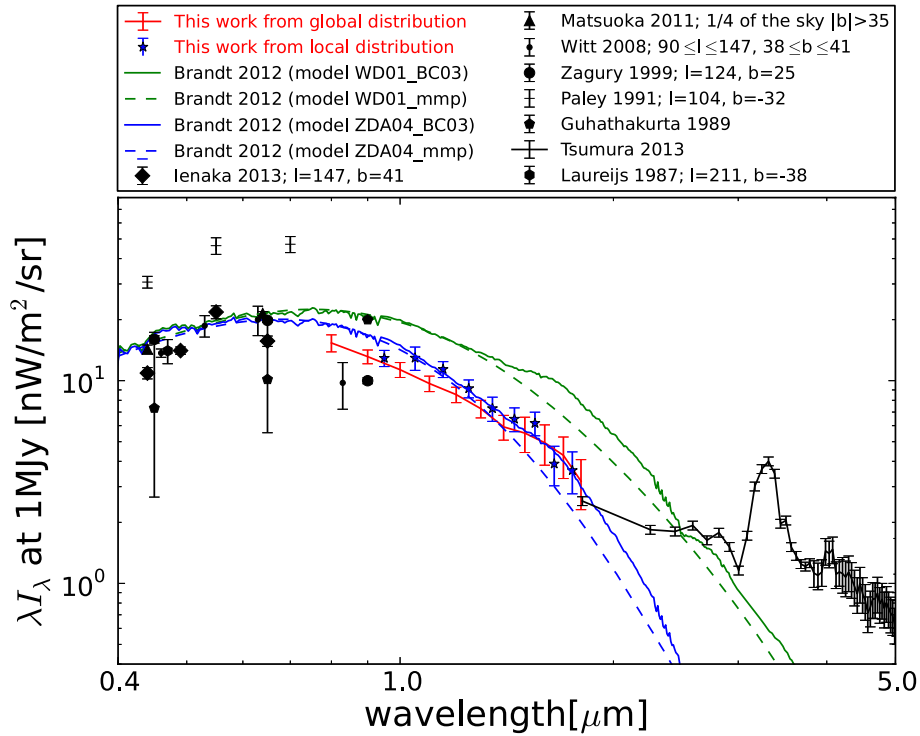


Figure 5.15: The DGL brightness as a function of wavelength from 0.5 to 5.0  $\mu\text{m}$  at the  $100\mu\text{m}$  brightness of  $1\text{MJy}\text{sr}^{-1}$ . The reference of these data is listed in the legend. Our result from local distribution and global distribution is presented as blue asterisks and red line, respectively.

et al. (2008) correlated these observations with SFD-100 $\mu$  map (Schlegel et al. 1998). The spectrum in the optical band is measured by the Brandt & Draine (2012). They analyzed the 92,000 blank-sky spectra from the Sloan Digital Sky Survey (SDSS) and correlated with the SFD-100 $\mu$  map. This spectrum shape is well consistent with each other, but their flux calibration has large uncertainty due to analyze method. Therefore we normalized this spectrum to value of Ienaka et al. (2013). Zagury et al. (1999), Paley et al. (1991), Guhathakurta & Tyson (1989), and Laureijs et al. (1987) used the original IRAS 100 $\mu$ m map (Low et al. 1984). The brightness of the DGL of the optical band is varied by a factor of 3-4. Especially the variation of the DGL based on original IRAS 100 $\mu$ m map is larger than that of the SFD-100 $\mu$ m map. We assume that this variation is due to flux calibration of the original IRAS 100 $\mu$ m map. The DGL spectrum of longer near-infrared wavelength of  $\lambda = 1.8 - 2.0\mu$ m is measured with AKARI by Tsumura et al. (2013c).

We successfully observe the DGL spectrum in the near-infrared. This is the first measurement of the DGL spectrum in the near-infrared. The DGL spectrum of the global-structure method is consistent with that of the local-structure method. The observed DGL spectrum shows bluer spectrum than the star spectrum. Our results are also consistent with other observations.

### 5.2.2 Discussion on Spectrum of Diffuse Galactic Light

As shown in the previous subsection, the DGL spectrum shows the bluer color than the star spectrum. Here, we discuss the size distribution and composition of interstellar dust which can reproduce the DGL spectrum.

The blue color of the DGL means that dust particles smaller than the wavelength  $a < 0.8/2\pi \approx 0.13\mu$ m are mainly responsible for DGL, because the scattering by large particles results in the prevalence of neutral or red color. This result is consistent with measurements of polarization of starlight by interstellar dust. The grains responsible for the polarization has diameter  $a \approx 0.1\mu$ m (Kim & Martin 1995).

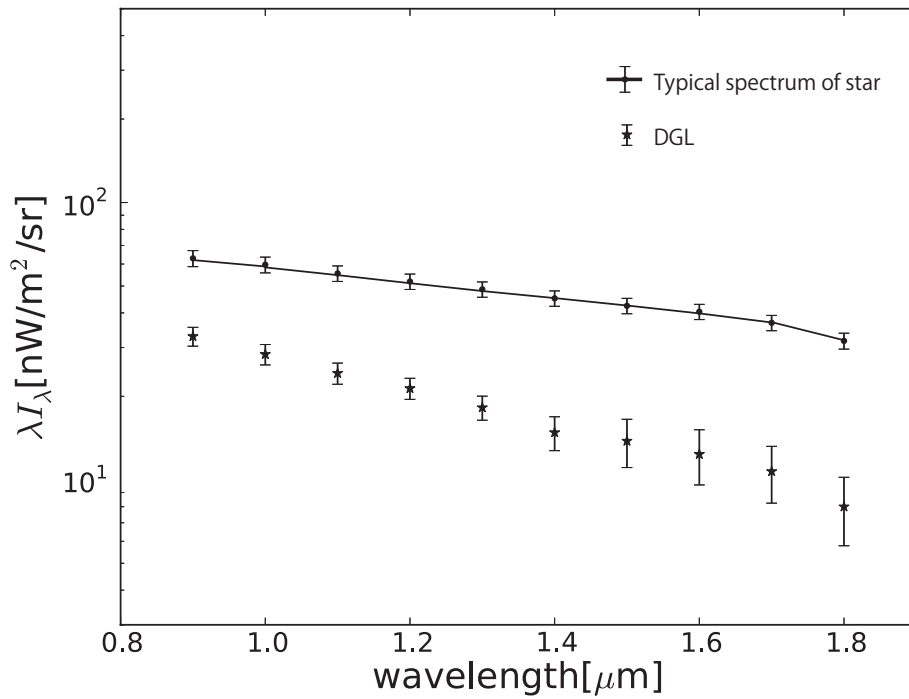


Figure 5.16: Comparison between the DGL spectrum with the typical star spectrum. The asterisk indicates the DGL spectrum. The solid line indicates  $I_{ISL}$  which is total faint stars.

Table 5.2: Summary of interstellar dust scattering models of Brandt & Drain (2012). The dust model is based on Weingartner & Draine (2001) (WD01), and Zubko et al (2004) (ZDA04). The interstellar dust model is based on Mathis et al. (1983) (MMP83) and Bruzual & Charlot (2003) (BC03)

Model name	composition	interstellar dust size	interstellar radiation field
WD01-BC03	graphite, silicate, and PAH	$a_{0.5}=0.12$	stellar population synthesis
ZDA04-MMP83	bare graphite, bare silicate, and PAH	$a_{0.5}=0.06\sim 0.07$	solar neighborhood
WD01-BC03	graphite, silicate, and PAH	$a_{0.5}=0.12$	stellar population synthesis
ZDA04-MMP93	bare graphite, bare silicate, and PAH	$a_{0.5}=0.06\sim 0.07$	solar neighborhood

To reveal detail of size distribution and composition of dust particles, we compare the DGL spectra with theoretical models by Brandt & Draine (2012). Figure 5.15 shows the our observed DGL spectra together with this theoretical models Brandt & Draine (2012).

In this theoretical model, Brandt & Draine (2012) consider an infinite plane-parallel galaxy with a Gaussian vertical distribution of dust from  $\sigma = 25\text{pc}$  (Malhotra 1995; Nakanishi & Sofue 2003), and two-exponential distributions of stars with scale heights of 300pc and 1350pc (Binney & Merrifield 1998; Gilmore & Reid 1983). Brandt & Draine (2012) estimated of the stellar emission spectrum in two ways:(1) a model that reproduces the local interstellar radiation field of Mathis et al. (1983) (hereafter MMP83), (2) a stellar population synthesis model of Bruzual & Charlot (2003) (hereafter BC03) with solar metallicity and an exponential star formation history over 12Gyr. Brandt & Draine (2012) also used two typical dust models Weingartner & Draine (2001) and Zubko et al. (2004) (hereafter WD01 and ZDA04). The dust composition of the WD01 model comprises graphite, silicate, and PAH material. On the other hand, the dust composition of the ZDA04 model consists of bare graphite grains, bare silicate grains and PAHs. Size distribution of the ZD04 model is shifted significantly to smaller side than that of the WD01 model; the half-mass grain radius (50% of the mass in grains with  $a > a_{0.5}$  is  $a_{0.5} \approx 0.12\mu\text{m}$  for both silicate and carbonaceous grains in WD01 model, and  $a \approx 0.06\mu\text{m}$  and  $0.07\mu\text{m}$  for carbonaceous grains and silicate grains respectively (Draine 2011). Dust graines  $a \leq 0.2\mu\text{m}$  absent in ZD04 model. We summarize these models in table 5.2. Because the models underestimate  $b(\lambda)$  by a factor of 2, the model is normalized at  $0.5\mu\text{m}$  to the data of Ienaka et al. (2013). Ienaka et al. (2013) present two possible explanations for this; a deficiency in UV photons of spectrum of the ISRF, and albedo of dust particles assumed in these models.

Our result of the DGL spectrum is consistent with the spectrum of both models of ZDA04. On the other hand, both models of WD01 can not reproduce the observed DGL spectrum. This result indicate that interstellar dust is predominated by small particles of  $a \approx 0.06\mu\text{m}$  and  $0.07\mu\text{m}$  for both silicate and carbonaceous grains. The effect of the difference of two interstellar radiation fields is not significant in the near-infrared wavelength. We can not resolve the interstellar radiation

field from our data.

We separate the DGL spectrum from the observed sky brightness using two different methods with following conclusions.

- The size of the interstellar dust is predominated by  $a \approx 0.06\mu\text{m}$ .
- The composition of interstellar dust are bare graphite, bare silicate and PAH material. The observed DGL can be reproduced by typical composition.

### 5.3 Summary of Discussion of Zodiacal Light and Diffuse Galactic Light

We successfully separate the DGL spectrum and the ZL spectrum from the observed sky brightness. We obtain the polarization spectrum of ZL from the third flight data. From the observations, we obtain following result.

- The ZL spectrum shows the redder color than the solar spectrum.
- The ZL polarization shows weak wavelength dependence.
- The DGL spectrum shows the bluer color than the typical star spectrum.

From these results, we find some important information of physical properties of interplanetary and interstellar dust.

- The size of interplanetary dust is predominated by larger particles than wavelength  $a \gg 5\mu\text{m}$ . Both the spectrum and polarization of ZL can be explained by Fresnel scattering with refractive index.
- Comets and S-type asteroids are candidate of the origin of the interplanetary dust.
- The size of interstellar dust is predominated by smaller particles than wavelength with  $a \approx 0.06\mu\text{m}$ .
- The composition of the interstellar dust can be reproduced bare graphite, bare silicate and PAH material.

The above results clearly shows that there is a clear discrepancy between size of interplanetary dust and that of interstellar dust. This discrepancy is expected from difference of morphosis between interplanetary dust and interstellar dust. The origin of interplanetary dust is propose to be comets and asteroids. The interplanetary dust is debris made from a collision or/and collapse of comets and asteroids. The resultant particles are large. On the other hand, the interstellar dust grows up from mass ejection from stars. The resultant particles cannot be grown up large particles in interstellar enviroment. Thus, this discrepancy between size of interplanetary dust and interstellar dust represents the difference of morphosis.

Understanding of the origin of the interplanetary dust is important not only for the understanding of the history of our solar system but also for the study dust disks around other planetary or planet-forming stellar systems (Wyatt 2008). Interplanetary dust is proposed to play essential roles in the formation process of planets.

The size distribution of interstellar dust also provides us with vital information on the galaxy evolution; since the interstellar dust forms and evolves through various processes in the galaxy evolution, the dust size distribution of interstellar dust is one of most important tracer of processes in the galaxy evolution (Asano et al. 2013). Thus our result of the DGL measurements provides us with important information of the galaxy evolution.

## 5.4 Limit on Extra-Galactic Background Light (EBL)

We now have spectra of all components of diffuse radiation except EBL. From above result, we can set the stringent constraint on the EBL measurements. Thus we summaries the error propagation from uncertainty of foreground and uncertainty of calibration to uncertainty of the EBL measurements.

Figure 5.17 shows the EBL brightness observed by several author. We also present the EBL brightness expected from galaxy count (Totani et al. 2001). From these results, we assume the upper limit of the EBL brightness as  $\sim 50 \text{ nW m}^{-2} \text{ sr}^{-1}$

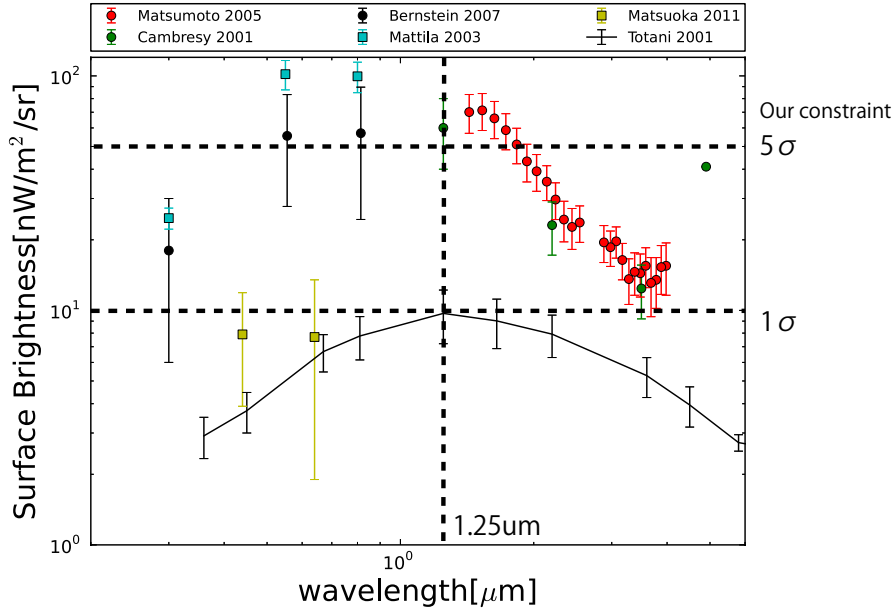


Figure 5.17: EBL at near-IR and optical wavelengths, showing upper limits, reported after subtraction of local foregrounds, and integrated galaxy counts. The our detection limit of the EBL measurements is also presented with a dashed line. Green circles present the EBL (Cambresy et al. 2001) measured with COBE/DIRBE. Red circles indicate the spectrum of the EBL (Matsumoto et al. 2005) measured with AKARI. Blue squares and black circles shows optical EBL(Mattila 2003; Bernstein 2007) measured with HST. The yellow squares are observed by Matsuoka et al. (2011) from heliocentric distances  $>3\text{AU}$  using Pioneer 10 data. The black line present integrated galaxy counts calculated by Totani et al. (2001)

from DIRBE/COBE data, and lower limit of the EBL brightness as  $\sim 10 \text{ nWm}^{-2} \text{sr}^{-1}$  from the galaxy count model at  $1.25 \mu\text{m}$ .

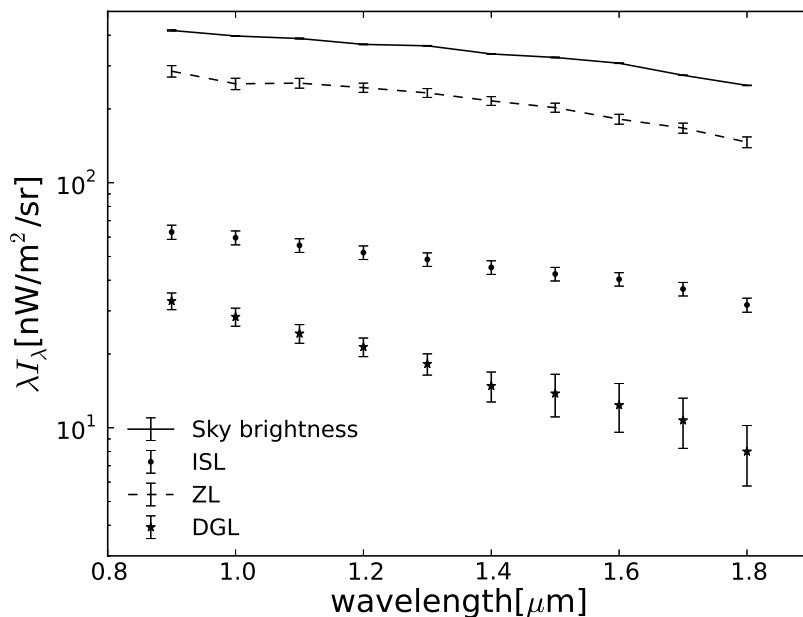


Figure 5.18: Components of diffuse radiation. Black line indicates the sky brightness after removing the airglow emission. Dashed line indicates the ZL spectrum. Circles indicate the ISL spectrum. Asterisks indicate the DGL spectrum.

Figure 5.18 shows components of diffuse radiation at NEP of the second flight. Table 5.3 summarizes the statistical uncertainty of the foreground. Note that the statistical uncertainty of the dark current is included into the uncertainty of the sky brightness. Table 5.4 summarizes the systematic uncertainty in this analysis. There is systematic uncertainty in the flux calibration. The systematic uncertainty is due to the model uncertainty, because the star count produced by the model is slightly different from the deep count observation (see Appendix A). The dark current has not only the statistical uncertainty but also the systematic uncertainty, because we estimate the dark current of the field of view region from the masked region (see Chapter 4). We assume the EBL brightness of

Table 5.3: Summary the statistical uncertainty of foregrounds. As an example, we assume the vale of NEP of the second flight at  $1.25\mu\text{m}$

Item	brightness [ $\text{nWm}^{-2}\text{sr}^{-1}$ ]	uncertainty [%]	uncertainty [ $\text{nWm}^{-2}\text{sr}^{-1}$ ]
Sky	340	0.5	$\sigma_{\text{sky}} = 2$
ZL	235	1	$\sigma_{ZL} = 2$
ISL	35	10	$\sigma_{ISL,st} = 4$
DGL	20	15	$\sigma_{DGL} = 3$
Airglow	-	-	$\sigma_{\text{air}} = 0.7$

Table 5.4: Summary of systematic uncertainty. As an example, we assume the EBL brightness of  $50\text{nWm}^{-2}\text{sr}^{-1}$ .

Item	uncertainty [%]	uncertainty [ $\text{nWm}^{-2}\text{sr}^{-1}$ ]
Flux calibration	4	$\sigma_{\text{flux}} = 2$
ISL model	-	$\sigma_{ISL,sy} = 1$
Dark-current subtraction	-	$\sigma_{\text{dark}} = 0.7$

$50\text{nWm}^{-2}\text{sr}^{-1}$  in the calculation to convert from % to  $\text{nWm}^{-2}\text{sr}^{-1}$ .

From these results, we can estimate the total uncertainty for the EBL measurements as follows.

$$\sigma_{EBL} = \sqrt{\sigma_{\text{sky}}^2 + \sigma_{ZL}^2 + \sigma_{ISL,st}^2 + \sigma_{DGL}^2} + (\sigma_{\text{flux}} + \sigma_{ISL,sy} + \sigma_{\text{dark}} + \sigma_{\text{air}}) \quad (5.6)$$

Where  $\sigma_{\text{sky}}^2, \sigma_{ZL}^2, \sigma_{ISL,st}^2, \sigma_{DGL}^2$  present the statistical uncertainty of foreground summarized in table 5.3,  $\sigma_{\text{flux}}, \sigma_{ISL,sy}, \sigma_{\text{dark}}, \sigma_{\text{air}}$  present the systematic uncertainty of this measurements summarized in table 5.4. We obtain the  $1\sigma$  uncertainty for the EBL measurements as  $\sigma_{EBL} = 10\text{nWm}^{-2}\text{sr}^{-1}$ .

When the EBL brightness is same as the observed brightness by DIRBE/COBE at  $1.25\mu\text{m}$ ,  $\sim 50\text{nWm}^{-2}\text{sr}^{-1}$ , we can detect the EBL brightness  $5\sigma$ . On the other hand, when the EBL brightness is same as the expected brightness by (Totani et al. 2001; Keenan et al. 2010),  $\sim 10\text{nWm}^{-2}\text{sr}^{-1}$ , we measure the EBL brightness

with  $1\sigma$ . The dashed horizontal lines in Figure 5.17 indicate the detection limit of  $1\sigma$  and  $5\sigma$ . Current models of star formation of reionization epoch cannot reproduce the excess of the measured EBL. Thus, if we measure the excess of the EBL with accurate subtraction of ZL and DGL, we provide information for some new physical mechanisms. In the not-too-distant future, we will be able to report the EBL spectrum.



# Chapter 6

## Conclusion

In this thesis, we describe the result of the near-infrared diffuse radiation observed from the space. In the near-infrared, diffuse radiation consists of Zodiacal Light (ZL) which is scattered sunlight by interplanetary dust, unresolved star light, Diffuse Galactic Light (DGL) and Extra-galactic Background Light (EBL). ZL includes the information on physical property of interplanetary dust. DGL includes information on the physical property of interstellar dust. EBL is an integrated radiation produced by stellar nucleosynthesis and gravitational accretion over the history of the universe.

We carried out Cosmic Infrared Background Experiment (CIBER) to measure these diffuse radiations, we conducted the experiments with a sounding-rocket to measure the sky brightness from the space, in order to avoid huge contamination caused by atmospheric emission. The payload of CIBER comprised four instruments. In this thesis, we described the results of one of the instruments called LRS, which was designed to measure the spectrum and polarization spectrum of diffuse radiation. LRS covered the wavelength range  $0.75\text{-}2.0\mu\text{m}$  with wavelength resolution of  $R=15\text{-}30$ .

CIBER has been flown four times, from White Sands Missile Range or Wallops Flight Facility. In the second flight and the third flight, the rocket reached altitude of 300km and observed the sky during 240sec using two-stage rocket. In the fourth flight, the rocket reached altitude of 600km and observed the sky during 335sec using four stage rocket. We observed five of six fields of  $5\times 5\text{deg}$  area of sky in

each flight with LRS. We selected observed fields based on the ecliptic latitude which decides the brightness of ZL, and column density of interstellar dust which decides the brightness of DGL, to separate the zodiacal light and diffuse galactic light from the observed diffuse radiation.

We successfully observed diffuse radiation from the sky. The observed diffuse radiation was processed with flux calibration factors obtained in the laboratory and in-flight stability checks. The uncertainty of flux calibration and the stability of the detector response was estimated to be less than 3%.

We found contamination by the airglow emission at the altitude lower than 250km, and subtracted them to negligible levels (<10% at lowest field, <1% at other field) based on their exponential time and altitude dependence. We then masked all the brighter stars than 13 magnitude, which is detected as discrete sources. In addition, we estimated the faint star contribution by Monte-Carlo simulation of the star distribution using 2MASS catalogues and TRILEGAL galaxy model, and subtracted them from the observed diffuse radiation. The resultant spectrum of the diffuse radiation from the sky consists of ZL, DGL, and EBL.

We decomposed the sky brightness into each component of ZL, DGL, and EBL. We first extracted the ZL spectrum by the difference between two fields which have the similar DGL brightness. In the same way, we also obtained the DGL spectrum by the difference between two fields which had the similar ZL brightness. However, the S/N of these spectra were too low to derive the EBL spectrum. We then iteratively found self consistent results of the ZL and the DGL spectrum with high S/N (the global structure method). In the first step of this iterative analysis, we correlated the sky brightness with the brightness of interstellar dust emission measured at  $100\mu\text{m}$ , assuming universality of the conversion factor from  $100\mu\text{m}$  brightness to the DGL brightness. Before this analysis, the ZL spectrum which was derived from the difference between two fields were subtracted. The slope of the linear correlation provides us to the conversion factor from the  $100\mu\text{m}$  brightness to the DGL brightness. In the second step, we correlated the sky brightness with the most conventional ZL model based on the COBE/DIRBE data. We pre-subtracted the DGL brightness derived in the first step. Then we subtracted the ZL brightness from the sky brightness and fed back to the first step. The uncertainty of the resultant spectrum of ZL and DGL are better than

1% and 15%, respectively. We can also separated the DGL spectrum using local-structure of spatial distribution of the  $100\mu\text{m}$  brightness. Thus we correlated the sky brightness with the  $100\mu\text{m}$  brightness in an local field. We obtained consistent result of the DGL spectrum with that of the global-structure method.

Some important scientific results derived from the ZL spectrum and polarization are the followings:

- The ZL spectrum shows redder spectrum than the solar one does in near-infrared.
- The ZL polarization spectrum shows weak wavelength dependence in the near-infrared. ZL is polarized  $22.6\pm 1\%$  at the NEP field.
- The red color of ZL and flat polarization of ZL requires large dust particles;  $2\pi a/\lambda \gg 1$
- The red color of ZL is similar to that of comets, which indicates that comets are one of candidate of origin of interplanetary dust.
- The red color of ZL is also similar to that of asteroids, which is also candidate of origin of interplanetary dust.

Some important scientific results derived from the DGL spectrum are the followings:

- The DGL spectrum shows bluer color than the mean spectrum of stellar radiation, which indicates that the interstellar dust is predominated by smaller particles than the wavelength;  $2\pi a/\lambda \ll 1$
- The DGL spectrum is consistent with scattering models of interstellar dust by small particles ( $a_{0.5} \approx 0.06\mu\text{m}$ ) consisting of bare graphite, bare silicate and PAH.

From above result, we set stringent constraint on the EBL measurements.

- We can detect the observed EBL ( $\sim 50\text{nWm}^{-2}\text{sr}^{-1}$ ) with  $5\sigma$ , and the expected EBL from galaxy count ( $\sim 10\text{nWm}^{-2}\text{sr}^{-1}$ ) with  $1\sigma$ .

For a future observations of the near-infrared diffuse radiation, we are planning to a new rocket experiment and a space probe. We call the new rocket experiment as CIBER-2 (see figure 6.1) . CIBER-2 has a 30cm Cassegrain telescope with four simultaneous imagers which covers the wavelength range from  $0.5\mu\text{m}$  to  $2.1\mu\text{m}$ . Since the telescope of CIBER-2 has eight times larger area than that of CIBER, CIBER-2 measure the EBL with ten times higher sensitivity and three times higher spatial resolution than that of CIBER. The optics and detectors are cooled to 77K using the same cryostat design as one of CIBER. We are planning to launch the CIBER-2 at 2015.

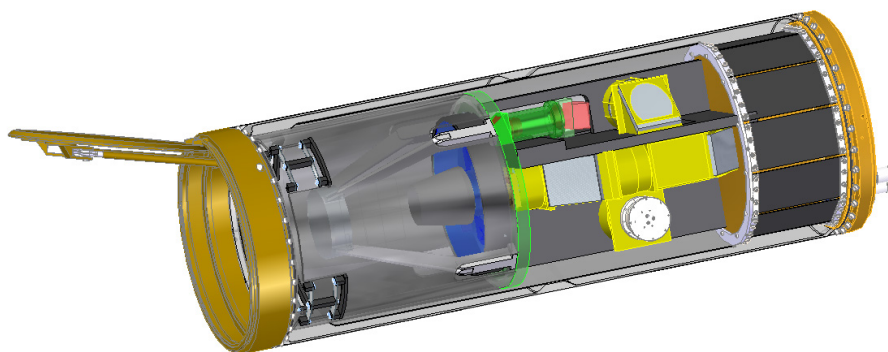


Figure 6.1: Solid model of CIBER-2. A 30cm Cassegrain telescope reflects light to beam splitters, and images onto focal planes by refracting optics. A LN<sub>2</sub> cryostat, a duplicate of the CIBER instrument, cools the optics and detectors. A cryogenic pop-up baffle and radiatively-cooled door linear and used to prevent stray light from thermal emission of the locket skin. Warm read-out electronics, a duplicate of the CIBER design, are mounted to the end of the section on a vacuum bulkhead.

We are also planning the space probe mission, EXZIT (EXo-Zodiacal Infrared Telescope). Since ZL is brightest foreground for the EBL measurement, the subtraction of ZL makes large systematic uncertainty in the EBL measurement. Thus we plan to observe EBL at outside the zodiacal cloud. As shown in figure 6.2, the estimated brightness of the ZL is about 1/50-1/100 than the brightness at 1AU,

which is lower than the brightness of the EBL. EXZIT instrument is one of the instrument of Solar Power sail mission to Jupiter and Trojan asteroids.

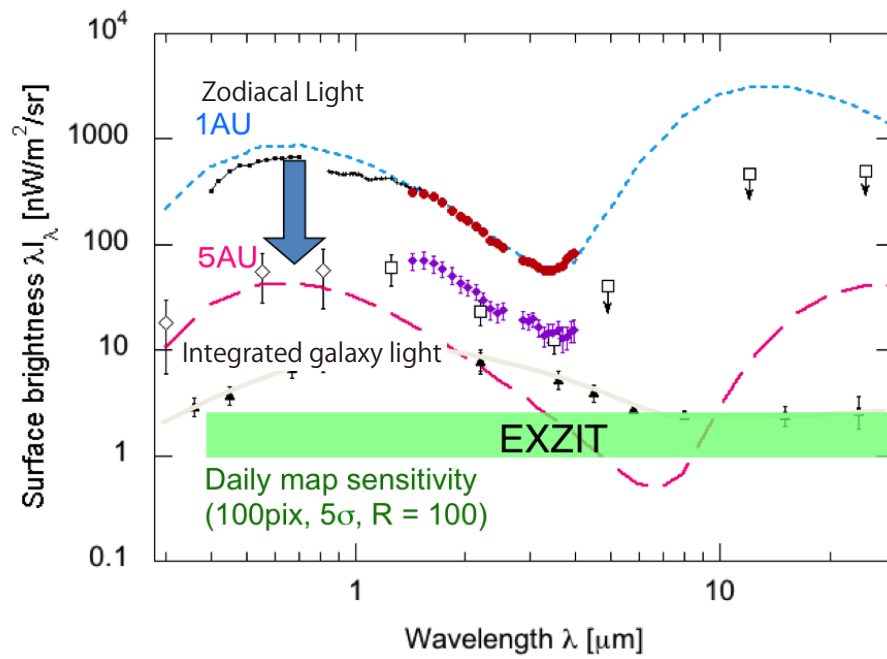


Figure 6.2: The brightness of the ZL from 1AU and 5AU. The estimated brightness of the ZL at 5AU is about 1/50-1/100 of that at 1AU.



# Appendix A

After basic data reduction including the dark current subtraction and the bright stars removal, we obtain the observed brightness. Ideally, the observed brightness should consist of only astronomical components of ZL, ISL, DGL and EBL. However, the observed brightness is contaminated by the airglow which is composed of stable atmospheric emission showing altitude dependence and time decaying emission may be due to outgassing from the rocket payload. Contamination of the airglow is as serious a problem at the beginning of the observation. We therefore remove this contamination from the data. In this Appendix, we introduce the method of the subtraction of the airglow.

Figure 6.3 shows the observed sky brightness of the second flight. The error bar is mainly due to the systematic error of the flux calibration. Only the spectrum of the SWIRE field which is observed at early time after the launch has a different shape from those of the other fields and has peaks at 1.1 and 1.6 $\mu\text{m}$ . From its spectral shape, we attribute this component mainly to OH molecules from either atmospheric airglow or dissociated water vapor outgassed from the payload early in the flight.

Figure 6.4 and 6.5 show the altitude dependence and the time dependence of the mean photocurrent at 1.6 $\mu\text{m}$ . We divide a long-time integration data at one field into sub-data with short integration time. As seen in Figure 6.5 the observed brightness in ascent is much brighter than that of descent at the same altitude. This result implies the existence of a time decaying emission component in early time of the field.

To remove the brightness of airglow emission, we assume an exponential decay

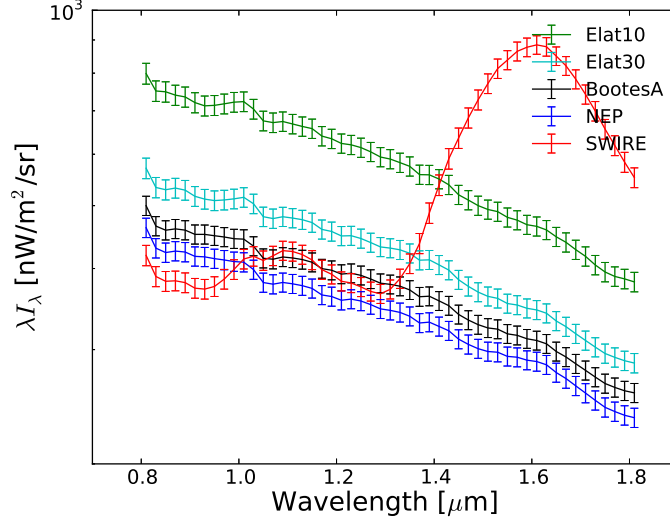


Figure 6.3: The observed brightness of the second flight.

model with time and altitude as follows.

$$I_{obs} = I_{sky} + I_t \exp\left(-\frac{t}{\tau}\right) + I_h \exp\left(-\frac{h}{S_h}\right) \quad (6.1)$$

where  $I_{obs}$ ,  $I_{sky}$  is the observed brightness and the astronomical sky brightness, respectively, the  $I_t$  is the brightness of time decay component at time  $t = 0$ sec, the  $I_h$  is the brightness of altitude decay component at time  $h = 0$ km. Then we convert this equation to a function of the raw signal output from each pixel as follows.

$$S = a + It + c_1 \exp\left(-\frac{t}{\tau}\right) + c_2 \exp\left(-\frac{h}{S_h}\right) \quad (6.2)$$

Where the  $S[e-]$  indicates the signal output of a pixel as the integrated charged electron, the  $I_{sky}[e-/sec]$  is the photocurrent which is assumed to be constant. The third term presents the time decay component of the airglow, where  $\tau$  indicates the time decay constant. The fourth term presents the altitude decay component of the airglow, where  $S_h$  indicates the scale height of the atmospheric layer. In the Chapter 3, we used the linear fitting method to measure the photocurrent

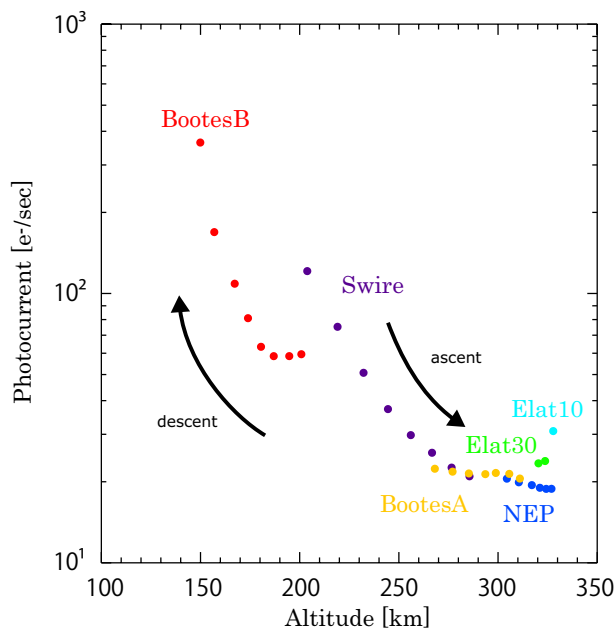


Figure 6.4: Altitude dependence of the observed brightness. The different color indicates a different field. The y-axis indicates photocurrent. The x-axis indicates the altitude of the payload.

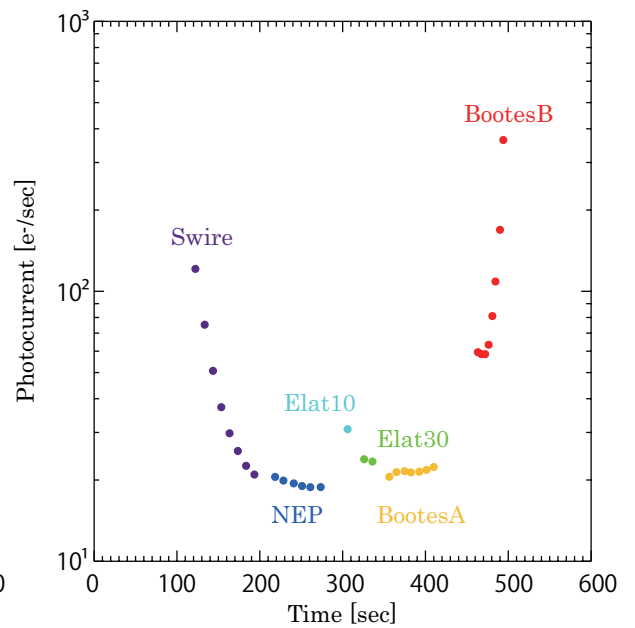


Figure 6.5: Time dependence of the observed brightness. The different color indicates a different field. The y-axis indicates photocurrent. The x-axis indicates the altitude of the payload.

from the raw data. To separate the time and altitude decay component from astronomical emission components, we use the Equation 6.2 instead of the linear function.

Figure 6.6 shows the fitting result for the SWIRE data. The blue line indicates the raw data. The green line indicates the fitting result. We also present the residual of the model fit. The result shows our model of the airglow works well. To measure the photocurrent of the sky brightness, we use the linear term only.

Figure 6.7 shows the time constant  $\tau$  and the scale height  $S_h$  derived from the fitting result as above. This result indicates that the time constant and the scale height depend on the wavelength, with maximum values of  $\tau = 19.2 \pm 0.5$  [sec] and  $S_h = 100.9 \pm 0.2$  km at  $1.65 \mu\text{m}$ .

From this fitting result, we can separate the airglow from the observed sky brightness. Figure 6.8 shows the brightness of the astronomical component (blue circles), the airglow component (red squares) compared with the observed sky brightness. We estimated the error of the airglow emission from the variance of fitting parameter error of all pixel of the detector. We subtracted the airglow emission from the first two fields for all the fields. We also subtract the airglow emission from the last field. Figure 6.9 shows the contribution the airglow emission to the observed brightness. Blue line indicates the time decay component. Red line indicates the altitude dependent component. From this result, the airglow contribution to the observed sky brightness is negligible at the middle fields of the flight after 250sec and above 250km.

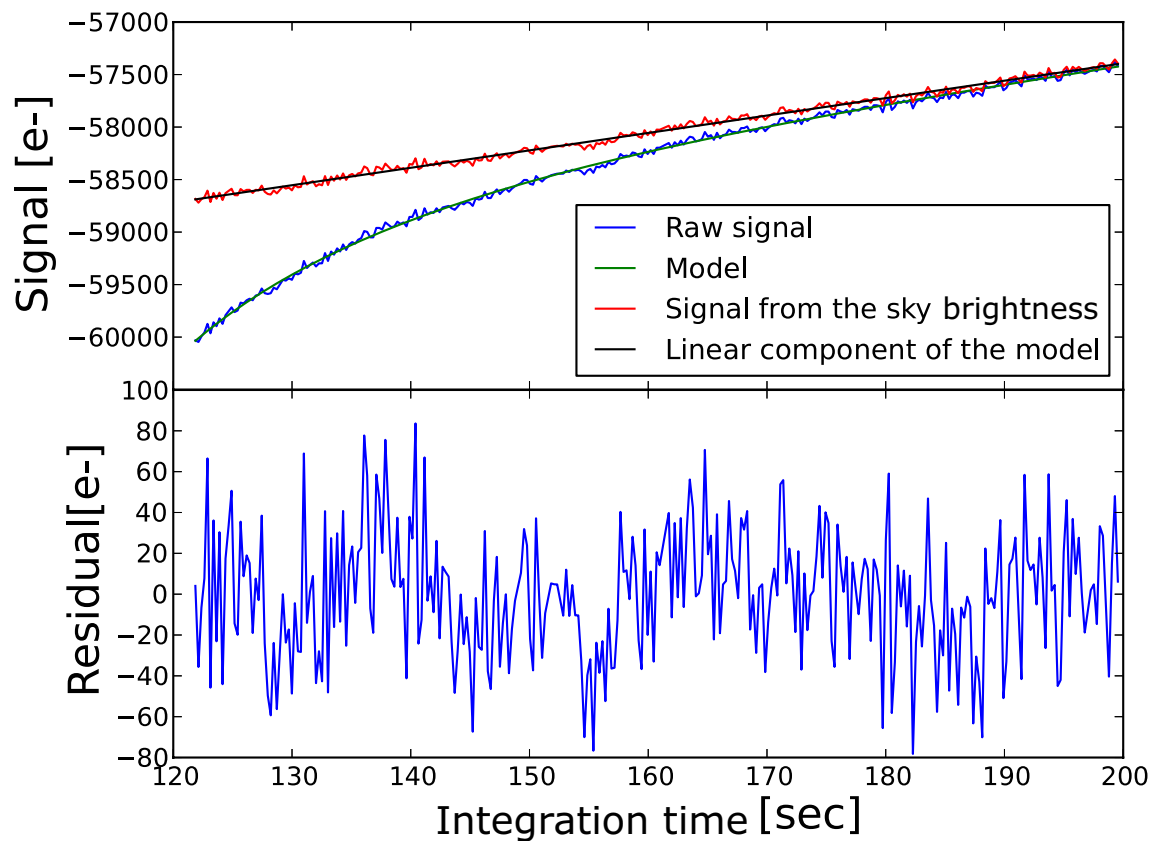


Figure 6.6: The fitting result of Equation 6.2 to the raw data in the top panel. The y-axis indicates the output signal as the integration time. The x-axis indicates the integration time. Blue line indicates raw data. Green line indicates the fitting result of Equation 6.2 to the raw data. Red line presents the separated linear component of the raw data. Black line presents the linear component of the fitting result. The bottom panel shows the residual.

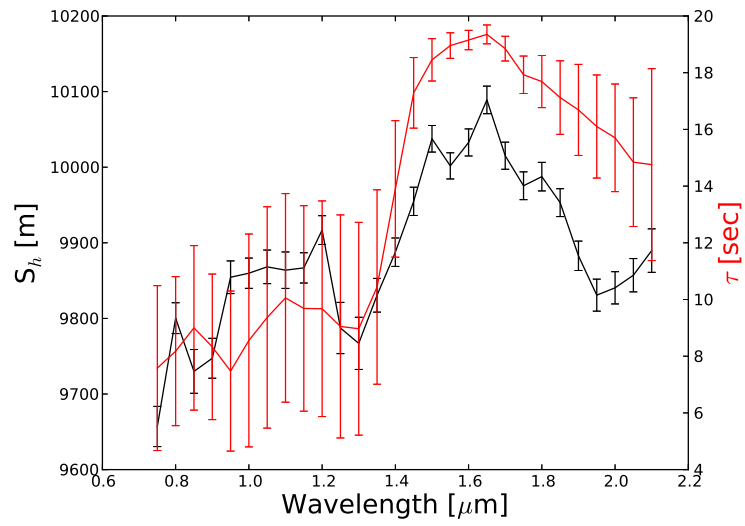


Figure 6.7: The time constant  $\tau$  and the scale height  $S_h$  as a function of wavelength.

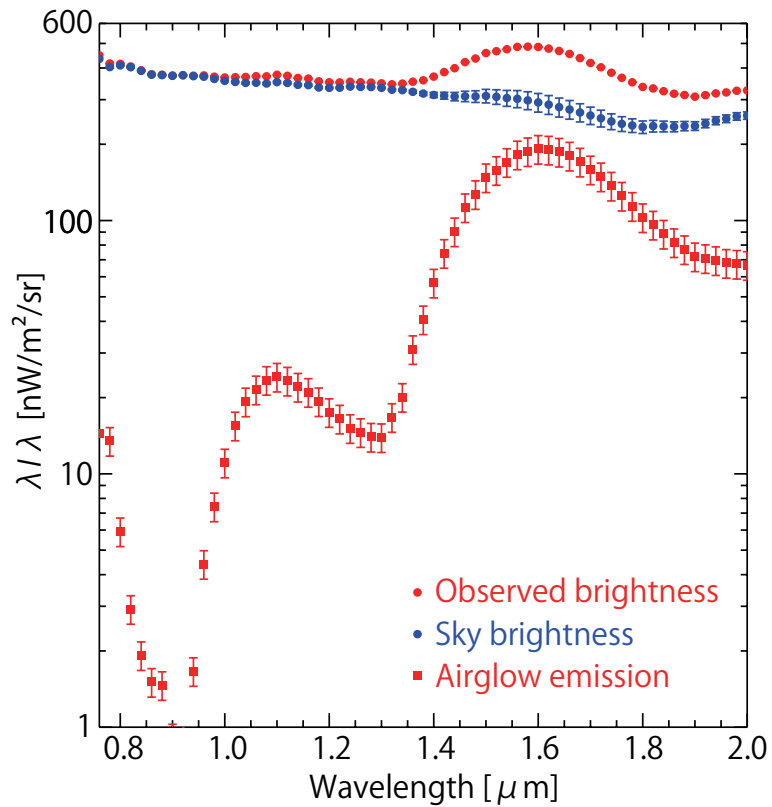


Figure 6.8: Red circles indicate the observed sky brightness. Red squares indicate the brightness of airglow emission. Blue circles indicate the sky brightness after subtracting the airglow emission. We estimated the error bar of the airglow emission from the variance of parameter error of all pixel in the detector.

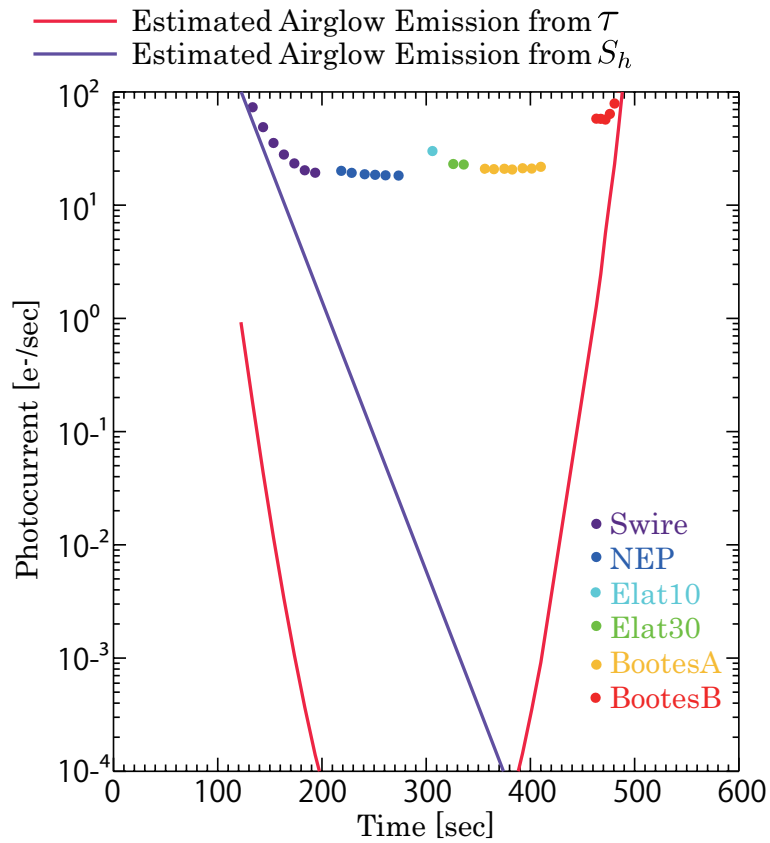


Figure 6.9: Circles indicate the observed brightness of each field. The blue line indicates the airglow emission of time dependent component. The red line indicates the airglow emission of altitude dependent component.

# Appendix B

## Integrated faint stars light

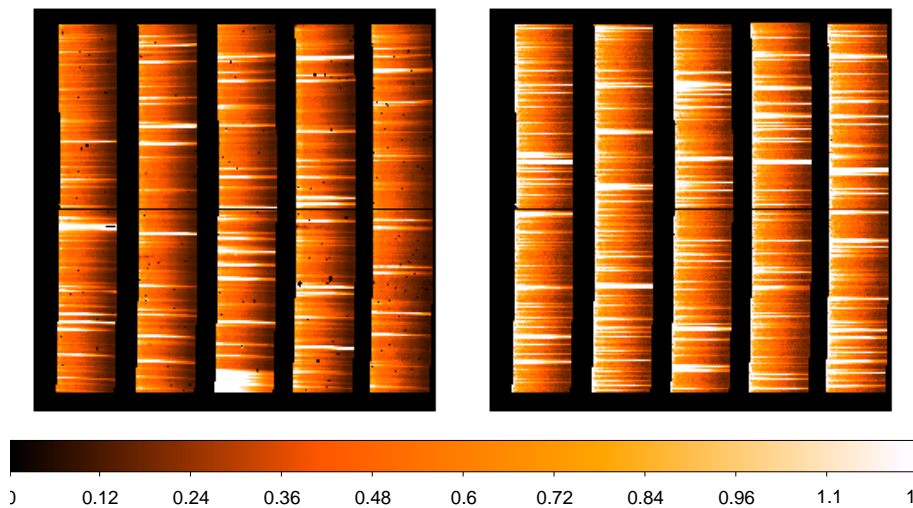


Figure 6.10: Left: observed image of NEP field. Right: simulated image of NEP field.

ISL is total brightness of the unresolved Galactic stars fainter than the detection limit of LRS. ISL is primary components of the Galactic emission.

To estimate the spectrum of ISL, we carried out the Monte-Carlo simulation of the star distribution and integrate the fluxes of the faint stars fallen in the FOV. We show the simulated image and observed image of the NEP field of second flight in Figure 6.10. We used 2MASS catalogues for J-band magnitude

of  $J \leq 17$  magnitude, and contemporary model of star counts named TRILEGAL galaxy model (Girardi et al. 2005) for  $17 < J \leq 32$  magnitude. The FOV is determined from the slit width and the point spread function (PSF) measured with the detected stars. The read-out noise is estimated from the observed image and added to the simulation data. Then we removed bright stars with the  $2\sigma$  clipping method as shown in Chapter 4. To check the validity of the Monte-Carlo simulation, we compared the simulated counts of bright stars with our observed star counts in the 2MASS bands as shown in Figure 6.11. The simulated counts are consistent with the observed counts within the Poisson error. The TRILEGAL galaxy model builds a geometric model of the Milky Way, including main components such as the thin and thick disks, the halo and bulge, each one containing a particular stellar population. The stellar population is defined by means of a star formation rate and the age-metallicity relation. Girardi et al. (2005) calibrate the TRILEGAL model with deep star observations. They find that discrepancies between the model and observations are  $<30\%$ . Thus, to quantify these discrepancies in our observed fields, we compared counts the star of the TRILEGAL model with deep source counts by the ground observations NEWFIRM (Gonzalez et al. 2010) and MEGACAM (Oi 2013), down to  $AB = 20$  mag in J-band as shown in figure 6.12. We find that counts of TRILEGAL model are 20% lower than the deep counts at  $17 \leq J \leq 20$  mag. Because stars of  $J \leq 17$  are predominant in ISL, this discrepancy gives only a few uncertainty of the  $1nWm^{-2}sr^{-1}$  to the ISL brightness. We assume the difference between the TRILEGAL model counts and the deep source count is systematic uncertainty.

To estimate the uncertainty of the spectrum of ISL, we repeat the Monte-Carlo simulation hundred times. As the result, the variance of the simulation is  $\sim 5\%$ . We also found that there is a slight color difference between the TRILEGAL counts and 2MASS counts of  $<5\%$ . Therefore the total uncertainty of ISL is 10%. We assume this 10% uncertainty is statistical uncertainty.

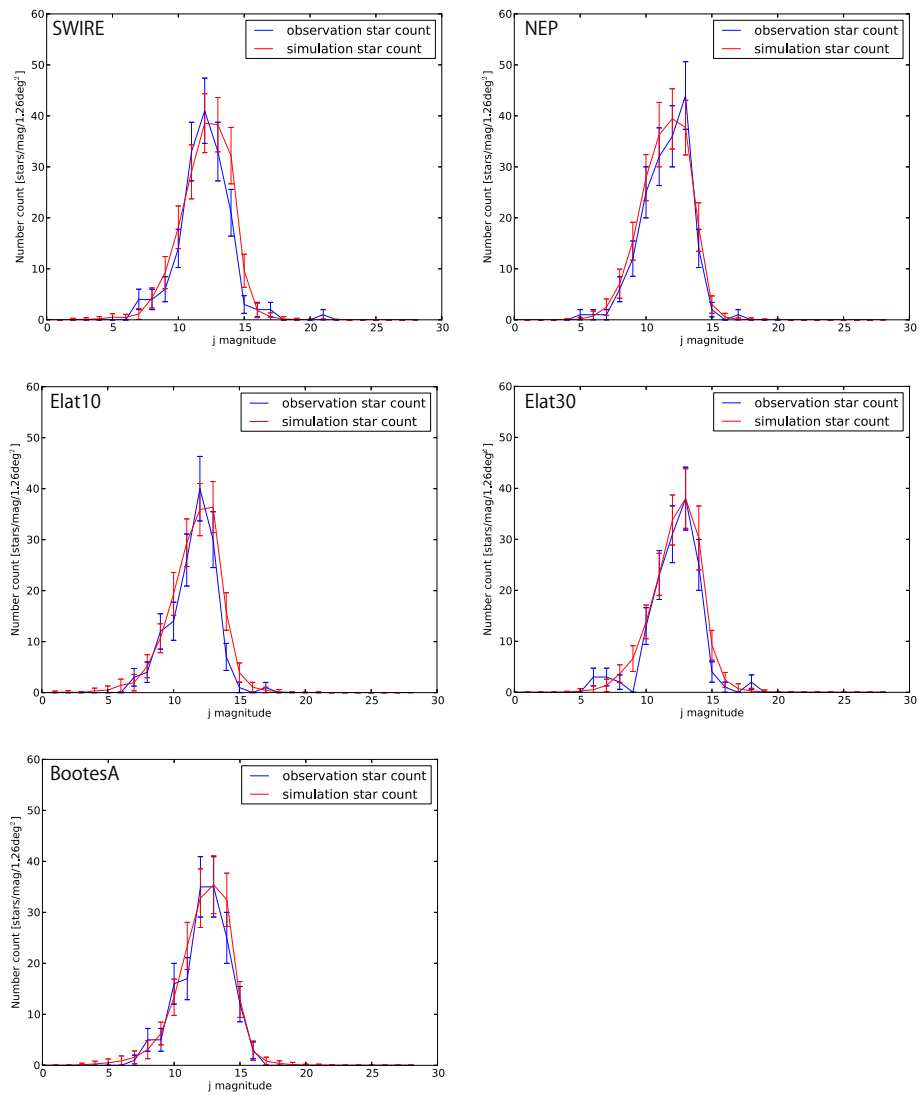


Figure 6.11: The counts of clipped bright stars. The red line indicates simulated counts. The blue line present observed count. The x-axis shows the J-band magnitude with AB system. The y-axis indicate the number of counts

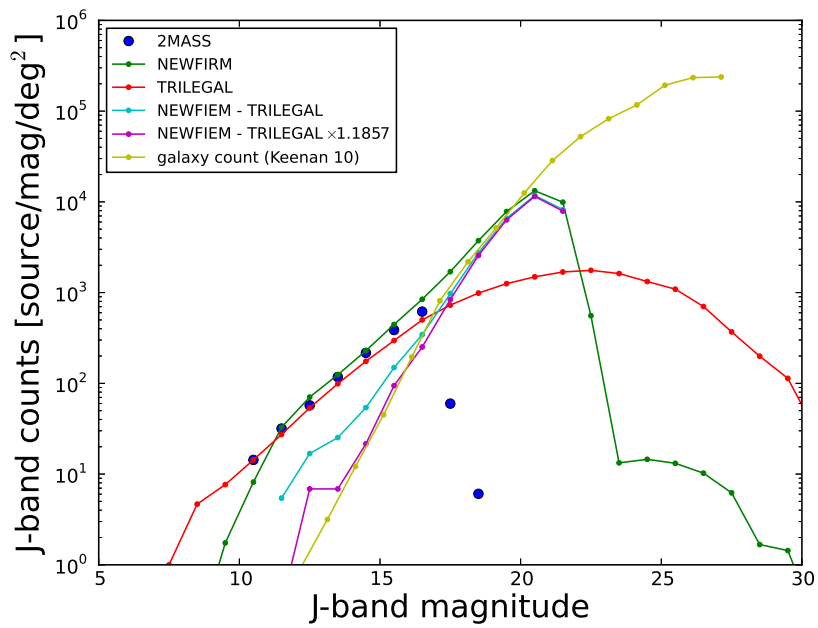


Figure 6.12: The counts of clipped bright stars. The red line indicates simulated counts. The blue line present observed count. The x-axis shows the J-band magnitude with AB system. The y-axis indicate the number of counts.

# Acknowledgments

I am very grateful to my supervisor Prof. Takao Nakagawa for giving me a great opportunity to study the infrared astronomy. My appreciation goes to Dr. Shuji Matsuura for inviting me to this CIBER project and also for thier valuable guidance throughout my all research activity.

Dr. Toshio Matsumoto, Dr. Koji Tsumura, Dr. Mai Shirahata, and Mr. Yosuke Onishi at ISAS/JAXA are key members in my work. They have given me the advice and support for both experiment and analysis. Scientific discussions with them have always inspired me.

Dr. James J. Bock, Dr. Michael Zemcov, Dr. Phil Korngut (Caltech: California institute of technology), Dr. Daehee Lee (KASI: Korea astronomy and space science institute), Mr. Kim MinGyu (SUN: Seoul national university) are also the key drivers on my work. We have enjoyed a lot of experiment at the Caltech and the launch site.

I would like to acknowledge generous support that I have received from the Research Fellowships of the Japan Society for the Promotion of Science for Young Scientist (JSPS).

I would like to thank Satoko Sorahana for giving me a great picture of ZL. I would like to thank my family for their continuous understanding and support for my work.



# Bibliography

- Abe S., Mukai T., Hirata N., Barnouin-Jha O. S., Cheng A. F., Demura H., Gaskell R. W., Hashimoto T., Hiraoka K., Honda T., Kubota T., Matsuoka M., Mizuno T., Nakamura R., Scheeres D. J., Yoshikawa M., 2006, *Science*, 312, 1344
- Abraham P., Leinert C., Lemke D., 1997, *A&A*, 328, 702
- Arendt R. G., Odegard N., Weiland J. L., Sodroski T. J., Hauser M. G., Dwek E., Kelsall T., Moseley S. H., Silverberg R. F., Leisawitz D., Mitchell K., Reach W. T., Wright E. L., 1998, *ApJ*, 508, 74
- Asano R. S., Takeuchi T. T., Hirashita H., Nozawa T., 2013, *MNRAS*, 432, 637
- Bernstein R. A., 2007, *ApJ*, 666, 663
- Berriman G. B., Boggess N. W., Hauser M. G., Kelsall T., Lisse C. M., Moseley S. H., Reach W. T., Silverberg R. F., 1994, *ApJ*, 431, L63
- Binney J., Merrifield M., 1998, *Galactic Astronomy*
- Bock J., Battle J., Cooray A., Kawada M., Keating B., Lange A., Lee D.-H., Matsumoto T., Matsuura S., Pak S., Renbarger T., Sullivan I., Tsumura K., Wada T., Watabe T., 2006, *New A Rev.*, 50, 215
- Boggess N. W., Mather J. C., Weiss R., Bennett C. L., Cheng E. S., Dwek E., Gulkis S., Hauser M. G., Janssen M. A., Kelsall T., Meyer S. S., Moseley S. H., Murdock T. L., Shafer R. A., Silverberg R. F., Smoot G. F., Wilkinson D. T., Wright E. L., 1992, *ApJ*, 397, 420

- Bohren C. F., Huffman D. R., 1983, Absorption and scattering of light by small particles
- Brandt T. D., Draine B. T., 2012, *ApJ*, 744, 129
- Brownlee D. E., 1978, *Microparticle studies by sampling techniques*, McDonnell J. A. M., ed., pp. 295–336
- Bruzual G., Charlot S., 2003, *MNRAS*, 344, 1000
- Cambrésy L., Reach W. T., Beichman C. A., Jarrett T. H., 2001, *ApJ*, 555, 563
- Cruikshank D. P., Hartmann W. K., Tholen D. J., 1985, *Nature*, 315, 122
- de Vries C. P., Le Poole R. S., 1985, *A&A*, 145, L7
- Draine B. T., 2011, *Physics of the Interstellar and Intergalactic Medium*
- Dumont R., Levasseur-Regourd A. C., 1978, *A&A*, 64, 9
- Dumont R., Levasseur-Regourd A.-C., 1988, *A&A*, 191, 154
- Elsässer H., Haug U., 1960, *ZAp*, 50, 121
- Elvey C. T., Roach F. E., 1937, *ApJ*, 85, 213
- Fernández Y. R., Campins H., Kassis M., Hergenrother C. W., Binzel R. P., Licandro J., Hora J. L., Adams J. D., 2006, *AJ*, 132, 1354
- Frey A., Hofmann W., Lemke D., Thum C., 1974, *A&A*, 36, 447
- Gilmore G., Reid N., 1983, *MNRAS*, 202, 1025
- Girardi L., Groenewegen M. A. T., Hatziminaoglou E., da Costa L., 2005, *A&A*, 436, 895
- Gonzalez A. H., Brodwin M., Brown M. J. I., Dey A., Dickinson M., Gettings D., Stanford S. A., Stern D., Bock J., Bussman S., Cooray A., Eisenhardt P. R. M., Jannuzi B., Lin Y. T., Mainzer A., Sullivan I., 2010, in *American Astronomical Society Meeting Abstracts*, Vol. 216, American Astronomical Society Meeting Abstracts 216, p. 415.13

- Grun E., Zook H. A., Fechtig H., Giese R. H., 1985, *Icarus*, 62, 244
- Guhathakurta P., Tyson J. A., 1989, *ApJ*, 346, 773
- Hanner M. S., 1980, *Icarus*, 43, 373
- Hanner M. S., Weinberg J. L., Beeson D. E., Sparrow J. G., 1976, in *Lecture Notes in Physics*, Berlin Springer Verlag, Vol. 48, *Interplanetary Dust and Zodiacal Light*, Elsaesser H., Fechtig H., eds., pp. 29–35
- Hanner M. S., Weinberg J. L., DeShields II L. M., Green B. A., Toller G. N., 1974, *J. Geophys. Res.*, 79, 3671
- Hauser M. G., Dwek E., 2001, *ARA&A*, 39, 249
- Heiles C., 2000, *AJ*, 119, 923
- Henry L. G., Greenstein J. L., 1941, *ApJ*, 93, 70
- Hong S. S., 1985, *A&A*, 146, 67
- Ienaka N., Kawara K., Matsuoka Y., Sameshima H., Oyabu S., Tsujimoto T., Peterson B. A., 2013, *ApJ*, 767, 80
- Ishiguro M., Yang H., Usui F., Pyo J., Ueno M., Ootsubo T., Minn Kwon S., Mukai T., 2013, *ApJ*, 767, 75
- Kashlinsky A., Arendt R. G., Mather J., Moseley S. H., 2005, *Nature*, 438, 45
- Keenan R. C., Barger A. J., Cowie L. L., Wang W.-H., 2010, *ApJ*, 723, 40
- Kelley M. S., Woodward C. E., Jones T. J., Reach W. T., Johnson J., 2004, *AJ*, 127, 2398
- Kelsall T., Weiland J. L., Franz B. A., Reach W. T., Arendt R. G., Dwek E., Freudenreich H. T., Hauser M. G., Moseley S. H., Odegard N. P., Silverberg R. F., Wright E. L., 1998, *ApJ*, 508, 44
- Kim S.-H., Martin P. G., 1995, *ApJ*, 444, 293

- Krick J. E., Glaccum W. J., Carey S. J., Lowrance P. J., Surace J. A., Ingalls J. G., Hora J. L., Reach W. T., 2012, *ApJ*, 754, 53
- Laureijs R. J., Mattila K., Schnur G., 1987, *A&A*, 184, 269
- Lederer S. M., Domingue D. L., Vilas F., Abe M., Farnham T. L., Jarvis K. S., Lowry S. C., Ohba Y., Weissman P. R., French L. M., Fukai H., Hasegawa S., Ishiguro M., Larson S. M., Takagi Y., 2005, *Icarus*, 173, 153
- Leinert C., 1975, *Space Sci. Rev.*, 18, 281
- Leinert C., Bowyer S., Haikala L. K., Hanner M. S., Hauser M. G., Levasseur-Regourd A.-C., Mann I., Mattila K., Reach W. T., Schlosser W., Staude H. J., Toller G. N., Weiland J. L., Weinberg J. L., Witt A. N., 1998, *A&AS*, 127, 1
- Leinert C., Grun E., 1990, *Interplanetary Dust*, Schwenn R., Marsch E., eds., p. 207
- Leinert C., Pitz E., 1989, *A&A*, 210, 399
- Leinert C., Richter I., Pitz E., Hanner M., 1980, in *IAU Symposium*, Vol. 90, *Solid Particles in the Solar System*, Halliday I., McIntosh B. A., eds., pp. 15–18
- Leinert C., Richter I., Pitz E., Planck B., 1981, *A&A*, 103, 177
- Levasseur-Regourd A. C., 1996, in *Astronomical Society of the Pacific Conference Series*, Vol. 104, *IAU Colloq. 150: Physics, Chemistry, and Dynamics of Interplanetary Dust*, Gustafson B. A. S., Hanner M. S., eds., p. 301
- Levasseur-Regourd A. C., Dumont R., 1980, *A&A*, 84, 277
- Low F. J., Young E., Beintema D. A., Gautier T. N., Beichman C. A., Aumann H. H., Gillett F. C., Neugebauer G., Boggess N., Emerson J. P., 1984, *ApJ*, 278, L19
- Malhotra S., 1995, *ApJ*, 448, 138
- Mathis J. S., Mezger P. G., Panagia N., 1983, *A&A*, 128, 212

- Mathis J. S., Rumpl W., Nordsieck K. H., 1977, *ApJ*, 217, 425
- Matsumoto T., Kawada M., Murakami H., Noda M., Matsuura S., Tanaka M., Narita K., 1996, *PASJ*, 48, L47
- Matsumoto T., Matsuura S., Murakami H., Tanaka M., Freund M., Lim M., Cohen M., Kawada M., Noda M., 2005, *ApJ*, 626, 31
- Matsuoka Y., Ienaka N., Kawara K., Oyabu S., 2011, *ApJ*, 736, 119
- Matsuura S., Matsumoto T., Matsuhara H., Noda M., 1995, *Icarus*, 115, 199
- Mattila K., 1979, *A&A*, 78, 253
- , 1980, *A&AS*, 39, 53
- , 2003, *ApJ*, 591, 119
- , 2006, *MNRAS*, 372, 1253
- Nakanishi H., Sofue Y., 2003, *PASJ*, 55, 191
- Nesvorný D., Jenniskens P., Levison H. F., Bottke W. F., Vokrouhlický D., Gounelle M., 2010, *ApJ*, 713, 816
- Neugebauer G., Habing H. J., van Duinen R., Aumann H. H., Baud B., Beichman C. A., Beintema D. A., Boggess N., Clegg P. E., de Jong T., Emerson J. P., Gautier T. N., Gillett F. C., Harris S., Hauser M. G., Houck J. R., Jennings R. E., Low F. J., Marsden P. L., Miley G., Olton F. M., Pottasch S. R., Raimond E., Rowan-Robinson M., Soifer B. T., Walker R. G., Wesselius P. R., Young E., 1984, *ApJ*, 278, L1
- Nimura T., Hiroi T., Pieters C. M., 2008, *Earth, Planets, and Space*, 60, 271
- Oi N. e. a., 2013, in .., Vol. 00, , p. 000
- Olbers H. W. M., 1826, 110
- Ootsubo T., Onaka T., Yamamura I., Tanabé T., Roellig T. L., Chan K.-W., Matsumoto T., 1998, *Earth, Planets, and Space*, 50, 507

- Ootsubo T., Ueno M., Ishiguro M., Usui F., Pyo J., Hong S. S., Kwon S. M., Mukai T., Akari Mp-Sosos Members, 2009, in *Astronomical Society of the Pacific Conference Series*, Vol. 418, AKARI, a Light to Illuminate the Misty Universe, Onaka T., White G. J., Nakagawa T., Yamamura I., eds., p. 395
- Paley E. S., Low F. J., McGraw J. T., Cutri R. M., Rix H.-W., 1991, *ApJ*, 376, 335
- Ramsay S. K., Mountain C. M., Geballe T. R., 1992, *MNRAS*, 259, 751
- Reach W. T., Franz B. A., Weiland J. L., Hauser M. G., Kelsall T. N., Wright E. L., Rawley G., Stemwedel S. W., Spiesman W. J., 1995, *Nature*, 374, 521
- Reach W. T., Morris P., Boulanger F., Okumura K., 2003, *Icarus*, 164, 384
- Renard J. B., Levasseur-Regourd A. C., Dumont R., 1995, *A&A*, 304, 602
- Schlegel D. J., Finkbeiner D. P., Davis M., 1998, *ApJ*, 500, 525
- Silverberg R. F., Hauser M. G., Boggess N. W., Kelsall T. J., Moseley S. H., Murdock T. L., 1993, in *Society of Photo-Optical Instrumentation Engineers (SPIE) Conference Series*, Vol. 2019, *Infrared Spaceborne Remote Sensing*, Scholl M. S., ed., pp. 180–189
- Soderblom L. A., Becker T. L., Bennett G., Boice D. C., Britt D. T., Brown R. H., Buratti B. J., Isbell C., Giese B., Hare T., Hicks M. D., Howington-Kraus E., Kirk R. L., Lee M., Nelson R. M., Oberst J., Owen T. C., Rayman M. D., Sandel B. R., Stern S. A., Thomas N., Yelle R. V., 2002, *Science*, 296, 1087
- Spiesman W. J., Hauser M. G., Kelsall T., Lisse C. M., Moseley Jr. S. H., Reach W. T., Silverberg R. F., Stemwedel S. W., Weiland J. L., 1995, *ApJ*, 442, 662
- Stark R., 1995, *A&A*, 301, 873
- Tokunaga A. T., Golisch W. F., Griep D. M., Kaminski C. D., Hanner M. S., 1986, *AJ*, 92, 1183

- Totani T., Yoshii Y., Iwamuro F., Maihara T., Motohara K., 2001, *ApJ*, 550, L137
- Tsumura K., Arai T., Battle J., Bock J., Brown S., Cooray A., Hristov V., Keating B., Kim M. G., Lee D. H., Levenson L. R., Lykke K., Mason P., Matsumoto T., Matsuura S., Murata K., Nam U. W., Renbarger T., Smith A., Sullivan I., Suzuki K., Wada T., Zemcov M., 2013a, *ApJS*, 207, 33
- Tsumura K., Battle J., Bock J., Cooray A., Hristov V., Keating B., Lee D. H., Levenson L. R., Mason P., Matsumoto T., Matsuura S., Nam U. W., Renbarger T., Sullivan I., Suzuki K., Wada T., Zemcov M., 2010, *ApJ*, 719, 394
- Tsumura K., Matsumoto T., Matsuura S., Pyo J., Sakon I., Wada T., 2013b, *ArXiv e-prints*
- Tsumura K., Matsumoto T., Matsuura S., Sakon I., Tanaka M., Wada T., 2013c, *ArXiv e-prints*
- van de Hulst H. C., de Jong T., 1969, *Physica*, 41, 151
- Weingartner J. C., Draine B. T., 2001, *ApJ*, 548, 296
- Witt A. N., Mandel S., Sell P. H., Dixon T., Vihj U. P., 2008, *ApJ*, 679, 497
- Wolstencroft R. D., Rose L. J., 1966, *Nature*, 209, 388
- Wyatt M. C., 2008, *ARA&A*, 46, 339
- Zagury F., Boulanger F., Banchet V., 1999, *A&A*, 352, 645
- Zemcov M., Arai T., Battle J., Bock J., Cooray A., Hristov V., Keating B., Kim M. G., Lee D. H., Levenson L. R., Mason P., Matsumoto T., Matsuura S., Nam U. W., Renbarger T., Sullivan I., Suzuki K., Tsumura K., Wada T., 2013, *ApJS*, 207, 31
- Zubko V., Dwek E., Arendt R. G., 2004, *ApJS*, 152, 211